Pharmaceutics, Drug Delivery and Pharmaceutical Technology

Molecular Dynamics Simulation of Amorphous Indomethacin–Poly(Vinylpyrrolidone) Glasses: Solubility and Hydrogen Bonding Interactions

TIAN-XIANG XIANG, BRADLEY D. ANDERSON

Department of Pharmaceutical Sciences, College of Pharmacy, University of Kentucky, Lexington, Kentucky 40536

Received 3 August 2012; revised 17 August 2012; accepted 9 October 2012

Published online 20 December 2012 in Wiley Online Library (wileyonlinelibrary.com). DOI 10.1002/jps.23353

ABSTRACT: Amorphous drug dispersions are frequently employed to enhance solubility and dissolution of poorly water-soluble drugs and thereby increase their oral bioavailability. Because these systems are metastable, phase separation of the amorphous components and subsequent drug crystallization may occur during storage. Computational methods to determine the likelihood of these events would be very valuable, if their reliability could be validated. This study investigates amorphous systems of indomethacin (IMC) in poly(vinylpyrrolidone) (PVP) and their molecular interactions by means of molecular dynamics (MD) simulations. IMC and PVP molecules were constructed using X-ray diffraction data, and force-field parameters were assigned by analogy with similar groups in Amber-ff03. Five assemblies varying in PVP and IMC composition were equilibrated in their molten states then cooled at a rate of 0.03 K/ps to generate amorphous glasses. Prolonged aging dynamic runs (100 ns) at 298 K and 1 bar were then carried out, from which solubility parameters, the Flory–Huggins interaction parameter, and associated hydrogen bonding properties were obtained. Calculated glass transition temperature (T_g) values were higher than experimental results because of the faster cooling rates in MD simulations. Molecular mobility as characterized by atomic fluctuations was substantially reduced below the T_g with IMC–PVP systems exhibiting lower mobilities than that found in amorphous IMC, consistent with the antiplasticizing effect of PVP. The number of IMC–IMC hydrogen bonds (HBs) formed per IMC molecule was substantially lower in IMC–PVP mixtures, particularly the fractions of IMC molecules involved in two or three HBs with other IMC molecules that may be potential precursors for crystal growth. The loss of HBs between IMC molecules in the presence of PVP was largely compensated for by the formation of IMC–PVP HBs. The difference (6.5 $\text{MPa}^{1/2}$) between the solubility parameters in amorphous IMC (25.5 $\text{MPa}^{1/2}$) and PVP (19.0 $\text{MPa}^{1/2}$) suggests a small, positive free energy of mixing, although it is close to the criterion for miscibility (<7 $\text{MPa}^{1/2}$). In contrast to the solubility-parameter method, the calculated Flory–Huggins interaction parameter (-0.61 ± 0.25), which takes into account the IMC–PVP interaction energy, predicts complete miscibility at all PVP compositions, in agreement with experimental observations. These results from MD simulations were combined with experimental values for the crystalline γ-polymorph of IMC and amorphous IMC to estimate the solubility of IMC in amorphous PVP dispersions and the theoretical enhancement in the aqueous solubility of IMC molecularly dispersed in PVP at various volume fractions. © 2012 Wiley Periodicals, Inc. and the American Pharmacists Association J Pharm Sci 102:876–891, 2013

Keywords: solid-state stability; solid dispersion; solubility; amorphous; molecular dynamics; mobility; physical stability; supersaturation; polymers; poly(vinylpyrrolidone)

INTRODUCTION

Amorphous solid drug dispersions are being increasingly considered in the pharmaceutical industry as a potential means for enhancing oral bioavailability of poorly soluble drugs. Poorly water-soluble drugs such as indomethacin (IMC) generally have higher

---

Additional Supporting Information may be found in the online version of this article. Supporting Information

Correspondence to: Bradley D. Anderson (Telephone: +859-218-6536; Fax: +859-323-0242; E-mail: bande@email.uky.edu)

Journal of Pharmaceutical Sciences, Vol. 102, 876–891 (2013)

© 2012 Wiley Periodicals, Inc. and the American Pharmacists Association

However, the presence of multiple HB acceptors in PVP suggests possible migration of HBs between IMC molecules to those between IMC and PVP upon mixing IMC with PVP as evident in Fourier transform infrared (FTIR) results.[11] The degree of this migration and its net effect on the enthalpy of mixing may be critically important in determining the miscibility of IMC with PVP. The disordered molecular organization and conformational diversity in amorphous IMC–PVP solids may lead to complex HB interaction patterns and conformational distributions that vary with the method of glass preparation and thermal history. Unraveling molecular structures such as HB distributions in amorphous solids experimentally remains a challenge as little detailed information can be gained from X-ray diffraction, the technique that is commonly used to determine crystal structures, whereas other spectroscopic techniques such as nuclear magnetic resonance, FTIR, and Raman provide rather limited insights due to poor resolution and/or quantitation.[11]

Molecular dynamics (MD) simulations can provide detailed atomic-level structural and energetic information that may be important in predicting solubility and miscibility of amorphous drug–excipient solid dispersions but cannot be easily obtained experimentally. Using MD methods, significant progress has been made in recent years toward developing model drug–excipient glasses and understanding their solubility/miscibility properties.[25–27] For example, MD simulations were recently utilized to predict the miscibility of IMC with certain pharmaceutical carriers by calculating and comparing their solubility parameters.[25] However, relatively fewer MD simulations have explored the underlying molecular interactions that govern miscibility/solubility nor have drug–carrier miscibility, drug solubility in a polymeric carrier, and the aqueous solubility enhancement that may be possible for drugs molecularly dispersed in a polymeric matrix been estimated by coupling MD simulations with a more exact model, the Flory–Huggins theory. These are the main goals of the present MD study.

The thermodynamic processes of interest are schematically illustrated in Figure 2. We first employed a classical-mechanics model for IMC based on crystalline structural data and the Amber force field[23] and one previously established for PVP[24] to construct IMC, PVP, and IMC–PVP assemblies containing a small but nearly constant amount of water. These assemblies were then equilibrated in their molten states and cooled to form amorphous solids followed by long aging dynamic runs (~100 ns) to determine solubility and miscibility and explore those structural properties (e.g., hydrogen bonding distributions) that may have a strong impact on these thermodynamic properties.

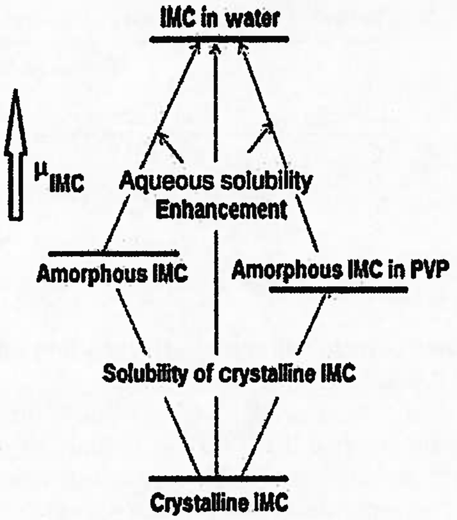

Figure 2. Schematic depiction of various thermodynamic processes addressed in this study.

COMPUTATIONAL METHODS

A molecular model for IMC was developed in a separate study.[23] Briefly, IMC molecules were built using xLeap/Amber (University of California, San Francisco, CA, USA). The force-field parameters for bond length and angle associated with different atomic types were determined based on available X-ray diffraction crystal-structure data (Cambridge Structural Database). Other molecular parameters for various torsional potentials and nonbonded Lennard–Jones potentials were assigned by analogy with existing parameters in the Amber database (ff03) except that the energy barrier for rotation of the chlorobenzyl group (*cf.*, φ_2 in Fig. 1) was reduced from 29.0 to 8.0 kcal/mol to facilitate the transition between and therefore sampling of various diastereomeric forms of IMC as characterized by the torsional angle φ_1 in Figure 1. Atomic partial charges for IMC were determined by first calculating the electrostatic potentials (ESPs) at the level of B3LYP/ccpVTZ30 along with the IEFPCM model[28–30] using Gaussian 03 followed by fitting the ESPs with the restrained electrostatic potential (RESP) method.[31,32]

The procedure for building PVP polymer molecules has been described previously.[24] Each PVP chain had 40 monomers with a total molecular weight of 4456 Da, comparable with the commercial PVP products Kollidon 12 (2000–3000 Da) or Kollidon 17 (7000–11000 Da) from BASF Company.[33] The backbone carbon covalently bonded to the nitrogen atom in each PVP monomer (*cf.*, Fig. 1) is a chiral center. Adjacent chiral center pairs or dyads along a PVP chain are in either a racemo or meso conformation. The dyad sequences in PVP were determined by assigning to each a random number between 0.0 and 1.0

expression[26,40,41]:

$$\Delta H_{\text{mix}} = \left(\frac{\Delta E_{\text{v}}}{V}\right)_{\text{IMC-PVP}} - \Phi_{\text{IMC}}\left(\frac{\Delta E_{\text{v}}}{V}\right)_{\text{IMC}} - \Phi_{\text{PVP}}\left(\frac{\Delta E_{\text{v}}}{V}\right)_{\text{PVP}} \qquad (4)$$

where Φ_{IMC} and Φ_{PVP} denote the volume fractions of IMC and PVP in an IMC–PVP mixture.

RESULTS AND DISCUSSION

Formation of IMC, PVP, and IMC–PVP Glasses

Experimentally, amorphous IMC glass has been prepared by heating the γ-crystalline polymorph of IMC to 210°C followed by quenching in liquid nitrogen.[42] Similarly, in the present MD simulation, molten liquids at 600–800 K were rapidly cooled to 200 K at a cooling rate of 0.03 K/ps. A representative three-dimensional image of a simulated IMC–PVP glass (41%:68%, w/w) formed at 298 K is shown in Figure S1 of the Supporting Information section.

Representative density-temperature diagrams for the simulated IMC,IMC–PVP (41%:68%, w/w), and PVP assemblies are shown in Figure 3. Changes in the absolute values of the slopes of density versus temperature are evident, indicative of glass transitions. The absolute values of the slopes for IMC, IMC–PVP, and PVP were, respectively, 6.33, 5.00, 4.17 × 10^{-4} g/(cm^3 K) above T_g and 3.03, 2.60, 2.54 × 10^{-4} g/(cm^3 K) below the glass transition temperature (T_g). Thus, the changes in density with temperature are greater for the bulky IMC molecules than for the long and flexible PVP chains. The ratios of the slopes below and above T_g (2.1, 1.9, and 1.6) are also in the same order suggesting a more sharply defined transition in IMC-containing systems. Estimates of T_g were determined by the points of intersection of straight lines drawn through the data below and above T_g,[43] which yielded values of 384, 473, and 595 K for amorphous IMC, IMC–PVP (41%:68%, w/w), and PVP, respectively. In accord with experimental results,[12] incorporation of IMC into a PVP polymer matrix increases the T_g in relation to IMC itself. This antiplasticizing effect of PVP has been proposed as one of the mechanisms for inhibition of IMC crystallization.[18] Depending on molecular weight, the T_g for commercial PVP products can vary from 373 to 463 K.[44] Thus, the simulated T_g for the PVP assembly is approximately 100–200 degrees higher than the experimental results. Likewise, the T_g for the simulated IMC assembly (384 K) is approximately 64 degrees higher than the experimental value of approximately 320 K.[5] The much faster (~10^{11}-fold) cooling rate employed here (0.03 K/ps) compared with experimental cooling rates (e.g., 20 K/min for IMC[5]) is probably the main cause of the disparity.[45,46] Similar results have been reported in other simulated amorphous solids.[24,47,48]

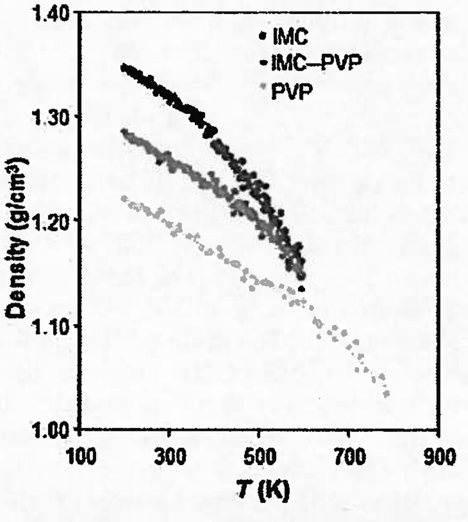

Figure 3. Density versus temperature diagrams for the simulated IMC, PVP, and IMC–PVP (58%:41%, w/w) assemblies.

Theoretically, the T_g for a binary mixture may be predicted from the Gordon–Taylor equation,[49]

$$T_{\text{g,mix}} = \frac{w_1 T_{\text{g1}} + K w_2 T_{\text{g2}}}{w_1 + K w_2} \qquad (5)$$

where w_1 and w_2 are the weight fractions of the two components, T_{g1} and T_{g2} are their respective glass transition temperatures, and K is a constant given by

$$K = \frac{\rho_1 T_{\text{g1}}}{\rho_2 T_{\text{g2}}} \qquad (6)$$

or by the Couchman–Karasz equation,

$$K = \frac{\Delta C_{\text{p1}}}{\Delta C_{\text{p2}}} \qquad (7)$$

where ρ_1 and ρ_2 are the densities of the two components. The values of the heat capacity changes at T_g for the two components (IMC and PVP) reported by Crowley and Zografi[13] were used in the present calculation ($\Delta C_{\text{p1}}/\Delta C_{\text{p2}} = 0.41/0.26$). The theoretical prediction based on the Couchman–Karasz estimate for K gives a $T_{\text{g,mix}}$ of 455 K, close to that obtained from the simulated 41%:68% (w/w) IMC–PVP glass (473 K), a system in which the drug–polymer interaction is strong.

Dramatic changes in molecular mobility occur at the glass transition temperature. In this study, molecular mobility is measured by the atomic fluctuation, or how far each atom moves from its average position within a certain time interval.[50] The atomic fluctuation, which can be converted to the B-factor by

Chains (or aggregates) of IMC molecules connected by carboxylic acid–carboxylic acid HBs were the more easily identified HB patterns in the simulated amorphous IMC solids.

For the amorphous 58%:41% (w/w) IMC–PVP solids simulated, results from Figure 5 (upper panel) indicate that the average number of HBs formed per IMC molecule is substantially reduced (1.5 vs. 0.85) upon addition of 41% (w/w) PVP. Interestingly, the probability of forming just one HB in an IMC molecule is actually increased (0.31 vs. 0.61) at the expense of sharply lower probabilities for forming two (0.42 vs. 0.094) or three HBs (0.091 vs. 0.019). The probability of finding IMC molecules that are not involved in a HB is now increased from 0.17 to 0.28. The inhibition of IMC dimer formation in the presence of PVP has been suggested as the major basis for inhibition of crystallization of IMC in IMC–PVP solid dispersions.[12] Figure 5 (lower panel) shows that in the presence of 41% (w/w) PVP, the carboxylic acid in IMC molecules is more likely ($p \sim 0.67$) to form hydrogen bonds with the carbonyl groups in PVP, a representative snapshot of which is illustrated in Figure S2 of the Supporting Information section. These results are consistent with previous experimental findings that incorporation of IMC into amorphous PVP increases the intensity of the infrared band at 1726 cm^{-1} assigned to the nonhydrogen bonded acid carbonyl of IMC and also leads to the appearance of a new peak at 1636 cm^{-1} assigned to the hydrogen-bonded PVP carbonyl.[11]

Because the carboxylic acid group in IMC is the only HB donor among the IMC and PVP molecules, the overall HB capacity can be measured by the fraction of the carboxylic acid groups donating a hydrogen to form a HB in the IMC–PVP mixtures varying in composition. The results, presented in Figure 6 (upper panel), indicate that the overall HB capacity does not change substantially with PVP concentration. Clearly, the loss of HBs between IMC molecules as percent PVP is increased is largely compensated for by the formation of HBs between IMC and PVP molecules, as indicated by the results in Figure 6 (lower panel). Thus, from an energetic point of view, electrostatic interactions favorably influence the mixing of amorphous IMC with amorphous PVP.

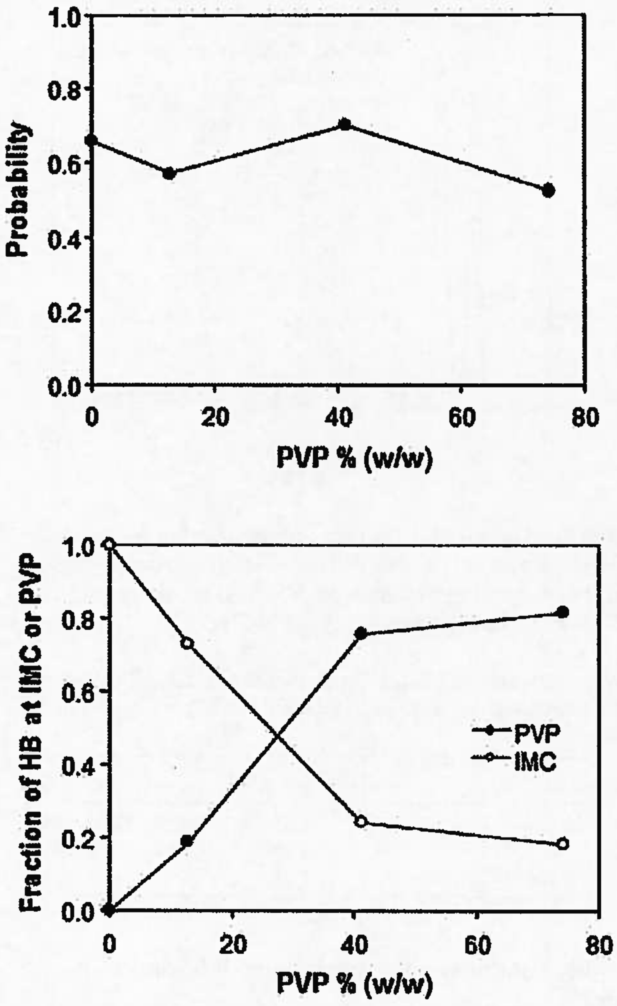

Figure 6. Upper panel: fraction of the carboxylic acid HB donor in IMC forming a HB in amorphous IMC–PVP mixtures as a function of weight percentage of PVP at 298 K. Lower panel: fraction of hydrogen bonded carboxylic acid donors in IMC molecules that are hydrogen bonded to HB acceptors in IMC and PVP molecules versus PVP concentration in the amorphous solids at 298 K.

Figure 7 shows the radial distribution function, $g(r)$, between the carboxylic acid proton and the IMC–COOH carbonyl oxygen and PVP carbonyl oxygen HB acceptors, respectively. Considering first the distribution function between the –COOH proton and the –COOH carbonyl oxygen, there are three distinct peaks. The first peak at 1.55 Å corresponds to a HB between two IMC molecules, the second peak at 2.25 Å represents the intramolecular distance between the proton and carbonyl oxygen in the donor IMC molecule, and the third peak at 3.15 Å represents the distance between the –COOH proton of one IMC molecule and a second IMC molecule that is acting as the proton donor to the –COOH carbonyl oxygen. The HB length, a measure of the HB strength, was found to be 1.550 Å for both the IMC–IMC and IMC–PVP hydrogen bonds represented by the first peak in the corresponding $g(r)$. Compared with the HB lengths in α- and γ-crystal forms (1.604 and 1.637 Å),[52] these results suggest strong and similar hydrogen bonding between the carboxylic acid in one IMC molecule with the carboxylic acid carbonyl oxygen atom of another IMC molecule and between the carboxylic acid in IMC and the carbonyl oxygen in PVP in the simulated IMC–PVP amorphous solids.

chemical composition. This is particularly relevant in light of the intense interest in making glasses that are more stable against crystallization for drug formulation through traditional physical annealing or, more recently, through novel preparatory methods such as physical vapor deposition.[16]

The solubility parameter difference ($\Delta\delta$) between IMC and PVP calculated in this study is 6.5 MPa$^{1/2}$. Comparing the electrostatic (δ_e) and nonpolar (δ_d) solubility parameter components for IMC and PVP in Table 2, it seems that the difference in $\Delta\delta$ arises mostly from the electrostatic component ($\delta_e \sim 14.4$ vs. 2.9 MPa$^{1/2}$) apparently because of the fact that IMC possesses both HB donor and acceptors and can thereby form a hydrogen bonded network, whereas PVP by itself has no HB capacity. The calculated $\Delta\delta$ (6.5 MPa$^{1/2}$) is near the miscibility boundary (<7 MPa$^{1/2}$) mentioned above.[20] Apart from the calculation uncertainties due to imperfect force fields and limited simulation times, caution should still be excised when this criterion is used to predict the miscibility. First, the use of solubility parameters to predict solubility is based on the Hildebrand regular solution theory,[60]

$$\ln X_s = \ln X_o - \frac{(\delta_{\mathrm{PVP}} - \delta_{\mathrm{IMC}})^2 V_{\mathrm{IMC}} \Phi_{\mathrm{PVP}}^2}{RT} \qquad (8)$$

where X_s and X_o are, respectively, the actual mole fraction solubility for IMC in PVP and its ideal mole fraction solubility, and Φ and V denote a particular volume fraction and molar volume, respectively. The regular solution theory may be a good approximation for binary systems lacking specific interactions but extension to those with strong hydrogen bonded networks such as IMC–PVP mixtures may be problematic. The fact that the second term in Eq. 8 is always negative also points to the inability of this model to accurately predict solubility in systems with exothermic enthalpies of mixing, which is usually the case for binary systems with stronger intermolecular interactions.[22]

Flory–Huggins Interaction Parameter for Amorphous IMC–PVP Solids

Flory–Huggins lattice theory[64,65] is a more suitable approach for evaluating the free energy of mixing (ΔG_{mix}) because it takes into account the intermolecular interactions in the binary mixture of interest, as characterized by the interaction parameter, $\chi_{\mathrm{IMC\text{–}PVP}}$, in the following expression,

$$\frac{\Delta G_{\mathrm{mix}}}{RT} = \frac{\Delta H_{\mathrm{mix}} - T\Delta S_{\mathrm{mix}}}{RT} = n_{\mathrm{IMC}} \ln \Phi_{\mathrm{IMC}} + n_{\mathrm{PVP}} \ln \Phi_{\mathrm{PVP}} + n_{\mathrm{IMC}} \Phi_{\mathrm{PVP}} \chi_{\mathrm{IMC\text{–}PVP}} \qquad (9)$$

where n_{IMC} and n_{PVP} are the numbers of moles of IMC and PVP in the mixture. The first two terms describe the entropy contribution to mixing that is always negative and therefore favorable for mixing. The third term measures the interaction strength between IMC and PVP with $\chi_{\mathrm{IMC\text{–}PVP}}$ being determined from the enthalpy of mixing (ΔH_{mix}) according to Eq. 3. In this study, ΔH_{mix} for IMC–PVP (58%:41%, w/w) was calculated from the CED values for the newly formed IMC, PVP, and IMC–PVP glasses and as a function of aging time (~100 ns) after glass formation at 298 K. The results are presented in Figure S3 of the Supporting Information section. ΔH_{mix} averaged -2.3 ± 0.9 cal/mol over the entire simulation run. The negative ΔH_{mix} obtained thus suggests favorable mixing of amorphous IMC and PVP. From this calculated ΔH_{mix} an interaction parameter, $\chi_{\mathrm{IMC\text{–}PVP}}$, of -0.61 ± 0.25 was obtained.

Several experimental methods have been used to determine the interaction parameter $\chi_{\mathrm{IMC\text{–}PVP}}$ with quite different results: (1) water sorption isotherms in IMC–PVP amorphous solids,[13,66] (2) melting-point-depression of crystalline IMC in the presence of amorphous PVP as measured with differential scanning calorimetry,[22] and (3) determination of IMC solubility in 1-ethyl-2-pyrrolidone, a liquid and prototype PVP monomer.[22] Crowley and Zografi[13] predicted a positive $\chi_{\mathrm{IMC\text{–}PVP}}$ (1.3–1.5) by fitting the Flory–Huggins model to the moisture sorption results. More recently, a negative $\chi_{\mathrm{IMC\text{–}PVP}}$ was obtained by the melting-point-depression method but the result varied considerably depending on whether onset (−6.16), midpoint (−1.94), or offset (−0.82) values of the melting event were used. The solubility method gave a negative interaction parameter of −1.83. Compared with the melting-point-depression method, the present MD result (−0.61) is close to that (−0.82) obtained from the offset of melting. Theoretically, the offset value should be used because this shows the melting point at the final composition, assuming complete mixing has occurred.[22] The present MD simulations and the melting-point-depression/solubility experiments predict negative $\chi_{\mathrm{IMC\text{–}PVP}}$ values and therefore a favorable free energy of mixing, whereas the water sorption study by Crowley and Zografi[13] predicts rather limited miscibility. Apart from statistical uncertainty, several factors may affect the outcome of a $\chi_{\mathrm{IMC\text{–}PVP}}$ determination from both experiment and MD simulation: (1) as pointed out by Rumondor et al.,[66] $\chi_{\mathrm{IMC\text{–}PVP}}$ is poorly determined in the application of the Flory–Huggins theory to water sorption isotherms for IMC–PVP mixtures because of much stronger water–IMC and water–PVP interactions than IMC–PVP interactions. The presence of specific drug–polymer interactions may alter the water–drug and the water–polymer interactions in the mixtures. Indeed, their estimate of $\chi_{\mathrm{IMC\text{–}PVP}}$ varied over a wide range block copolymers by Patel et al.[69] found that Flory–Huggins interaction parameters computed by MD simulations were consistent with the experimental solubility data in these drug–polymer systems, whereas those obtained by the solubility-parameter method deviated significantly from experiment. Inspecting all energy components in the MD simulation can shed light on their respective contributions to the free energy of mixing. In particular, the present simulation reveals that the favorable free energy of mixing is not because the IMC-IMC molecular interactions are similar to PVP-PVP interactions as judged by their respective CED values, $(E_v/V)_{IMC}$ and $(E_v/V)_{PVP}$, employed in the solubility parameter calculation. Rather, it is the strong interactions between IMC and PVP molecules as measured by $(E_v/V)_{IMC\text{–}PVP}$ that lead to a negative ΔH_{mix}.

Solubility of Crystalline IMC in Amorphous IMC and PVP

Amorphous solid drug dispersions are typically thermodynamically unstable and often supersaturated with respect to the crystalline drug. Over time, that amount of molecularly dispersed drug that exceeds its equilibrium solubility will crystallize. This inherent instability is a primary concern in considering the potential commercial success of amorphous solid drugs.

Amorphous IMC can be formed by cooling molten IMC sufficiently rapidly to avoid crystallization. Below the melting point but above T_g, the IMC molecules have sufficient molecular mobility to reorganize to their equilibrium state with decreasing temperature until the supercooled melt becomes so highly viscous that glass formation ensues. At temperatures below T_g, amorphous IMC is a metastable glass trapped in a higher energetic state than the equilibrium supercooled IMC melt that would have formed given infinite time for relaxation. This hypothetical (equilibrium) supercooled melt serves as a useful reference system for calculating the ideal solubility of crystalline IMC representing the solubility of IMC in a solvent virtually identical to the supercooled melt at the temperature of interest (i.e., 298 K). At equilibrium, a small quantity of IMC would dissolve in this hypothetical solvent until the chemical potential of IMC in the crystal equals that in the liquid ($\mu_{IMC}^{crystal} = \mu_{IMC}^{sol'n}$). The chemical potential for IMC in solution can be expressed in terms of the chemical potential of the standard state, $\mu^{\circ}{}_{sol'n}^{crystal}$, and the IMC concentration. Then,

$$\mu^{\circ}{}_{IMC}^{crystal} = \mu^{\circ}{}_{IMC}^{sol'n} + RT\ln X_{IMC} \tag{12}$$

The ideal mole fraction solubility of IMC in the supercooled melt, X_{IMC}, can be estimated from the melting point (T_m) of IMC, the heat of fusion at the melting temperature (ΔH_f), and the heat capacity difference between the supercooled liquid and the crystal (ΔC_p) according to[22]

$$\begin{aligned}\ln X_{IMC} &= -\frac{\Delta G^{\circ}_{crystal\text{->}sol'n}}{RT} \\ &= -\frac{\Delta H_f}{RT}\left[1-\frac{T}{T_m}\right] \\ &\quad + \frac{\Delta C_p}{R}\left[\frac{T_m - T}{T} + \ln\left(\frac{T}{T_m}\right)\right]\end{aligned} \tag{13}$$

At 298 K, applying the IMC values needed in Eq. 13 as reported by Murdande et al.[70] yields an estimated ideal mole fraction solubility of 0.048 for IMC.

Similar to the above, the solubility of IMC in amorphous IMC can be related to the difference between the crystal and amorphous standard state free energies, $\Delta G^{\circ}_{crystal \rightarrow amorphousIMC}$ at 298 K, which can be determined from the temperature dependence of $\Delta G^{\circ}_{crystal \rightarrow amorphousIMC}$ as described by the van't Hoff equation,

$$\frac{\partial\left(\Delta G^{\circ}_{crystal\rightarrow amorphousIMC}\right)/T)}{\partial T} = -\frac{\Delta H^{\circ}_{crystal\rightarrow amorphousIMC}}{T^2} \tag{14}$$

Integrating the above equation, we have

$$\Delta G_{crystal\rightarrow amorphousIMC} = -T\int_{T_m}^{T}\frac{\Delta H_{crystal\rightarrow amorphousIMC}}{T^2}\,dT \tag{15}$$

where $\Delta H^{\circ}_{crystal \rightarrow amorphousIMC}$ is dependent on temperature and can be expressed in terms of the enthalpy of fusion at the melting temperature (ΔH_f) and the constant-pressure heat capacity difference between the supercooled glass and the crystalline state, $\Delta C_{p\ crystal\rightarrow amorphous\ IMC}$,

$$\Delta H_{crystal\rightarrow amorphousIMC} = \Delta H_f + \int_{T_m}^{T}\Delta C_{pcrystal\rightarrow amorphousIMC}\,dT \tag{16}$$

Thus, $\Delta G^{\circ}_{crystal \rightarrow amorphousIMC}$ at 298 K can be estimated from the experimentally determined heat of fusion and heat capacity versus T data. Although several approximate methods to estimate $\Delta C_{p\ crystal\rightarrow amorphous\ IMC}$ have been introduced,[1] Murdande et al.[70] took into consideration the difference of ΔC_p below and above T_g with a discontinuous using thermal analysis may be erroneous if mixing and equilibration between crystalline and amorphous drugs are not complete within the timescale of the experiments, even though attempts have been made to address these problems. On the basis of the present MD study, γ-crystalline IMC has a very low solubility in PVP and as a result, amorphous IMC dispersed in practical solid PVP formulations would be supersaturated and thermodynamically unstable. The rate of IMC crystallization would then be controlled by structural and kinetic factors such as proximity of the carboxylic groups in neighboring IMC molecules and rotational/translational mobility of IMC molecules. Both factors, as demonstrated in the present study, appear to favor PVP polymer as a drug carrier for IMC.

Aqueous Solubility Enhancement for Amorphous IMC in PVP Compared with Crystalline IMC

Amorphous solid dispersions in pharmaceutically acceptable excipients are receiving increased attention for the formulation of poorly water-soluble drugs such as unionized IMC. Unfortunately, it is extremely difficult to measure the aqueous solubility of drugs dispersed in hydrophilic excipients such as PVP because the solvent properties and integrity of the dispersion are often rapidly altered by water uptake upon contact with an aqueous solution and the drug tends to rapidly crystallize in the predominantly aqueous environment before a true solubility equilibrium can be reached. It would be of interest to determine the theoretical aqueous solubility enhancement achievable in the absence of these complicating factors. On the basis of the free energy of mixing of amorphous IMC and PVP obtained from the present MD simulations and the free energy difference between pure crystalline and amorphous IMC, $\Delta G^{\circ}_{\text{crystal}\rightarrow\text{amorphousIMC}}$, obtained previously,[1,70] the overall free energy change between pure crystalline IMC and amorphously dispersed IMC in PVP can be determined from the following expression:

$$\Delta G_{\text{crystal}\rightarrow\text{amorphousIMC/PVP}} = \Delta G^{\circ}_{\text{crystal}\rightarrow\text{amorphousIMC}} + \frac{\partial \Delta G_{\text{mix}}}{\partial n_{\text{IMC}}} \qquad (22)$$

In the above equation, $\partial \Delta G_{\text{mix}}/\partial n_{\text{IMC}}$ is the chemical potential change upon mixing amorphous IMC with PVP, which, as expressed in Eq. 20, depends on PVP concentration and can be determined from the interaction parameter $\chi_{\text{IMC–PVP}}$ obtained in the present MD simulations and the chemical composition (Φ_{IMC} and Φ_{PVP}) of the IMC–PVP mixture. Thus, the overall solubility enhancement for amorphous IMC in an amorphous PVP dispersion compared with the pure crystalline IMC can be obtained by combining Eq. 22 with $\Delta G^{\circ}_{\text{crystal}\rightarrow\text{amorphousIMC}} = 1.99$kcal/mol obtained by Murdande et al.[70]:

$$\begin{aligned} S &= \exp\left(\Delta G^{\circ}_{\text{crystallineIMC}\rightarrow\text{amorphousIMC/PVP}}/RT\right) \\ &= \exp(1.99/RT + \ln(1-\Phi_{\text{IMC}}) \\ &\quad + (1 - V_{\text{IMC}}/V_{\text{PVP}})\Phi_{\text{PVP}} + \Phi_{\text{PVP}}\chi_{\text{IMC–PVP}}) \end{aligned} \qquad (23)$$

The results are presented in Figure 8 (lower panel) as a function of PVP concentration. At low PVP concentrations the solubility enhancement decreases only gradually with an increase in PVP (<12% for $\Phi_{\text{IMC}} \leq 0.5$), whereas the decrease becomes more dramatic at high PVP concentrations. One should bear in mind, however, that the conformational entropy term in the simple Flory–Huggins model (i.e., Eq. 9) is derived with the approximation of $\Phi_{\text{IMC}} > \Phi_{\text{PVP}}$, and is therefore strictly applicable only at relatively low PVP concentrations. At an equal volume fraction ($\Phi_{\text{IMC}} = \Phi_{\text{PVP}}$), the overall solubility enhancement is 19.6 reflecting contributions of 29.0-fold from the conversion of γ-crystalline IMC to amorphous IMC and 0.68-fold from the mixing of amorphous IMC with PVP.

Recent years have witnessed an increasing frequency in attempts to experimentally measure the apparent aqueous solubility enhancement for hydrophobic drugs formulated in amorphous solid dispersions. Dissolution studies for various amorphous drug dispersions in polymers often suggest an apparent solubility that is higher than that obtained for the pure amorphous drug.[73-75] For example, Alonzo et al.[76] found that the peak concentration of IMC generated during the dissolution of a 50:50 IMC–PVP solid dispersion was similar to the predicted amorphous drug solubility. These observations are often attributed to complex phenomena such as micelle formation, supersaturation, or crystallization of drugs to form nanometer-sized particles upon rapid swelling and disintegration of the drug–polymer dispersions in aqueous solution.[73,76] For instance, Friesen et al.[73] found that spray-dried dispersions of low-solubility drugs in hydroxypropylmethylcellulose acetate succinate were supersaturated in *in vitro* bile-salt/lecithin solutions due to formation of various drug–polymer colloids as characterized by dynamic light scattering and cryogenic transmission electron microscopy. At this stage, the various processes that amorphous solid dispersions undergo after their administration are still poorly understood and a "clean" experimental determination of the aqueous solubility enhancement exhibited by drug–polymer solid dispersions is still lacking.

11. Taylor LS, Zografi G. 1997. Spectroscopic characterization of interactions between PVP and indomethacin in amorphous molecular dispersions. Pharm Res 14(12):1691–1698.
12. Matsumoto T, Zografi G. 1999. Physical properties of solid molecular dispersions of indomethacin with poly(vinylpyrrolidone) and poly(vinylpyrrolidone-co-vinyl-acetate) in relation to indomethacin crystallization. Pharm Res 16(11):1722–1728.
13. Crowley KJ, Zografi G. 2002. Cryogenic grinding of indomethacin polymorphs and solvates: Assessment of amorphous phase formation and amorphous phase physical stability. J Pharm Sci 91(2):492–507.
14. Repka MA, Battu SK, Upadhye SB, Thumma S, Crowley MM, Zhang F, Martin C, McGinity JW. 2007. Pharmaceutical applications of hot-melt extrusion: Part II. Drug Dev Ind Pharm 33(10):1043–1057.
15. Savolainen M, Heinz A, Strachan C, Gordon KC, Yliruusi J, Rades T, Sandler N. 2007. Screening for differences in the amorphous state of indomethacin using multivariate visualization. Eur J Pharm Sci 30(2):113–123.
16. Swallen SF, Kearns KL, Mapes MK, Kim YS, McMahon RJ, Ediger MD, Wu T, Yu L, Satija S. 2007. Organic glasses with exceptional thermodynamic and kinetic stability. Science 315(5810):353–356.
17. Chokshi RJ, Sandhu HK, Iyer RM, Shah NH, Malick AW, Zia H. 2005. Characterization of physico-mechanical properties of indomethacin and polymers to assess their suitability for hot-melt extrusion process as a means to manufacture solid dispersion/solution. J Pharm Sci 94(11):2463–2474.
18. Yoshioka M, Hancock BC, Zografi G. 1995. Inhibition of indomethacin crystallization in poly(vinylpyrrolidone) coprecipitates. J Pharm Sci 84(8):983–986.
19. Hildebrand JH. 1916. Solubility. J Am Chem Soc 38:1452–1473.
20. Greenhalgh DJ, Williams AC, Timmins P, York P. 1999. Solubility parameters as predictors of miscibility in solid dispersions. J Pharm Sci 88(11):1182–1190.
21. Hansen CM. 1967. The three dimensional solubility parameter and solvent diffusion coefficient. Copenhagen, Denmark: Danish Technical Press.
22. Marsac PJ, Li T, Taylor LS. 2009. Estimation of drug–polymer miscibility and solubility in amorphous solid dispersions using experimentally determined interaction parameters. Pharm Res 26(1):139–151.
23. Xiang T-X, Anderson BD. 2012. Molecular dynamics simulation of amorphous indomethacin. Mol Pharm DOI: 10.1021/mp3000698.
24. Xiang TX, Anderson BD. 2004. A molecular dynamics simulation of reactant mobility in an amorphous formulation of a peptide in poly(vinylpyrrolidone). J Pharm Sci 93(4):855–876.
25. Gupta J, Nunes C, Vyas S, Jonnalagadda S. 2011. Prediction of solubility parameters and miscibility of pharmaceutical compounds by molecular dynamics simulations. J Phys Chem B 115(9):2014–2023.
26. Huynh L, Grant J, Leroux JC, Delmas P, Allen C. 2008. Predicting the solubility of the anti-cancer agent docetaxel in small molecule excipients using computational methods. Pharm Res 25(1):147–157.
27. Yang H, Li Z-S, Qian H-j, Yang Y-b, Zhang X-b, Sun C-c. 2004. Molecular dynamics simulation studies of binary blend miscibility of poly(3-hydroxybutyrate) and poly(ethylene oxide). Polymer 45(2):453–457.
28. Duan Y, Wu C, Chowdhury S, Lee MC, Xiong G, Zhang W, Yang R, Cieplak P, Luo R, Lee T, Caldwell J, Wang J, Kollman P. 2003. A point-charge force field for molecular mechanics simulations of proteins based on condensed-phase quantum mechanical calculations. J Comput Chem 24(16):1999–2012.
29. Miehlich B, Savin A, Stoll H, Preuss H. 1989. Results obtained with the correlation energy density functionals of Becke and Lee, Yang and Parr. Chem Phys Lett 157(3):200–206.
30. Pomelli CS, Tomasi J, Barone V. 2001. An improved iterative solution to solve the electrostatic problem in the polarizable continuum model. Theor Chem Acc 105(6):446–451.
31. Bayly CI, Cieplak P, Cornell W, Kollman PA. 1993. A well-behaved electrostatic potential based method using charge restraints for deriving atomic charges: The RESP model. J Phys Chem 97(40):10269–10280.
32. Cieplak P, Caldwell J, Kollman P. 2001. Molecular mechanical models for organic and biological systems going beyond the atom centered two body additive approximation: Aqueous solution free energies of methanol and N-methyl acetamide, nucleic acid base, and amide hydrogen bonding and chloroform/water partition coefficients of the nucleic acid bases. J Comput Chem 22(10):1048–1057.
33. Bühler V. 2008. Kollidon® Polyvinylpyrrolidone excipients for the pharmaceutical industry. 9th ed. Ludwigshafen, Germany: BASF SE.
34. Cheng HN, Smith TE, Vitus DM. 1981. Tacticity of poly(N-vinylpyrrolidone). J Polym Sci Polym Lett Ed 19:29.
35. Jorgensen WL, Chandrasekhar J, Madura JD, Impey RW, Klein ML. 1982. Comparison of simple potential functions for simulating liquid water. J Chem Phys 79:926–935.
36. Verlet L. 1967. Computer "experiments" on classical fluids. I. Thermodynamical properties of Lennard-Jones molecules. Phys Rev 159(1):98–103.
37. Berendsen HJC, Postma JPM, Van Gunsteren WF, DiNola A, Haak JR. 1984. Molecular dynamics with coupling to an external bath. J Chem Phys 81(8):3684–3690.
38. Ewald P. 1921. Die Berechnung optischer und elektrostatischer Gitterpotentiale. Ann Phys 64:253–287.
39. Humphrey W, Dalke A, Schulten K. 1996. VMD: Visual molecular dynamics. J Mol Graph 14(1):33–38.
40. Spyriouni T, Vergelati C. 2001. A molecular modeling study of binary blend compatibility of polyamide 6 and poly(vinyl acetate) with different degrees of hydrolysis: An atomistic and mesoscopic approach. Macromolecules 34:5306–5316.
41. Kasimova AO, Pavan GM, Danani A, Mondon K, Cristiani A, Scapozza L, Gurny R, Moller M. 2012. Validation of a novel molecular dynamics simulation approach for lipophilic drug incorporation into polymer micelles. J Phys Chem B 116(14):4338–4345.
42. Aceves-Hernandez JM, Nicolas-Vazquez I, Aceves FJ, Hinojosa-Torres J, Paz M, Castano VM. 2009. Indomethacin polymorphs: Experimental and conformational analysis. J Pharm Sci 98(7):2448–2463.
43. Donth E. 2001. The glass transition: Relaxation dynamics in liquids and disordered materials. Berlin, Germany: Springer Series in Material Science.
44. Khougaz K, Clas S-D. 2000. Crystallization inhibition in solid dispersion of MK-0591 and poly(vinylpyrrolidone) polymers. J Pharm Sci 89:1325–1334.
45. Barrat J-L, Baschnage J, Lyulin A. 2010. Molecular dynamics simulations of glassy polymers. Soft Matter 6:3430–3446.
46. Buchholz J, Paul W, Varnik F, Binder K. 2002. Cooling rate dependence of the glass transition temperature of polymer melts: Molecular dynamics study. J Chem Phys 117(15):7364–7372.
47. Boyd SU, Boyd RH. 2001. Chain dynamics and relaxation in amorphous poly(ethylene terephthalate): A molecular dynamics simulation study. Macromolecules 34:7219–7229.
48. Soldera A, Metatla N. 2006. Glass transition of polymers: Atomistic simulation versus experiments. Phys Rev E Stat Nonlin Soft Matter Phys 74(6 Pt 1):061803.
49. Gordon M, Taylor JS. 1952. Ideal co-polymers and the second order transitions of synthetic rubbers. I. Non-crystalline co-polymers. J Appl Chem 2:493–500.

RESEARCH ARTICLE – *Pharmaceutics, Drug Delivery and Pharmaceutical Technology*

Water Uptake, Distribution, and Mobility in Amorphous Poly(D,L-Lactide) by Molecular Dynamics Simulation

TIAN-XIANG XIANG, BRADLEY D. ANDERSON

Department of Pharmaceutical Sciences, College of Pharmacy, University of Kentucky, Lexington, Kentucky 40536

Received 27 September 2013; revised 23 December 2013; accepted 24 December 2013

Published online in Wiley Online Library (wileyonlinelibrary.com). DOI 10.1002/jps.23855

ABSTRACT: An explicit all-atom computational model for amorphous poly(lactide) (PLA) was developed. Molecular dynamics simulations of PLA glasses were conducted to explore various molecular interactions and predict certain physical properties. The density of a newly formed PLA glass aged for 100 ns at 298 K was 1.23 g/cm^3, close to the experimental range (1.24–1.25 g/cm^3). The glass transition temperature ($T_g = 364$ K) was higher than experimental values because of the fast cooling rate (0.03 K/ps) in the simulation. The solubility parameter (20.6 MPa$^{1/2}$) compared favorably to the literature. The water sorption isotherm obtained by relating the excess chemical potential of water in PLA to the Henry's law constant for water sorption was close to the experiment. At 0.6% (w/w), water molecules localize next to polar ester groups in PLA because of hydrogen bonding. Local mobility in PLA as characterized by the atomic fluctuation was sharply reduced near the T_g, decreasing further with aging at 298 K. The non-Einsteinian diffusion of water was found to correlate with the rotational β-relaxation of PLA C=O groups at 298 K. A relaxation–diffusion coupling model proposed recently by the authors gave a diffusion coefficient (1.3×10^{-8} cm^2/s at 298 K) which is comparable to reported experimental values. © 2014 Wiley Periodicals, Inc. and the American Pharmacists Association J Pharm Sci

Keywords: amorphous; diffusion; water sorption; glass; glass transition; materials science; mobility; molecular dynamics; polymers; solid-state stability

INTRODUCTION

The molecular events governing water uptake into pharmaceutical solids and the influence of moisture uptake on solid-state formulation properties have been recurring themes in the pharmaceutical literature for several decades. Current understanding in these areas rests to a significant extent on the pioneering research of Zografi and coworkers.[1–9] During a period when the development of high-energy amorphous drug dispersions has emerged as a key enabling technology to enhance oral bioavailability of poorly soluble drugs,[10] Zografi's explorations of the mechanisms of water uptake into amorphous solids and the role of water as a plasticizer to influence both physical and chemical stabilities have provided key insights. One of these was the notion that because of the disordered state of amorphous solids, "it is possible for water to dissolve in the solid," thus setting the stage for an increased appreciation within the pharmaceutical sciences community for the profound effects of water on such properties as the glass transition temperature (T_g) and changes in molecular mobility that may ultimately influence the degree of physical and chemical reactivity.[1] Because of the important impact of water on polymer properties and the stability of amorphous drug formulations, a significant body of work from Zografi and his coworkers also focused on the underlying water–polymer interactions.[2,3,7,8]

Molecular dynamics (MD) simulations are becoming increasingly useful for exploring molecular interactions that govern drug solubility, moisture uptake, and mobility in amorphous formulations. Ultimately, predictions from MD simulations may facilitate excipient selection and formulation design, activities that today require extensive and often costly trial-and-error experiments.[11–17] Work from our own laboratory has demonstrated the utility of MD simulations for understanding the nature of interactions that govern the dissolution of water in amorphous solids and the influence of water content on water cluster formation[11,12]; water mobility[11,12]; and the influence of drug–polymer interactions, drug concentration, and water content on phase miscibility and drug solubility in amorphous formulations.[16,17]

Recent years have witnessed a growing interest in the field of biodegradable polymers and, consequently, in computational activities to explore various molecular properties of biodegradable polymers.[18–21] Poly(lactide) (PLA) and its copolymers are among the most widely used synthetic biodegradable polymers for drug encapsulation and delivery with several products for controlled release of proteins or peptides on the market.[22–24] Biodegradable polymers such as PLA and its copolymers are also useful for applications in biotechnology (e.g., medical devices, implants, and tissue engineering), packaging, and other areas.[24–27]

Despite growing interest, explicit all-atom MD studies of such fundamental properties as water solubility, diffusivity, and distribution in PLA polymers are still lacking. This study is intended to develop a realistic molecular representation of an amorphous PLA solid that can then be useful for predicting PLA properties of pharmaceutical relevance such as the solubility parameter and structural relaxation parameters. In particular, using molecular structures and trajectories obtained from MD simulations, the moisture sorption isotherm of water in PLA and the heterogeneous distribution and diffusion coefficient of water in simulated PLA matrices have been characterized. These properties are of general importance in determining the stability of amorphous drug formulations and in this sense

---

Correspondence to: Bradley D. Anderson (Telephone: +859-218-6536; Fax: +859-257-2489; E-mail: bande2@email.uky.edu)

Journal of Pharmaceutical Sciences

© 2014 Wiley Periodicals, Inc. and the American Pharmacists Association

according to:

$$\delta = \sqrt{\mathrm{CED}} \tag{2}$$

By analogy with the Hansen method,[43] δ was decomposed into electrostatic (δ_{ele}) and van der Waals components (δ_{vdW}),

$$\delta^2 = \delta^2_{\mathrm{ele}} + \delta^2_{\mathrm{vdW}} = \frac{E_{\mathrm{ele}}}{V} + \frac{E_{\mathrm{vdW}}}{V} \tag{3}$$

where the electrostatic component δ_{ele} includes contributions from both polar and hydrogen bonding interactions. E_{v}, E_{ele}, and E_{vdW} in Eqs. (2) and (3) were calculated, respectively, from the differences of the total potential energies, electrostatic interaction energies, and van der Waals interaction energies for all molecules in the simulated assemblies and in a vacuum when they were infinitely separated from each other.

RESULTS AND DISCUSSION

Physical Properties of PLA Glass

The partial atomic charges for the ester groups in the present PLA model calculated using the combined methods of B3LYP/ccpVTZ30, IEFPCM, and RESP were 0.760 (C1), −0.564 (O1), and −0.542 (O2), respectively (Table 1). Using the 6–31G^* basis set and various partitioning schemes, Koller et al.[44] studied the atomic charge distributions in a series of methyl esters (methyl formate, methyl acetate, and methyl propionate) in the absence of a solvent model and found the charges for the carbonyl carbon and oxygen to be in a narrow range of 0.76–0.98 and −0.58 to −0.62, respectively, whereas that for the ether oxygen was −0.37 to −0.55. Aside from differences in chemical structure between PLA monomers and the model esters described above, different quantum-mechanical (QM) methods and solvent models were also employed. For example, Koller et al.[44] found that the inclusion of a reaction field to account for the medium effect lowered the energy of the ether oxygen–water complex perhaps because of a more pronounced polarization effect of the medium on the charge partitioning between the carbonyl and ether oxygen atoms. Klauda et al.[45] conducted full AM1 level calculations for methyl acetate and other model ester molecules, which served as the basis for optimization of the charges and other nonbonded parameters in more complex phospholipids, and obtained a set of partial charges for these three atoms of 0.48 (C1), −0.43 (O1), and −0.36 (O2). The QM method used in the present study is consistent with the Amber force field as described by Duan et al.[30] The partial charges for the terminal groups in PLA were judiciously assigned based on the present *ab initio* calculations and previous calculations of the same groups in other molecular species and the assumption of overall charge neutrality for each PLA polymer. For the terminal hydrogen atom covalently bonded to the –OCH– group in a PLA repeat unit to form an –OH group, the partial charge was set at a value of 0.36. A similar value (0.40) was assigned to the hydrogen atom for the hydroxyl group in heparin.[46] To maintain charge neutrality, the terminal –OH group attached to the terminal carbonyl group in a PLA repeat unit to form a –COOH group was assigned charge values of (−0.74 and 0.38). These are comparable to those obtained for acetic acid (−0.66 and 0.45) using the same *ab initio* method.

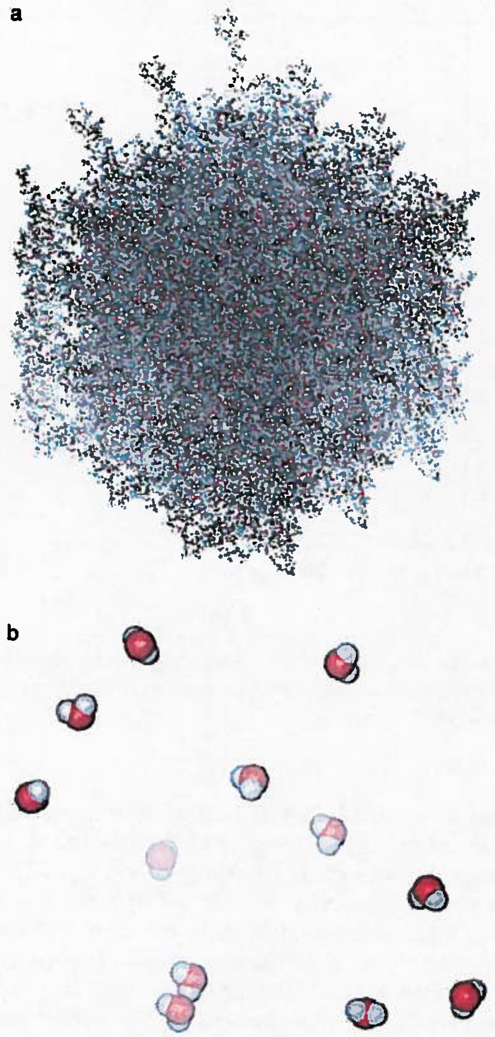

Figure 2. Images of a simulated structure for: (a) a newly formed amorphous PLA solid at 298 K (central and ±x, ±y, ±z image cells) and (b) the corresponding water distribution in the same assembly.

Because of the chiral nature of lactic acid (cf., Fig. 1), PLA polymers can exist in many different conformations differing in isomeric L/D content and sequence. The ratio of L- to D-lactic acid units influences the physical properties of PLA polymers.[47,48] Those having the greatest diversity in terms of isomeric conformation (i.e., L/D ~50:50) exist as amorphous solids that resist crystallization and may thereby be more suitable as formulation matrices for various pharmaceutical applications.[47] Thus, in this study, model PLA polymers comprising randomly distributed 50% L-lactic acid and 50% D-lactic acid units were built and used to construct PLA assemblies.

Once a PLA assembly was built and equilibrated at 600 K, the PLA melt was cooled to 200 K to form a glass at a cooling rate of 0.03 K/ps. Figure 2a shows a representative microstructure of a newly formed PLA glass at 298 K. The amorphous PLA exhibited an apparent T_g, as shown by the plot of density versus temperature (cf., Fig. 3) obtained during the cooling dynamic run. As noted in Figure 3, changes of density versus temperature were steeper at higher temperature, becoming more flat as temperature was lowered below 350 K. The T_g was determined from the intersection of straight-line fits above and below T_g.[13]

DOI 10.1002/jps.23855

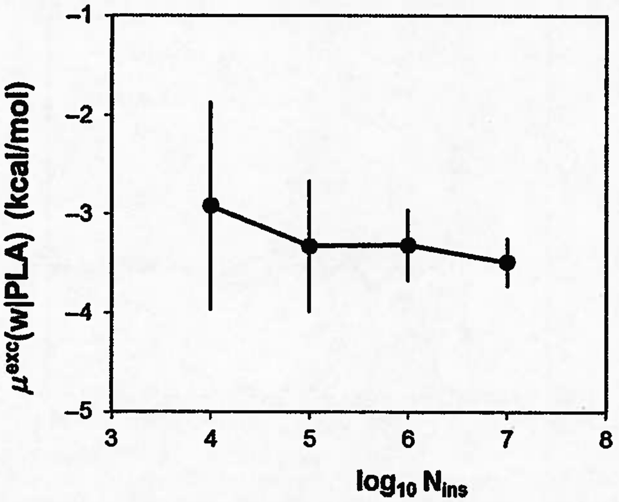

Figure 5. Variation of the excess chemical potential for water in a newly formed PLA glass at 298 K with the number of water molecules inserted.

of insertions with the excess chemical potential approaching $\mu^{exc}(w\,|\,PLA) = -3.4 \pm 0.2$ kcal/mol at $N_{ins} = 10^7$.

The excess chemical potential of a solute is intrinsically related to its solubility in the material of interest at a given vapor pressure. The theoretical representation for generalized solvation processes given by Ben-Naim and Marcus[57] was closely followed in the derivation of this relation. The chemical potential of water in a PLA glass at a given temperature and pressure can be expressed as

$$\mu(\mathrm{w|PLA}) = \mu^{exc}(\mathrm{w|PLA}) + RT\ln\left(\rho_{\mathrm{w/PLA}}\Lambda_{\mathrm{w}}^{3}q_{\mathrm{w/PLA}}^{-1}\right) \quad (4)$$

where R is the gas constant, $\rho_{\mathrm{w/PLA}}$ is the number density of water in PLA, and Λ_{w} and $q_{\mathrm{w/PLA}}$ are the translational and internal partition functions for water in PLA, respectively. By definition,[57] $\mu^{exc}(w\,|\,PLA)$ is the Gibbs free energy change for the introduction of water into PLA with the constraint that its center of mass is at a fixed position and can thus be considered as the excess chemical potential as derived from the particle insertion method of Widom[42] because of the interaction between the inserted water and surrounding PLA polymer molecules. A similar equation can be written for water in the vapor phase (v):

$$\mu(\mathrm{w|v}) = \mu^{exc}(\mathrm{w|v}) + RT\ln\left(\rho_{\mathrm{w/v}}\Lambda_{\mathrm{w}}^{3}q_{\mathrm{w/v}}^{-1}\right) \quad (5)$$

Consider now that water in the vapor phase is at equilibrium with water molecules absorbed within PLA:

$$\mu(\mathrm{w|PLA}) = \mu(\mathrm{w|v}) \quad (6)$$

Substituting Eqs. (4) and (5) into Eq. (6), we have

$$\mu^{exc}(\mathrm{w|PLA}) - \mu^{exc}(\mathrm{w|v}) = RT\ln(\rho_{\mathrm{w/v}}q_{\mathrm{w/PLA}}/\rho_{\mathrm{w/PLA}}q_{\mathrm{w/v}}) \quad (7)$$

For a similar equilibrium process between a saturated water vapor (v_s) and a pure liquid water (l) phase, we have

$$\mu^{exc}(\mathrm{w|l}) - \mu^{exc}(\mathrm{w|v_s}) = RT\ln(\rho_{\mathrm{w|v_s}}q_{\mathrm{w|l}}/\rho_{\mathrm{w|l}}q_{\mathrm{w|v_s}}) \quad (8)$$

Combining Eqs. (7) and (8) and assuming that the internal partition function is identical in the condensed PLA and water phases, $q_{\mathrm{w/l}} = q_{\mathrm{w/PLA}}$, we have

$$\begin{aligned}\delta\mu^{exc} &= \mu^{exc}(\mathrm{w|PLA}) - \mu^{exc}(\mathrm{w|l})\\ &= RT\left[\ln(\rho_{\mathrm{w/v}}/\rho_{\mathrm{w/v_s}}) + \ln(\rho_{\mathrm{w/l}}/\rho_{\mathrm{w/PLA}})\right]\end{aligned} \quad (9)$$

In the limit of low water-vapor pressure where the ideal gas approximation applies, one has the relation $\rho_{\mathrm{w/v}}/\rho_{\mathrm{w/vs}} = P/P_s$, where P and P_s are a given water vapor pressure and the saturated water vapor pressure at temperature T, respectively. Transforming the number density of water in PLA and pure liquid water in terms of mass density, one has $\rho_{\mathrm{w/PLA}}/\rho_{\mathrm{w/l}} = \phi_{\mathrm{w}}(d_{\mathrm{PLA}}/d_{\mathrm{l}})$, where ϕ_{w} is the water content by weight (g/g) in PLA and d_{PLA} and d_{l} are the mass densities of PLA polymer and pure liquid water, respectively. Substituting these results into Eq. (9) and assuming low-equilibrium water sorption where Henry's law applies, the sorption isotherm between water content (ϕ_{w}) and the relative humidity (RH = P/P_s) can be expressed as a linear relation:

$$\phi_{\mathrm{w}} = K(P/P_s) \quad (10)$$

where the Henry's constant, K, can be approximated as:

$$K = e^{-(\mu^{exc}(\mathrm{w|PLA}) - \mu^{exc}(\mathrm{w|l}))/RT}(d_{\mathrm{l}}/d_{\mathrm{PLA}}) \quad (11)$$

Consequently, the water sorption isotherm is uniquely determined by the constant K. The excess chemical potential of water ($\mu^{exc}(w\,|\,l) = -5.74$ kcal/mol) and density ($d_{\mathrm{l}} = 1.0$ g/cm^3) in pure liquid water have been reported in literature based on available experimental results.[58] Thus, the water sorption isotherm in PLA can be calculated from $\mu^{exc}(w\,|\,PLA)$ and d_{PLA} results obtained from the present MD simulations. The results are presented in Figure 6 along with those obtained experimentally[37] for comparison. The agreement is within the statistical uncertainty and both the computational and experimental results indicate a low level of water sorption in PLA (<2%, w/w, water content in the range of 0%–100% relative humidity), which can

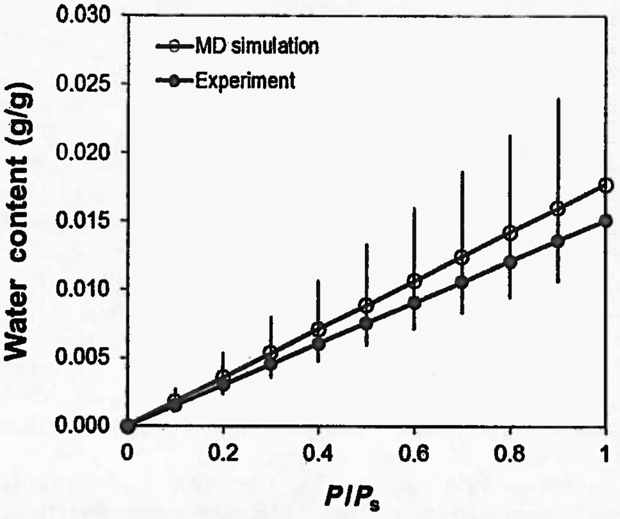

Figure 6. Comparison of water sorption isotherms in PLA at 298 K obtained by the present MD simulation and experiment.[37]

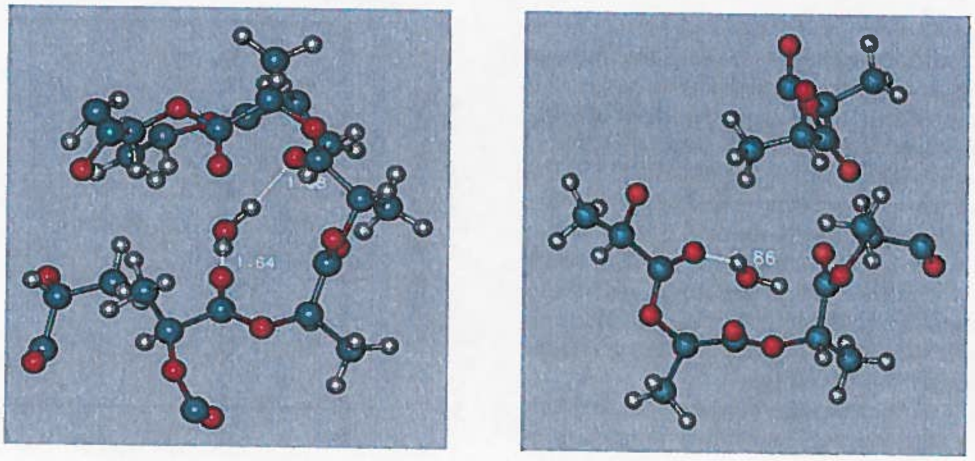

Figure 8. Representative hydrogen bonding configurations for a water molecule with neighboring PLA ester groups in the simulated PLA glass at 298 K: left, two HBs; and right, single HB.

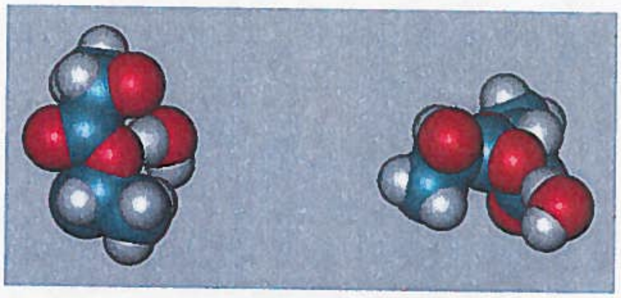

Figure 9. Space-filling representation of hydrogen bonding between a water molecule and a carbonyl (right) and ether group (left) in the simulated PLA glass. For clarity, only two adjacent lactic acid units in the simulated PLA along with the hydrogen bonded water molecule are displayed.

Table 2. Solubility Parameter $(\mathrm{MPa})^{1/2}$ for Simulated PLA Compared with Those for Some Other Common Materials

Substance	δ	δ_{vdW}	δ_{ele}
PLA	20.6^{a}	13.6^{a}	15.0^{a}
n-Hexane	14.9^{b}	14.9^{c}	0
Methyl acetate	18.7^{c}	15.5^{c}	10.5^{c}
Glucose	38.9^{c}	–	–
Water	47.9^{b}	15.6^{c}	45.2^{c}
Poly(ethylene)	16.2^{d}	–	–
PEG-4000	20.8^{e}	–	–
IMC	25.5^{f}	20.6^{f}	14.4^{f}

[a] Present MD study.
[b] Ref. 68.
[c] Ref. 69.
[d] Ref. 70.
[e] Ref. 71.
[f] Ref. 17.

ether oxygen atom is markedly limited compared with the carbonyl oxygen atom. Thus, it is this steric hindrance rather than the atomic charges that effectively excludes the ether oxygen atoms as hydration sites.[44] This is consistent with the experimental evidence that favors water binding at the carbonyl atom in some simple organic compounds.[44] No water molecules were hydrogen bonded to the terminal –OH groups perhaps because of the scarcity of these –OH groups compared with the rich abundance of ester groups in PLA. These results appear to be in contrast with the suggestion by Cairncross et al.[36] based on their sorption experimental observations that moisture sorption is controlled by hydrophilic end groups in PLA.[36,48]

Solubility Parameter for Amorphous PLA Solid

In the pharmaceutical industry, drug–excipient miscibility is commonly predicted by the solubility parameter method developed on the basis of Hildebrand's solubility theory,[14,64–66] even though recent studies have exposed this method's limitations for accurately predicting miscibility.[17,67] Differences in solubility parameters, $\Delta\delta$, of less than 7.0 $\mathrm{MPa}^{1/2}$ between materials have been considered as a criterion for compatible systems, whereas those with $\Delta\delta$ of greater than 10.0 $\mathrm{MPa}^{1/2}$ are considered likely to be immiscible with each other.[64] The solubility parameter for simulated PLA glass and its polar and nonpolar components were calculated from the present MD simulations and compared with some common materials in Table 2.

The shortcomings of the solubility parameter method may be attributed in part to the difficulty in determining solubility parameters experimentally. The reliability of various group contribution methods to estimate solubility parameters is still uncertain, especially in dealing with amorphous polymeric solids, as the group-contribution databases are usually based on experimental results for simple organic compounds. They ignore such factors as the internal conformational constraints pervasive in polymeric materials and changes in internal energy and density that accompany physical aging for thermodynamically nonequilibrium glassy solids.

Because of the widespread interest in using PLA polymers, the solubility parameter for PLA (δ_{PLA}) has been extensively studied. The results reported thus far in the literature vary over a range of 19–23 $\mathrm{MPa}^{1/2}$, partly because of the use of different PLA species and determination methods. Earlier, using Fedor's[72] group contribution method, Shogren[61] found a δ_{PLA} value of 22.7 $\mathrm{MPa}^{1/2}$. Karst and Yang[19] calculated the solubility parameter for PLA using various group contribution methods, obtaining an average δ_{PLA} of 20.2 $\mathrm{MPa}^{1/2}$. Using similar group contribution methods, Liu et al.[66] obtained δ_{PLA} of 23.3 $\mathrm{MPa}^{1/2}$. Schenderlein et al.[73] performed both the turbidity titration experiments and group contribution calculations for D,L-PLA and various poly(D,L-lactide-co-glycolide) copolymers and obtained

DOI 10.1002/jps.23855

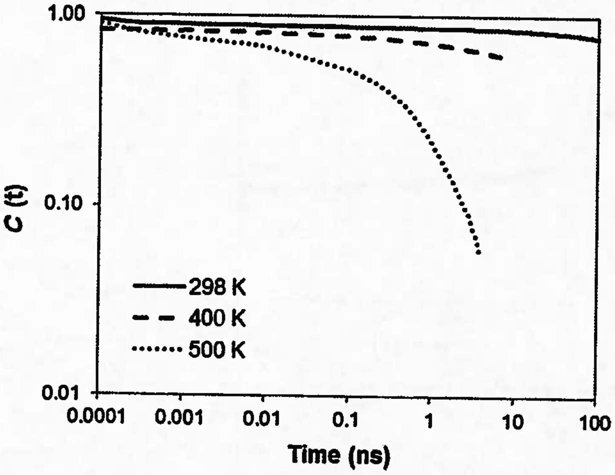

Figure 11. Averaged correlation functions for rotational relaxation of carbonyl groups (C=O) in the simulated PLA assemblies.

exponential function[83–85]:

$$C_{\mathrm{KWW}} = C_0 \exp[-(t/\tau)^{\beta}] \quad (12)$$

where τ and β are the central relaxation time and the stretching parameter, respectively. β varies between 0 and 1 and measures the broadness of the dynamic distribution. Thus, the correlation functions in Figure 11 were fitted with one (at $T > T_g$) or two (at $T < T_g$) KWW functions. The fitted β value for the α-process varied in a narrow range of 0.48–0.51 over 298–500 K, which is close to the β value of 0.51 for the α-process at 353 K in mostly amorphous PLA.[79] A much smaller β (0.23) was obtained for the fast decay at 298 K, suggesting a much broader distribution of relaxation modes for the β-process. Above T_g, the calculated relaxation times (τ) were 0.6 ns at 500 K and 67 ns at 400 K. A broad-band dielectric relaxation experiment by Mijovic and Sy[77] gave τ = ~0.3 ns at 452 K in amorphous L-PLA. At a sub-T_g temperature of 298 K, the τ values found from the simulations for the two decaying components were 0.2 ns and 84 μs, which are markedly smaller than those (~40 ns and >1 s) found for β- and α-processes in L-PLA glasses[77] or related L-PLA homopolymer networks.[78] The correlation time, 84 μs, for the slow decay is also smaller than that (0.03 s) found for the α-process in PLA (L/D = 80/20) at 323 K.[80] We note that the slow decay at 298 K is far from complete and τ and β are highly correlated with a small change in β leading to a large change in τ. Thus, the results at 298 K can only be considered as a rough estimation and an accurate determination would require a simulation time longer than more than 10 μs. Other factors such as differences in polymer L/D content, chain length, measurement subject, and preparative method (an extremely fast cooling rate is typical for simulations) may also contribute to the discrepancies between simulation and experiment results.

Water Diffusivity in PLA Glass

Molecular mobility in the simulated PLA polymers was further evaluated by monitoring the diffusivity of water. One of the major challenges to commercialization of bio-based polymers for some applications is their inferior moisture barrier properties compared with conventional synthetic polymers. Shogren[61] found that typical values of water vapor permeability (WVTR) for biodegradable polyesters (20–300 g/m^2 per day at 25°C) are much higher than those for polymers that display good barrier properties such as polyethylene (~1 g/m^2 per day). Furthermore, because PLA is hydrolytically degradable, the degree of water penetration during manufacturing, shipping, storage, and end use of PLA products determines the physicochemical stability of the polymer.[36] Thus, understanding moisture transport, which is usually characterized in terms of the solubility and diffusion coefficient of water in the polymer of interest, is extremely important. The experimental determination of water diffusivity in PLA is particularly challenging because it is difficult to separate the diffusion process from hydrolytic degradation, and as a result, accurate measurement of water transport requires analyzing the simultaneous diffusion/reaction processes.[48]

According to the Einstein relation,

$$D = \lim_{t\to\infty} D_t = \lim_{t\to\infty} \frac{< |r(t_0+t) - r(t_0)|^2 >}{6t} \quad (13)$$

where the angled brackets represent an ensemble average over all molecules of the same kind and time origins (t_0), solute diffusivity can be evaluated by monitoring the mean-squared displacement (MSD) over a sufficiently long time (t). The results for water molecules in the simulated PLA glass at 298 and 400 K are presented in the left panels of Figure 12 as log–log plots. The MSD plots as a whole failed to exhibit linear profiles with slopes of one as predicted from the Einstein relation. The degree of this non-Einsteinian behavior at different time intervals was assessed here by the slope (n) of a linear fit, or the following power law:

$$< |r(t_0+t) - r(t_0)|^2 \propto t^n \quad (14)$$

As shown in Figure 12, at 298 K, n varied from 0.34 at short times (<1 ns) to 0.62 within the latest time interval (up to 100 ns). Thus, water diffusion became less anomalous with time, though it remained non-Einsteinian at 100 ns. Similar non-Einsteinian behaviors have also been observed in another MD simulation of water diffusion in PLA,[86] though it was performed over a much shorter time scale (1 ns). The non-Einsteinian behaviors are greatly diminished above T_g as the n values approach one (0.95) at 400 K even within a shorter time frame of 10 ns.

To further understand the impact of non-Einsteinian behavior on the determination of water diffusivity, the diffusion results were analyzed in terms of the apparent diffusivity (D_t) as defined in Eq. (13) and shown in the right panels of Figure 12. If Einsteinian diffusion holds, D_t should be a constant independent of time. The decay of D_t over time shown in Figure 12 is thus reminiscent of the structural relaxation shown in Figure 11. In a recent MD study,[16] non-Einsteinian diffusion in glassy solids was attributed to structural relaxation and a relaxation-coupling diffusion model was formulated on the basis of this hypothesis:

$$D_t = D + C \exp[-(t/\tau)^{\beta}] \quad (15)$$

Interestingly, as shown in Figure 12, the use of the same KWW parameters (τ = 0.21 ns and β = 0.23) for the β-relaxation process involving PLA C=O rotations at 298 K gives a very

DOI 10.1002/jps.23855

use of a higher water content (2%, w/w, vs. 0.6%, w/w, in our present MD study). Discrepancies may also arise from: (1) experimental error (∼30%) as reported by Siparsky et al.,[48] (2) hydrolysis reactions in those experiments that deplete water molecules and may have significantly altered physicochemical properties of the underlying PLA polymers, and (3) insufficient equilibration time of the glassy polymers in the experimental measurements, which lends to non-Fickian diffusion as inferred from thickness-dependent diffusion coefficients,[88] and in the present MD simulations and other computational studies.

CONCLUSIONS

An explicit all-atom simulation model for PLA polymer was developed that is capable of approximately reproducing some important physical properties of amorphous PLA solids including material density, water sorption isotherm, and diffusion coefficient, thus verifying its potential utility in designing PLA-based drug delivery systems and in particular for predicting drug–PLA miscibility.[17] The combination of MD simulations, the particle insertion method of Widom,[42] and a theoretical sorption relation elucidated in this work was employed to calculate the water sorption isotherm in PLA. Weak sorption of water in amorphous PLA solids was predicted similar to experimental results. Inspection of molecular structures of the simulated PLA glasses provided further understanding of the distribution of water in PLA polymers that has been difficult to obtain experimentally. In particular, water molecules were found to be mostly separated from each other at a water content of 0.6% by weight, residing more favorably near the ester groups in PLA where they form HBs with carbonyl oxygen atoms. Water diffusion in the glassy PLA was found to exhibit non-Einsteinian behavior over the 100 ns simulation time, which could be modeled satisfactorily by a relaxation–coupling diffusion model using the same correlation time for β-relaxation of C=O groups in PLA. Above T_g, water diffusion became Einsteinian after a short non-Einsteinian decay period (<1 ns), a process that was shown to be distinct from the structural relaxation (α-process) of C=O groups in PLA at the same temperatures. Thus, the present study advances the relaxation–coupling diffusion model[16] by verifying that it is the β and/or related local relaxation processes that are mostly responsible for non-Einsteinian diffusion of water molecules in glassy polymers.

ACKNOWLEDGMENTS

Financial support for this project was obtained from the NSF I/UCRC Center for Pharmaceutical Development. We also thank the University of Kentucky Information Technology Department and Center for Computational Sciences for computing time on the Lipscomb High Performance Computing Cluster and for access to other supercomputing resources.

REFERENCES

1. Ahlneck C, Zografi G. 1990. The molecular basis of moisture effects on the physical and chemical stability of drugs in the solid state. Int J Pharm 62:87–95.

2. Oksanen CA, Zografi G. 1990. The relationship between the glass transition temperature and water vapor absorption by poly(vinylpyrrolidone). Pharm Res 7:654–657.

3. Hancock BC, Zografi G. 1993. The use of solution theories for predicting water vapor absorption by amorphous pharmaceutical solids: A test of the Flory–Huggins and Vrentas models. Pharm Res 10:1262–1267.

4. Hancock BC, Zografi G. 1994. The relationship between the glass transition temperature and the water content of amorphous pharmaceutical solids. Pharm Res 11:471–477.

5. Oksanen CA, Zografi G. 1993. Molecular mobility in mixtures of absorbed water and solid poly(vinylpyrrolidone). Pharm Res 10:791–799.

6. Shalaev EY, Zografi G. 1996. How does residual water affect the solid-state degradation of drugs in the amorphous state? J Pharm Sci 85:1137–1141.

7. Zhang J, Zografi G. 2000. The relationship between "BET"—And "free volume"—Derived parameters for water vapor absorption into amorphous solids. J Pharm Sci 89:1063–1072.

8. Taylor LS, Langkilde FW, Zografi G. 2001. Fourier transform Raman spectroscopic study of the interaction of water vapor with amorphous polymers. J Pharm Sci 90:888–901.

9. Newman AW, Reutzel-Edens SM, Zografi G. 2007. Characterization of the "hygroscopic" properties of active pharmaceutical ingredients. J Pharm Sci 97:1047–1059.

10. Hancock BC, Zografi G. 1997. Characteristics and significance of the amorphous state in pharmaceutical systems. J Pharm Sci 86:1–12.

11. Xiang TX, Anderson BD. 2004. A molecular dynamics simulation of reactant mobility in an amorphous formulation of a peptide in poly(vinylpyrrolidone). J Pharm Sci 93:855–876.

12. Xiang TX, Anderson BD. 2005. Distribution and effect of water content on molecular mobility in poly(vinylpyrrolidone) glasses: A molecular dynamics simulation. Pharm Res 22:1205–1214.

13. Barrat JL, Baschnagel J, Lyulin A. 2010. Molecular dynamics simulations of glassy polymers. Soft Matter 6:3430–3446.

14. Gupta J, Nunes C, Vyas S, Jonnalagadda S. 2011. Prediction of solubility parameters and miscibility of pharmaceutical compounds by molecular dynamics simulations. J Phys Chem B 115:2014–2023.

15. Huynh L, Grant J, Leroux JC, Delmas P, Allen C. 2008. Predicting the solubility of the anti-cancer agent docetaxel in small molecule excipients using computational methods. Pharm Res 25:147–157.

16. Xiang TX, Anderson BD. 2013. Molecular dynamics simulation of amorphous indomethacin. Mol Pharm 10:102–114.

17. Xiang T-X, Anderson BD. 2013. Molecular dynamics simulation of amorphous indomethacin-poly(vinylpyrrolidone) glasses: Solubility and hydrogen bonding interactions. J Pharm Sci 102:876–891.

18. Ahmad S, Johnston BF, Mackay SP, Schatzlein AG, Gellert P, Sengupta D, Uchegbu IF. 2010. In silico modelling of drug–polymer interactions for pharmaceutical formulations. J Roy Soc Interface 7:S423–S433.

19. Karst D, Yang Y. 2005. Using the solubility parameter to explain disperse dye sorption on polylactide. J Appl Polym Sci 96:416–422.

20. Kasimova AO, Pavan GM, Danani A, Mondon K, Cristiani A, Scapozza L, Gurny R, Möller M. 2012. Validation of a novel molecular dynamics simulation approach for lipophilic drug incorporation into polymer micelles. J Phys Chem B 116:4338–4345.

21. Wang YC, Ju SP, Jung T, Wang HH. 2011. Modeling of polyethylene, poly(L-lactide), and CNT composites: A dissipative particle dynamics study. Nanoscale Res Lett 6:433.

22. Fredenberg S, Wahlgren M, Reslow M, Axelsson A. 2011. The mechanisms of drug release in poly(lactic-co-glycolic acid)-based drug delivery systems—A review. Int J Pharm 415:34–52.

23. Hans ML, Lowman AM. 2002. Biodegradable nanoparticles for drug delivery and targeting. Curr Opin Solid St M 6:319–327.

24. Kumari A, Yadav SK, Yadav SC. 2010. Biodegradable polymeric nanoparticles based drug delivery systems. Colloid Surface B 75:1–18.

25. Auras R, Harte B, Selke S. 2004. An overview of polylactides as packaging materials. Macromol Biosci 4:835–864.

26. Auras RA, Lim LT, Selke SEM, Tsuji H, Eds. 2011. Poly(lactic acid): Synthesis, structures, properties, processing, and applications. New York: John Wiley & Sons.

DOI 10.1002/jps.23855

75. Götze W. 2009. Complex dynamics of glass-forming liquids: A mode-coupling theory. Oxford, UK: Oxford University Press.
76. Dionisio M, Viciosa MT, Wang Y, Mano JF. 2005. Glass transition dynamics of poly(L-lactic acid) during isothermal crystallisation monitored by real-time dielectric relaxation spectroscopy measurements. Macromol Rapid Commun 26:1423–1427.
77. Mijovic J, Sy JW. 2002. Molecular dynamics during crystallization of poly(L-lactic acid) as studied by broad-band dielectric relaxation spectroscopy. Macromolecules 35:6370–6376.
78. Serra RSI, Ivirico JLE, Duenas JMM, Balado AA, Ribelles JLG, Sanchez MS. 2009. Segmental dynamics in poly(e-caprolactone)/poly(L-lactide) copolymer networks. J Polym Sci B Polym Phys 47:183–193.
79. Shinyama K, Oi T, Fujita S. 2012. Dielectric relaxation phenomena of polylactic acid with β-crystalline chitin. Int J Polym SciVolume 2012: Article ID 389491.
80. Mierzwa M, Floudas G, Dorgan J, Knauss D, Wegner J. 2002. Local and global dynamics of polylactides. J Non-Cryst Solids 207–310:296–303.
81. Bedrov D, Smith GD. 2005. Molecular dynamics simulation study of the α- and β-relaxation processes in a realistic model polymer. Phys Rev E 71:050801.
82. Smith GD, Bedrov D. 2007. Relationship between the α- and β-relaxation processes in amorphous polymers: Insight from atomistic molecular dynamics simulations of 1,4-polybutadiene melts and blends. J Polym Sci B Polym Phys 45:627–643.
83. Kohlrausch R. 1854. Theorie des electrischen Ruckstandes in der Leidner Flasche. Pogg Ann Phys Chem 91:179–214.
84. Williams G, Watts DC. 1970. Non-symmetrical dielectric relaxation behavior arising from a simple empirical decay function. Trans Faraday Soc 66:80–85.
85. Williams G, Watts DC, Dev SB, North AM. 1971. Further considerations of non symmetrical dielectric relaxation behaviour arising from a simple empirical decay function. Trans Faraday Soc 67:1323–1335.
86. Entrialgo-Castaño M, Salvucci AE, Lendlein A, Hofmann D. 2008. An atomistic modeling and quantum mechanical approach to the hydrolytic degradation of aliphatic polyesters. Macromol Sy 269:47–64.
87. Gautieri A, Mezzanzanica A, Motta A, Redealli A, Vesentini A. 2012. Atomistic modeling of water diffusion in hydrolytic biomaterials. J Mol Model 18:1495–1502.
88. Sharp JS, Forrest JA, Jones RAL. 2001. Swelling of poly(D,L-lactide) and polylactide-co-glycolide in humid environments. Macromolecules 34:8752–8760.

molecular pharmaceutics
Article
pubs.acs.org/molecularpharmaceutics

Investigating Miscibility and Molecular Mobility of Nifedipine-PVP Amorphous Solid Dispersions Using Solid-State NMR Spectroscopy

Xiaoda Yuan, Diana Sperger, and Eric J. Munson*

Department of Pharmaceutical Sciences, College of Pharmacy, University of Kentucky, 789 South Limestone Street, Lexington, Kentucky 40536, United States

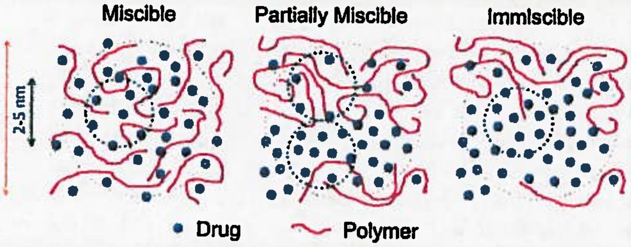

ABSTRACT: Solid-state NMR (SSNMR) ^{1}H T_1 and $T_{1\rho}$ relaxation times were used to evaluate the miscibility of amorphous solid dispersions of nifedipine (NIF) and polyvinylpyrrolidone (PVP) prepared by three different methods: melt quenching in the typical lab setting, spray drying and melt quenching in the NMR rotor while spinning. Of the five compositions prepared by melt quenching in the lab setting, the 95:5 and 90:10 NIF:PVP (w:w) amorphous solid dispersions were not miscible while 75:25, 60:40, and 50:50 NIF:PVP dispersions were miscible by the ^{1}H $T_{1\rho}$ measurements. The domain size of the miscible systems was estimated to be less than 4.5 nm. Amorphous solid dispersions with composition of 90:10 NIF:PVP prepared by spray drying and melt quenching in the NMR rotor showed miscibility by ^{1}H $T_{1\rho}$ values. Variable-temperature SSNMR ^{1}H $T_{1\rho}$ relaxation measurements revealed a change in relaxation time at approximately 20 °C below T_g, suggesting increased molecular mobility above that temperature.

KEYWORDS: *solid-state NMR, amorphous, solid dispersion, miscibility, relaxation time, nifedipine, PVP*

■ INTRODUCTION

Formulation of oral solid dosage forms using the amorphous form of the active pharmaceutical ingredient (API) is a strategy used to enhance the bioavailability of poorly water-soluble compounds, as the amorphous API has higher apparent solubility and faster dissolution rate than its crystalline counterpart.[1,2] However, amorphous materials possess higher free energies and have the risk of converting to the crystalline state, which is thermodynamically more stable. To overcome physical instability, a polymer can be mixed with the amorphous API to form an amorphous solid dispersion, which has been shown to significantly delay the onset of crystallization.[3−5] The two main processes that are commonly used to commercially prepare amorphous solid dispersions are spray drying and hot-melt extrusion. These two methods use different approaches to accomplish the preparation of stable amorphous dispersions and are most closely mimicked at the laboratory scale using a mini spray dryer or a melt-quenching approach.

There have been extensive discussions in the literature about the mechanisms of physical stabilization of amorphous solid dispersions, including reduction in the thermodynamic driving force toward crystallization, increase in crystallization energy barrier, disruption/formation of molecular interactions, and combinations of these factors.[6] Regardless of the specific mechanism, it is generally agreed that molecular-level miscibility is necessary to achieve maximum stabilization.[7,8] Immiscibility between drug and polymer has been reported to have led to increased crystallization rate of amorphous drugs.[9,10] Herein, the term miscibility describes a single-phase amorphous system in which the API is supersaturated in the polymer and the components are intimately mixed at the molecular level. The API does not necessarily exhibit equilibrium solubility in the polymer.[10]

Currently, the most common method to determine whether the API and polymer are miscible is by measuring the glass transition temperature (T_g) of the mixture using differential scanning calorimetry (DSC). A miscible system is characterized by a single glass transition temperature intermediate to those of the API and polymer, as opposed to two separate glass transition temperatures in a phase-separated system. However, it has been reported in the literature that it is possible to observe a single T_g in a phase-separated system[11,12] and vice versa.[13] In addition, Raman mapping has been used to access phase homogeneity of amorphous solid dispersions.[12] The method, however, is limited by the low spatial resolution as the step size is typically on the micrometer scale. Thus, a mixture that appears to be homogeneous using one technique may be found heterogeneous using another technique with a finer detection limit. For example, when T_g is used to assess miscibility, a detection limit of about 20−30 nm is generally assumed and domain sizes smaller than that are indistinguishable by DSC.[14−16] Thus, a method to accurately measure the miscibility between API and polymer of smaller domain sizes is

Received: August 20, 2013
Revised: October 25, 2013
Accepted: November 20, 2013
Published: November 20, 2013

ACS Publications © 2013 American Chemical Society

chemical degradation of nifedipine was observed by ^{1}H NMR in solutions of DMSO-d_6.

A 90:10 (w:w) nifedipine:PVP amorphous dispersion was prepared by melt quenching in an NMR rotor while spinning. To prepare amorphous dispersions via this method, appropriate mixture of drug and polymer was ball milled for 10 min to obtain optimum mixing. The ball-milled mixture was then transferred into a 7.5 mm zirconia NMR rotor with Teflon end-caps. The rotor was heated in the NMR probe equipped with a variable-temperature accessory stack (Varian, Palo Alto, CA) at 180 °C for 30 min while spinning at 4 kHz. The rotor was then rapidly cooled to room temperature, resulting in the amorphous dispersion.

A 90:10 (w:w) nifedipine:PVP amorphous dispersion was also prepared by spray drying using a Büchi Mini Spray Dryer B-290 (Büchi, Switzerland) equipped with 0.7 mm nozzle. Compressed nitrogen gas was used for atomization at a flow rate of 10 L/min. The drug and polymer were dissolved in methanol to form a solution with solid concentration of 13 mg/mL. The feed rate was set at 22.5 mL/min. The inlet temperature was set at 120 °C, and the corresponding outlet temperature was 49 °C. All amorphous dispersions were stored in glass vials over Drierite in the freezer when not analyzed.

Modulated DSC. The glass transition temperature (T_g) of nifedipine–PVP solid dispersions was determined by modulated DSC (MDSC) using a Q2000 differential scanning calorimeter equipped with an RCS90 refrigerated cooling system (TA Instruments, Newcastle, DE). Nitrogen gas was used as the purge gas at a flow rate of 50 mL/min. Temperature and enthalpy were calibrated using indium. Samples (2–5 mg) prepared by melt quenching as described above were placed in TZero aluminum pans and sealed with TZero aluminum hermetic lids with one pinhole (TA Instruments, New Castle, DE). Samples were equilibrated at 0 °C, and then heated at 1 °C/min to 200 °C with an amplitude of ±0.5 °C and a modulation period of 60 s. The glass transition was separated into the reversing heat flow signal and was determined by half height at midpoint using the Universal Analysis software (TA Instruments, Newcastle, DE).

Solid-State NMR ^{1}H T$_1$ and T$_{1\rho}$ Relaxation Measurements. All solid-state NMR spectra were acquired using a Tecmag Redstone HF3 2RX spectrometer (Tecmag, Inc., Houston, TX), operating at 75.48 MHz for ^{13}C (7 T static magnetic field). Samples were packed into 7.5 mm zirconia rotors and sealed with Teflon or Kel-F end-caps (Revolution NMR, LLC, For Collins, CO). Experiments were performed using a 7.5 mm double-resonance MAS probe (Varian, Palo Alto, CA). All ^{13}C spectra were acquired under magic angle spinning (MAS)[39] at 4 kHz, using ramped-amplitude CP,[40] total sideband suppression (TOSS)[41] and SPINAL64 decoupling[42] with a ^{1}H decoupling field of about 62 kHz. A 2 ms contact time was used in all experiments. 3-Methylglutaric acid was used to optimize spectrometer settings and was used as an external standard, with the methyl peak referenced to 18.84 ppm.[43] All experiments were conducted at room temperature, if not otherwise specified.

^{1}H T$_1$ relaxation values were measured using the saturation-recovery experiment through ^{13}C observation. The reason to observe ^{13}C is to provide information on the relaxation behavior of the protons that belong to each of the individual compounds. A 90° pulse width of about 4 μs was used in the experiment. In the Fourier-transformed spectrum, the peak of interest was integrated and plotted against recovery delay times and the values were fitted to the following equation using GraphPad Prism (GraphPad Software, Inc., La Jolla, CA)

$$M = M_0(1 - e^{-\tau/T_1}) \qquad (2)$$

where M is the integrated signal intensity and τ is the recovery delay time. M_0 is an amplitude parameter from the fit, and T$_1$ is the obtained spin–lattice relaxation time.

^{1}H T$_{1\rho}$ relaxation times were measured by varying the spin-lock duration time following a 90° pulse. A recycle delay of about 1.5–2 times the measured T$_1$ was used to maximize the signal-to-noise ratio. A frequency field of about 65 kHz was used for the spin-lock field. The peak of interest was integrated and plotted against the recycle delay times and the values were fitted to the following equation using GraphPad Prism (GraphPad Software, Inc., La Jolla, CA)

$$M = M_0\, e^{-\tau/T_{1\rho}} \qquad (3)$$

where M is the integrated signal intensity and τ is the spin-lock duration time. M_0 is an amplitude parameter from the fit, and T$_{1\rho}$ is the obtained spin–lattice relaxation time in the rotating frame.

Variable-Temperature Solid-State NMR. ^{1}H T$_{1\rho}$ relaxation times were determined as a function of temperature using a variable-temperature accessory stack (Varian, Palo Alto, CA). Lead nitrate was used to calibrate the temperature prior to the experiment.[44] A linear slope of 0.75 was obtained for the temperature range between 20 and 180 °C, agreeing very well with literature reported value.[44] Samples were equilibrated at each temperature for at least 15 min before data acquisition. ^{1}H T$_{1\rho}$ values were determined at 20, 40, 60, 70, 80, 90, and 100 °C for nifedipine and PVP amorphous solid dispersions of various weight ratios made by melt quenching in the lab setting.

■ RESULTS

Modulated DSC. Figure 2a shows the MDSC thermograms of NIF, PVP and five compositions of NIF:PVP amorphous solid dispersions (95:5, 90:10, 75:25, 60:40, 50:50) made by melt quenching in the lab setting. Only the reversing heat flow is plotted to show the glass transition event. NIF showed a T_g at 42 °C and a recrystallization event at 78 °C, followed by the melting at 172 °C. The 95:5 and 90:10 dispersions showed similar thermal events, with T_g, recrystallization, and melting all being observed. The thermogram of the 75:25 dispersion was different from the previous three thermograms in that there was no observable change in the heat capacity above T_g. A small melting peak was observed at 168 °C. The 60:40 and 50:50 dispersions showed no change of heat capacity or melting peaks above T_g. All five compositions showed single T_g values which was in agreement with previous reports.[38] Figure 2b shows the MDSC reversing signal of 90:10 NIF:PVP (w:w) dispersions prepared by all three methods (spray drying, melt quenching in the NMR rotor during spinning, and melt quenching in the lab). A single T_g was observed by all three samples and the thermal events were consistent with each other. As expected, two separate T_g events were observed for the 50:50 NIF:PVP physical mixture, corresponding to the respective glass transition temperatures of the drug and the polymer (data not shown).

The Gordon–Taylor equation (eq 4) can be used to estimate the T_g of an ideal binary mixture,[45] Table 1. ^{1}H T_1 and $T_{1\rho}$ Relaxation Times of Different Forms of NIF, PVP, and the 50:50 NIF:PVP Physical Mixture (PM)[a]

	nifedipine				50:50 NIF:PVP PM	
	α	β	amorphous	PVP	NIF	PVP
^{1}H T_1 (s)	32.4 (0.5)	13.0 (0.4)	4.2 (0.1)	2.1 (0.04)	3.6 (0.07)	2.1 (0.04)
^{1}H $T_{1\rho}$ (ms)	287 (6)	190 (6)	79.3 (0.1)	27.3 (0.3)	88 (3.5)	16.0 (0.4)

[a] The numbers in parentheses indicate the standard error associated with the fit.

adopt a range of molecular conformations. As a result, amorphous nifedipine had the shortest relaxation times, as expected. Among the two crystalline forms of nifedipine, α has been shown as the stable polymorph,[47,49] which in this case coincided with our relaxation time measurements.

Also shown in Table 1 are the relaxation times of the two components present in the 50:50 NIF:PVP physical mixture in the amorphous state. As evident in the table, nifedipine had different relaxation times than PVP in both ^{1}H T_1 and $T_{1\rho}$ measurements. The relaxation times of nifedipine and PVP in the physical mixture were similar to the values measured in their pure forms. These results showed that the physical mixture of nifedipine and PVP was not mixed on the molecular level.

Because the relaxation times are very sensitive to small changes in water content, the differences in the relaxation times between nifedipine and PVP were compared, rather than their absolute values. Ideally, relaxation time is a weighted arithmetic mean of the two components in a miscible system. However, water is known to decrease the relaxation time if present in a system.[48]

^{13}C SSNMR spectra of NIF-PVP amorphous solid dispersions prepared by melt quenching in the lab setting are shown in Figure 5. All the spectra had broad peaks, consistent with the amorphous nature of the samples. For pure amorphous nifedipine (or PVP), a single proton relaxation time (T_1 and $T_{1\rho}$) was observed regardless of the resonances used for the integration, as expected due to rapid proton spin diffusion in the solid state. Thus, any peak from one component that does not overlap with peaks from the other component can be used to calculate the relaxation times of the component of interest in the solid dispersion. Thus, the peaks around 175 and 43 ppm were chosen to calculate the relaxation times of PVP because there was no interference from nifedipine peaks in the same region. Likewise, the peaks at approximately 167, 148, and 103 ppm were chosen for nifedipine because they do not overlap with peaks from PVP.

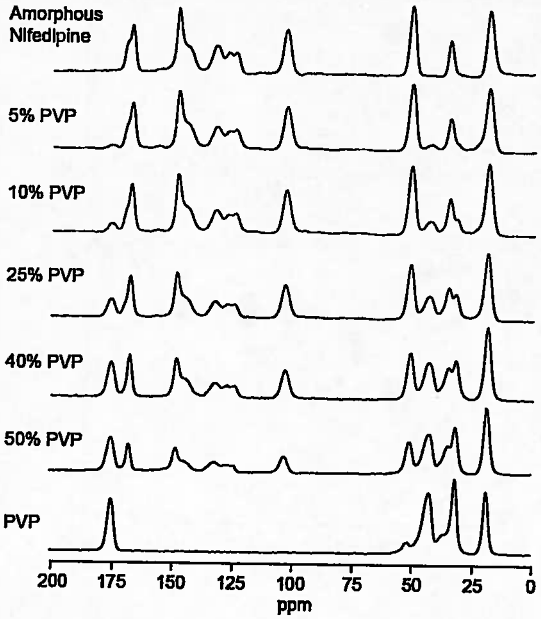

Figure 5. ^{13}C SSNMR spectra of NIF-PVP amorphous solid dispersions prepared by melt quenching in the lab setting containing 0, 5, 10, 25, 40, 50, and 100% PVP (from top to bottom).

The ^{1}H T_1 and $T_{1\rho}$ relaxation times of nifedipine and PVP in the amorphous solid dispersions prepared by melt quenching in the lab setting are shown in Table 2, and the differences of the relaxation times between nifedipine and PVP are plotted in Figure 6. There were no obvious differences in ^{1}H T_1 values between nifedipine and PVP in the amorphous solid dispersions except the 95:5 NIF:PVP composition. As shown in Figure 6a, no obvious trend could be seen in the plot of ^{1}H T_1 differentials. The similar ^{1}H T_1 relaxation times indicated that nifedipine and PVP were miscible on the 20−50 nm length scale. This was consistent with modulated DSC measurements that showed single T_g values for these samples, since DSC generally assumes a distinguishable domain size of 30 nm.[11] The 95:5 and 90:10 NIF:PVP compositions were on the borderline of being miscible as the confidence intervals did not or barely touched the zero horizontal line. It is interesting that the 95:5 and 90:10 were the two compositions that showed the large recrystallization peaks in the DSC.

^{1}H $T_{1\rho}$ relaxation times, on the other hand, were different for the drug and polymer for the 95:5 and 90:10 compositions. There was also a clear trend of decreasing differentials with increasing PVP content, as shown in Figure 6b. The ^{1}H $T_{1\rho}$ relaxation times indicated that the compositions with 25%, 40% and 50% PVP were miscible on the 2−5 nm length scale. The combination of ^{1}H T_1 and ^{1}H $T_{1\rho}$ relaxations times indicated that the two compositions with higher drug loadings were immiscible on the 2−5 nm length scale and might be borderline miscible on the 20−50 nm length scale. The three compositions with lower drug loadings were miscible on the 2−5 nm length scale. The biggest domain size was estimated to be 4.5 nm for those three miscible compositions using eq 1 with a ^{1}H $T_{1\rho}$ value of 35 ms. D was assumed to be 10^{-12} cm^2/s.[19]

Miscibility by SSNMR for Samples Prepared by Other Methods. ^{1}H T_1 and $T_{1\rho}$ values were also obtained for the 90:10 NIF:PVP amorphous solid dispersions prepared by two other methods: spray drying and melt quenching in the NMR rotor while spinning. The results are shown in Table 3. The ^{1}H $T_{1\rho}$ values suggested that the dispersions made by spray drying and melt quenching in the NMR rotor during spinning were miscible while the dispersion made by simple melt quenching in the lab setting was not. The ^{1}H $T_{1\rho}$ values of the dispersion made by melt quenching in the NMR rotor were large compared to the values of the other two dispersions. This is due to the dryness of the sample prepared in this method as the indicated there was a dramatic increase in the molecular mobility starting at about 20 °C below T_g of the dispersion. Aso and co-workers have studied the molecular mobility of amorphous nifedipine using ^{13}C SSNMR relaxation measurements and also found out a marked decreased in ^{13}C $T_{1\rho}$ at 20 °C below T_g.[50] Our results showed that a similar trend existed in the ^{1}H $T_{1\rho}$ of amorphous solid dispersions as well. The increase of molecular mobility below T_g is likely an underlying reason for increased structural relaxation and crystallization of amorphous systems reported by a number of studies. Wang and Pikal observed maximum structural relaxation at 15–20 °C below T_g for amorphous sodium ethacrynate/sucrose system.[51] Ishida and co-workers have observed increased crystal growth rate of amorphous nifedipine near and below T_g.[37] These reports are consistent with our findings and may suggest that the increased molecular mobility in the sub-T_g range plays an important role in the stability of amorphous systems.

■ DISCUSSION

Miscibility of Nifedipine and PVP. It has been reported by Taylor and co-workers that spin-coated films of nifedipine and PVP can form molecular level dispersions over all compositions based on IR detection of drug-polymer hydrogen bonding in the nifedipine NH moiety.[38] Taylor and co-workers have also calculated the interaction parameter (χ) between nifedipine and PVP (K12) to be −3.8 using a melting point depression method.[7] The fairly large negative value indicated mixing was favored; however, the result obtained through this method only applied to temperatures close to the melting temperature of the drug. This has apparently limited its practical usage, as storage temperatures are typically much lower than the melting point of the drug and the phase behavior of the drug-polymer mixture could be different at different temperatures.

Hydrogen bonding between nifedipine and PVP has also been studied by Aso and Yoshioka using ^{13}C NMR spin–lattice (T_1) relaxation time.[32] It was found that the T_1 of both PVP (carbonyl carbon) and nifedipine (dihydropyridine ring carbon adjacent to nitrogen) increased in the solid dispersion compared to the polymer or drug alone. The result suggested reduced motions of these functional groups, which were ascribed to hydrogen bonding between PVP carbonyl and nifedipine NH. Interestingly, the increase of T_1 of nifedipine carbons plateaued at about 40% (w:w) PVP, coinciding with the level of PVP to make miscible dispersions in our findings. It was also found that the chemical shift of PVP carbonyl carbon increased by about 1 ppm as the drug content increased,[32] which is usually an indication of hydrogen bond formation. In our own SSNMR spectra, we have also observed about 1 ppm downfield chemical shift change of the carbonyl carbon of PVP between neat PVP (175.1 ppm) and the dispersion with up to 95% nifedipine (175.9 ppm) (Table 4). The similar chemical shift change observed in our study indicates that the extent of hydrogen bonding interactions in our dispersion samples was similar to the samples prepared by Aso and Yoshioka, which in turn suggests that the existence of hydrogen bonds alone was not enough to demonstrate complete miscibility. It is likely that in the high drug content dispersions, some population of the drug was hydrogen bonded with PVP and thus being molecularly dispersed, while the rest of the drug formed small clusters of roughly 5–20 nm in size.

Table 4. Chemical Shift of the Carbonyl Carbon of PVP in Various NIF:PVP Amorphous Solid Dispersions of Different Compositions

NIF:PVP dispersion	ppm
neat PVP	175.1
50:50	175.4
60:40	175.6
75:25	175.7
90:10	175.8
95:5	175.9

Hydrogen bonding interaction at the nifedipine NH was also probed using ^{15}N solid-state NMR CPMAS. However, no significant change in chemical shift was found among crystalline NIF, amorphous NIF and the dispersions. It has been reported in the case of acetaminophen-PVP amorphous dispersions that ^{14}N SSNMR showed differences in chemical shift between neat drug and dispersion, while ^{15}N SSNMR did not show any difference in chemical shift.[52] This finding suggests that ^{14}N chemical shift is more sensitive to hydrogen bonding interactions than ^{15}N in some cases and it is very likely to have the same ^{15}N chemical shift while having different hydrogen bonding interactions. Since ^{14}N is a quadrupolar nucleus with complicated line shapes, we are currently exploring the feasibility of performing ^{14}N SSNMR on these systems.

Preparation Methods. In this study, the main focus was to investigate the melt-quench mixtures prepared as might be done in a laboratory setting. Because the melting point of crystalline nifedipine was 173 °C and the T_g of PVP was around 160 °C, it was determined that heating a ball milled mixture of crystalline nifedipine and PVP to 180 °C for 30 min would result in a uniformly mixed melt. Because PVP was still very viscous at 180 °C, the concern at higher PVP concentrations was that the drug would not adequately diffuse into PVP, and so a low limit of 50% drug was used for this study.

It was found in this study that 95:5 and 90:10 NIF:PVP dispersions prepared by melt quenching in the lab setting were not intimately mixed at the molecular level. However, 90:10 NIF:PVP dispersions prepared by the other two methods, spray drying and melt quenching in the NMR rotor during spinning, produced miscible systems as indicated by the common ^{1}H $T_{1\rho}$ relaxation times. The DSC thermograms of both dispersions showed recrystallization peaks between 100 and 115 °C, similar to the recrystallization behavior of the 90:10 dispersion made by melt quenching in the lab setting.

It is known that preparation methods affect the crystallization tendency of amorphous state materials. Strachan and co-workers have compared amorphous indomethacin prepared by melt quenching, spray drying, ball-milling, and cryo-milling and found differences in the recrystallization rate among the samples.[53] Our study demonstrated that, on the molecular level, the ability to form a miscible amorphous solid dispersion also depended on the preparation methods. It is likely that the 90:10 solid dispersion made by melt quenching in the lab setting will phase separate and thus crystallize over time faster than the other two dispersions of the same composition but prepared differently.

■ CONCLUSIONS

NIF:PVP amorphous solid dispersions prepared by three different methods were studied using SSNMR ^{1}H relaxation time measurements. The 95:5 and 90:10 NIF:PVP dispersions prepared by melt quenching in the typical lab setting were

(32) Aso, Y.; Yoshioka, S. Molecular mobility of nifedipine–PVP and phenobarbital–PVP solid dispersions as measured by ^{13}C-NMR spin-lattice relaxation time. *J. Pharm. Sci.* 2006, *95* (2), 318–325.

(33) Fyfe, C. A. *Solid State NMR for Chemists*, 1st ed.; C. F. C. Press: Guelph, Ontario, Canada, 1983.

(34) Harris, R. K. *Nuclear Magnetic Resonance Spectroscopy: A Physicochemical View*; John Wiley & Sons, Inc.: New York, 1986.

(35) Gao, P. Characterization of three crystalline forms (VIII, XI, and XII) and the amorphous form (V) of delavirdine mesylate using ^{13}C CP/MAS NMR. *Pharm. Res.* 1998, *15* (9), 1425–1433.

(36) Aso, Y.; Yoshioka, S.; Otsuka, T.; Kojima, S. The physical stability of amorphous nifedipine determined by isothermal microcalorimetry. *Chem. Pharm. Bull.* 1995, *43*, 300–3.

(37) Ishida, H.; Wu, T.; Yu, L. Sudden rise of crystal growth rate of nifedipine near T_g without and with polyvinylpyrrolidone. *J. Pharm. Sci.* 2007, *96* (5), 1131–1138.

(38) Marsac, P. J.; Konno, H.; Taylor, L. S. A comparison of the physical stability of amorphous felodipine and nifedipine systems. *Pharm. Res.* 2006, *23*, 2306–2316.

(39) Andrew, E. R.; Bradbury, A.; Eades, R. G. Removal of dipolar broadening of nuclear magnetic resonance spectra of solids by specimen rotation. *Nature* 1959, *183* (4678), 1802–1803.

(40) Pines, A.; Gibby, M. G.; Waugh, J. S. Proton-enhanced NMR of dilute spins in solids. *J. Chem. Phys.* 1973, *59* (2), 569–590.

(41) Dixon, W. T.; Schaefer, J.; Sefcik, M. D.; Stejskal, E. O.; McKay, R. A. Total suppression of sidebands in CPMAS C-13 NMR. *J. Magn. Reson.* 1982, *49* (2), 341–345.

(42) Fung, B. M.; Khitrin, A. K.; Ermolaev, K. An improved broadband decoupling sequence for liquid crystals and solids. *J. Magn. Reson.* 2000, *142* (1), 97–101.

(43) Barich, D. H.; Gorman, E. M.; Zell, M. T.; Munson, E. J. 3-Methylglutaric acid as a ^{13}C solid-state NMR standard. *Solid State Nucl. Magn. Reson.* 2006, *30* (3–4), 125–129.

(44) Bielecki, A.; Burum, D. P. Temperature dependence of ^{207}Pb MAS spectra of solid lead nitrate. An accurate, sensitive thermometer for variable-temperature MAS. *J. Magn. Reson. Ser. A* 1995, *116* (2), 215–220.

(45) Gordon, M.; Taylor, J. S. Ideal copolymers and the second-order transitions of synthetic rubbers. i. non-crystalline copolymers. *J. Appl. Chem.* 1952, *2* (9), 493–500.

(46) Apperley, D. C.; Forster, A. H.; Fournier, R.; Harris, R. K.; Hodgkinson, P.; Lancaster, R. W.; Rades, T. Characterisation of indomethacin and nifedipine using variable-temperature solid-state NMR. *Magn. Reson. Chem.* 2005, *43* (11), 881–892.

(47) Gunn, E.; Guzei, I. A.; Cai, T.; Yu, L. Polymorphism of nifedipine: crystal structure and reversible transition of the metastable β polymorph. *Cryst. Growth Des.* 2012, *12* (4), 2037–2043.

(48) Sperger, D. M.; Fu, S.; Block, L. H.; Munson, E. J. Analysis of composition, molecular weight, and water content variations in sodium alginate using solid-state NMR spectroscopy. *J. Pharm. Sci.* 2011, *100* (8), 3441–3452.

(49) Grooff, D.; De Villiers, M. M.; Liebenberg, W. Thermal methods for evaluating polymorphic transitions in nifedipine. *Thermochim. Acta* 2007, *454* (1), 33–42.

(50) Aso, Y.; Yoshioka, S.; Kojima, S. Explanation of the crystallization rate of amorphous nifedipine and phenobarbital from their molecular mobility as measured by ^{13}C nuclear magnetic resonance relaxation time and the relaxation time obtained from the heating rate dependence of the glass transition temperature. *J. Pharm. Sci.* 2001, *90* (6), 798–806.

(51) Wang, B.; Pikal, M. J. The impact of thermal treatment on the stability of freeze dried amorphous pharmaceuticals: I. dimer formation in sodium ethacrynate. *J. Pharm. Sci.* 2010, *99* (2), 663–682.

(52) Tatton, A. S.; Pham, T. N.; Vogt, F. G.; Iuga, D.; Edwards, A. J.; Brown, S. P. Probing hydrogen bonding in cocrystals and amorphous dispersions using ^{14}N–^{1}H HMQC solid-state NMR. *Mol. Pharmaceutics* 2013, *10* (3), 999–1007.

(53) Karmwar, P.; Graeser, K.; Gordon, K. C.; Strachan, C. J.; Rades, T. Investigation of properties and recrystallisation behaviour of amorphous indomethacin samples prepared by different methods. *Int. J. Pharm.* 2011, *417* (1–2), 94–100.

THE JOURNAL OF PHYSICAL CHEMISTRY B

Article

pubs.acs.org/JPCB

Gauging Colloidal and Thermal Stability in Human IgG1–Sugar Solutions through Diffusivity Measurements

Jonathan Rubin,[†,‡] Aditi Sharma,[†,‡] Lars Linden,[§] Andreas S. Bommarius,[†,‡,∥] and Sven H. Behrens*,[†,‡]

[†]School of Chemical & Biomolecular Engineering, Georgia Institute of Technology, Atlanta, Georgia 30332-0100, United States

[‡]Parker H. Petit Institute of Bioengineering & Biosciences, Georgia Institute of Technology, Atlanta, Georgia 30332-0363, United States

[§]Bayer Healthcare AG, Global Biologics, Wuppertal 42096, Germany

[∥]School of Chemistry & Biochemistry, Georgia Institute of Technology, Atlanta, Georgia 30332-0400, United States

Supporting Information

ABSTRACT: Monoclonal antibodies are the fastest growing class of biotherapeutics. Ensuring their colloidal and conformational stability in liquid dispersions is crucial for maintaining therapeutic efficacy and economic viability. Sugars are often added to increase the colloidal and thermal stability of protein; however, determining which sugar is the most stabilizing requires time and sample-consuming stability tests. Here we show for a human IgG1 that the extent of stabilization by different sugars can be gauged by analyzing the proteins' diffusive virial coefficient k_D. This protein interaction parameter is measured conveniently in a noninvasive, high-throughput manner using dynamic light scattering. It is found to correlate closely with experimental aggregation rate constants at the onset of aggregation and with melting temperatures for antibodies in different sugar solutions. The proposed analysis thus provides a rapid test of the subtle differences between inherently similar sugar–protein interactions; it should greatly facilitate the formulation of protein therapeutics. For the antibody investigated in this study, circular dichroism spectroscopy also yields clues about the *mechanism* by which sugars improve the thermal stability.

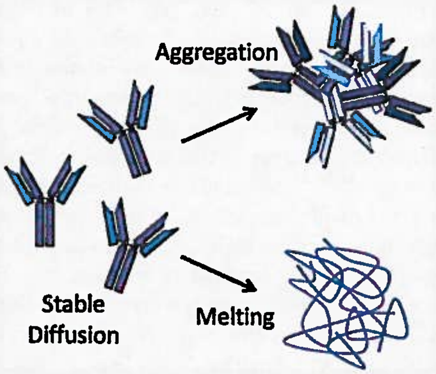

INTRODUCTION

Monoclonal antibodies (mAbs) and antibody derivatives constitute the fastest growing class of biopharmaceuticals.[1] Antibodies are effective in treating a wide range of cancers, autoimmune diseases, inflammation, and potentially even amyloid diseases, such as Alzheimer's.[1−3] As of March 2012, 28 mAbs were actively marketed in the United States and/or the European Union.[4] The combined sale of the 10 top grossing antibodies in 2011 was 52.2 billion USD, and the commercial market for mAbs is expected to continue to grow rapidly.[5] Six of the top ten selling drugs in 2013 are predicted to be mAbs, and nearly 350 antibody-derived therapeutics are currently in development.[5,6]

Although great advances in antibody engineering have brought many successes to market,[7] the field of biologics still struggles with pervasive physical protein instability (for reviews, see refs 2 and 8). Irreversible protein aggregation is a familiar and adverse occurrence during the fermentation, purification, formulation, and storage of biopharmaceuticals, such as antibodies. Aggregates are detrimental because they reduce the therapy's efficacy, are aesthetically undesirable, and, most importantly, may incite an immunogenic response within the patient.[9−11] To avoid these issues, the International Conference on Harmonization and the FDA have regulated that to be salable a biopharmaceutical must have a shelf life greater than 6 months (>12 months is recommended) under manufacturer-prescribed storage conditions [1995 Guideline Q5C (on the "Quality of Biotechnological Products: Stability Testing of Biotechnological/Biological Products) of the International Conference on Harmonisation of Technical Requirements for Registration of Pharmaceuticals for Human Use (ICH); http://www.ich.org/fileadmin/Public_Web_Site/ICH_Products/Guidelines/Quality/Q5C/Step4/Q5C_Guideline.pdf].

To comply with governmental regulations, researchers work to optimize the storage solution environment of mAbs by toggling solution parameters such as the pH, temperature, viscosity, and excipients (salts, sugars, surfactants), to name a few.[12] Sugars are common protein structure stabilizers added to liquid formulations and used to stabilize proteins during lyophilization.[2,8,13−15]

According to the preferential interaction model proposed by Arakawa and Timasheff,[13,16−18] the stabilization of protein solutions by sugar is caused by the preferential hydration of proteins and exclusion of sugar from the protein–water interface. Sugars, having many hydrogen bonding sites, preferentially interact with each other and with the bulk

Received: November 14, 2013
Revised: February 12, 2014
Published: February 20, 2014

ACS Publications © 2014 American Chemical Society

dx.doi.org/10.1021/jp411185d | J. Phys. Chem. B 2014, 118, 2803−2809

5.5, so no additional pH adjustment was necessary. The sugar solutions were sterile filtered through a 0.2 μm PallAcrodisc syringe filter with Supor membrane (Pall Corporation, Port Washington, NY).

Measurements of the Interaction Parameter. Concentration-dependent diffusivity measurements were conducted at 25 °C in the aforementioned buffer (25 mM acetate, 150 mM sodium chloride, pH 5.5). Samples contained a final concentration of 500 mM of a given sugar. Under these conditions the antibody remains stable in its native conformation for over 24 h (i.e., no change in hydrodynamic radius). Prepared sugar solutions were mixed in Corning black-walled 96-well plates with a final protein concentration ranging from 1.9 to 11.9 mg/mL (13.1 to 82.1 μM). Samples were gently mixed then capped by a layer of silicon oil to prevent solvent evaporation. Silicon oil has been shown to have no effect on interaction parameter measurements or aggregation in quiescent systems.[31,46] Samples were investigated by DLS using a Wyatt DynaPro plate reader instrument (Santa Barbara, CA) to measure protein diffusivity and size. The instrument operates in backscatter geometry (158°) using the 830 nm wavelength illumination from a GaAs laser. Each sample well was read 10 consecutive times for 30 s each. The diffusivity readings were averaged and then normalized by the diffusivity at infinite dilution. The interaction parameter k_D was determined as the slope of normalized diffusivity versus protein concentration. An illustrative example of how to calculate k_D is provided in the Supporting Information.

Aggregation Rate Measurements. Aggregation experiments were performed at 5.1 mg/mL antibody at 45 °C. Each sample contained 500 mM of a given sugar. The refractive index and viscosity of each sugar solution was determined as described and tabulated in the Supporting Information. We believe that the antibodies were monomeric and natively folded at the beginning of each experiment, as supported by a low initial polydispersity index (coefficients of variation below 0.1 obtained via cumulant fit of the intensity autocorrelation function in DLS), uniform initial radii in all sugar solutions, and melting temperatures well above 45 °C. Samples were prepared in 96-well plates similar to those used in the diffusivity experiments. The hydrodynamic radius of each sample was tracked continuously over at least 65 h. The change in protein hydrodynamic radius over time was monitored and used to calculate the initial aggregation rate constant k_{11}. A sample calculation is presented in the Supporting Information.

Circular Dichroism Experiments. The antibody's melting temperature was determined using a Jasco J-810 circular dichroism spectrophotometer (Easton, MD) equipped with a Peltier temperature controller. Experiments were conducted at a protein concentration of 120 μg/mL. The sugar concentration (500 mM) was the same as that used in the measurements of the aggregation rate and interaction parameter. A linear 1 °C/min temperature ramp was run from 35 to 95 °C, and the ellipiticity of absorbed light was monitored at a wavelength of 218 nm (sensitive to β-sheets). The data were then normalized, and the apparent melting temperatures were inferred from the loss of 50% of the maximum signal.

RESULTS AND DISCUSSION

Protein Concentration-Dependent Diffusivity. The interaction parameter for the hIgG1 was determined in a variety of saccharide solutions (Figure 1). According to eq 2 larger values of k_D for the same protein indicate a relatively more repulsive, stabilizing protein pair interaction. All of the sugars increased k_D compared to the control, suggesting that they all stabilized the protein to varying degrees. The k_D values for the monosaccharides (glucose, mannitol, sorbitol, and xylitol) were similar despite differences in their molecular weight, oxidation state, and number of hydroxyl groups. From solutions of the disaccharides trehalose and sucrose, a k_D value was obtained that was larger (less negative) than that from the monosaccharide solutions. A summary is presented in Table 1 .

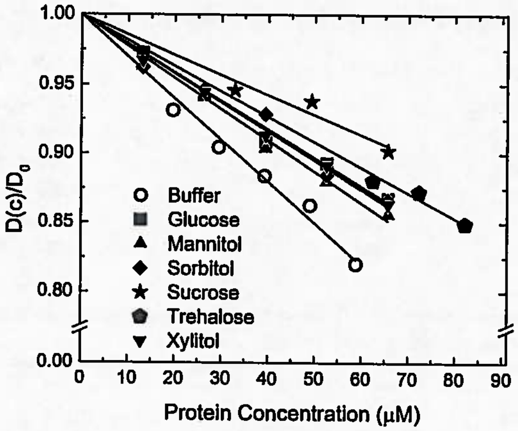

Figure 1. Normalized mutual diffusion coefficient versus protein concentration. k_D is determined from the slope of these curves (eq 1).

Our calculation of k_D assumes that concentration-dependent changes in diffusivity and apparent protein size are a result of protein–protein interactions and not changes in the *actual* size of the protein. While the actual size of some proteins may change with concentration through reversible self-association, unfolding upon dilution, or aggregation, we do not believe this is the case here.[37,38] Self-association should be reflected in the polydispersity. For all of our experiments we consistently observed a polydispersity index of 0.1 (the lowest possible reading for the instrument), so we conclude that our k_D measurements detect the monomeric antibody and are truly measures of protein–protein pair interactions.

Thermally-Induced Aggregation. Aggregation was induced thermally at 45 °C to evaluate how much stabilization the sugars afforded our hIgG1. Little or no aggregation was detected at 35 °C, and aggregation proceeded too rapidly to accurately capture the initial stages at 55 °C (data not shown). A similar need to accelerate aggregation thermally was previously reported in our study of salt-mediated effects on antibody aggregation.[31] Figure 2 shows the initial increase of the protein radius seen by DLS in a representative aggregation experiment from which k_{11} can be calculated, as explained in more detail in the Supporting Information. The k_{11} values for all the sugars tested are presented in Table 1.

At 500 mM all of the sugars tested slowed the rate of aggregation compared to the buffered control. Aggregation in disaccharide solutions was notably slower than aggregation in the presence of the monosaccharides. Monosaccharides slowed aggregation by a factor of 1.5 to 2.3, whereas trehalose slowed aggregation by a factor of 3.6 and sucrose even by a factor of 5.6 (Table 1). The greater stabilization in di- versus monosaccharides can partly be attributed to greater viscosity (see Table S2 in the Supporting Information) and may partly be related to greater exclusion of the sugar from the protein surface.[16,17] Regardless of the mechanism, these stress tests

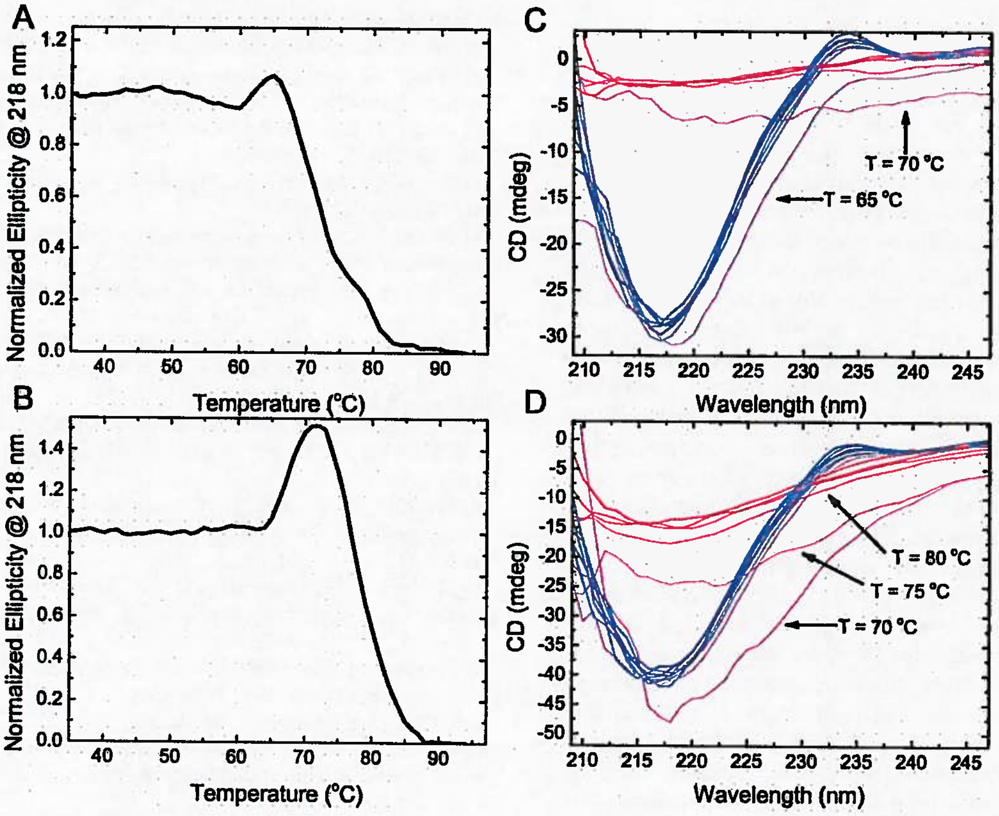

Figure 3. CD melts of aglycosylated hIgG1 in (A) buffer and (B) trehalose read at 218 nm. Full spectra scans every 5 °C are shown for (C) buffer and (D) trehalose. The blue to red color gradient corresponds to traces from 30 to 95 °C, respectively. A melting intermediate can be inferred from the labeled curves in panels C and D and the humps in panels A and B.

toward the denatured spectra, we can clearly see that the traces at 65 and 70 °C in Figure 3C and the traces between 70 and 80 °C in Figure 3D are *not* a mixture of the native and denatured spectra but are distinctly different curves. This distinction is observed over a wider temperature range and produces a signal in trehalose solution (Figure 3D) that is stronger than that in buffer only. Neither panel C nor panel D in Figure 3 contains an isosbestic point, so we may deduce that the hump observed during our melts corresponds to an ephemeral, sugar-stabilized intermediate.

Correlating Stability Metrics. To assess the usefulness of the interaction parameter as a predictor of aggregation propensity and thermostability, we studied the correlation of k_D with k_{11} and with $T_{\mathrm{m,app}}$ (panels A and B of Figures 4, respectively). Both plots revealed strong, roughly linear correlations with a squared correlation coefficient $R^2 \geq 0.91$, suggesting that k_D is indeed a good predictor of antibody stability in saccharide solutions.

For media of different salt composition, we previously reported a strong correlation between k_D and protein stability, with both properties showing general trends familiar from the Hofmeister series[29,31] but with k_D failing to resolve significant variations in the effect of kosmotropic ions on a monoclonal antibody. Unlike salts, which produce electrostatic and ion-specific effects and can either enhance or reduce protein stability,[53] all sugars tend to have the same qualitative effect on proteins. Despite this similarity in saccharide–protein interactions, k_D is seen to resolve subtle quantitative differences in the effect of different sugars and correlate well with aggregation tests and CD melts.

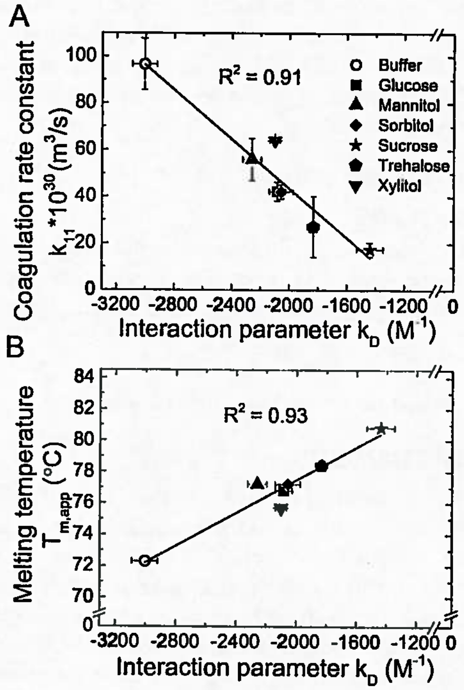

Figure 4. Correlations of the interaction parameter k_D with (A) the coagulation rate constant k_{11} and (B) the apparent melting temperature $T_{\mathrm{m,app}}$. Error estimates for both data sets are given in Table 1.

(25) Lauer, T. M.; Agrawal, N. J.; Chennamsetty, N.; Egodage, K.; Helk, B.; Trout, B. L. Developability Index: A Rapid in Silico Tool for the Screening of Antibody Aggregation Propensity. *J. Pharm. Sci.* 2012, *101*, 102−115.

(26) Auton, M.; Bolen, D. W. Predicting the Energetics of Osmolyte-Induced Protein Folding/Unfolding. *Proc. Natl. Acad. Sci. U.S.A.* 2005, *102*, 15065−15068.

(27) Duddu, S. P.; DalMonte, P. R. Effect of Glass Transition Temperature on the Stability of Lyophilized Formulations Containing a Chimeric Therapeutic Monoclonal Antibody. *Pharm. Res.* 1997, *14*, 591−595.

(28) Polizzi, K. M.; Parikh, M.; Spencer, C. U.; Matsumura, I.; Lee, J. H.; Realff, M. J.; Bommarius, A. S. Pooling for Improved Screening of Combinatorial Libraries for Directed Evolution. *Biotechnol. Prog.* 2006, *22*, 961−967.

(29) Rubin, J.; San Miguel, A.; Bommarius, A. S.; Behrens, S. H. Correlating Aggregation Kinetics and Stationary Diffusion in Protein−Sodium Salt Systems Observed with Dynamic Light Scattering. *J. Phys. Chem. B* 2010, *114*, 4383−4387; and Correction *J. Phys. Chem. B* 2011, *115*, 10778−10778.

(30) Saluja, A.; Fesinmeyer, R. M.; Hogan, S.; Brems, D. N.; Gokarn, Y. R. Diffusion and Sedimentation Interaction Parameters for Measuring the Second Virial Coefficient and Their Utility as Predictors of Protein Aggregation. *Biophys. J.* 2010, *99*, 2657−2665.

(31) Rubin, J.; Linden, L.; Coco, W. M.; Bommarius, A. S.; Behrens, S. H. Salt-induced aggregation of a monoclonal human immunoglobulin G1. *J. Pharm. Sci.* 2013, *102*, 377−386.

(32) Saito, S.; Hasegawa, J.; Kobayashi, N.; Kishi, N.; Uchiyama, S.; Fukui, K. Behavior of Monoclonal Antibodies: Relation Between the Second Virial Coefficient (B-2) at Low Concentrations and Aggregation Propensity and Viscosity at High Concentrations. *Pharm. Res.* 2012, *29*, 397−410.

(33) Behrens, S. H.; Borkovec, M. Influence of the secondary interaction energy minimum on the early stages of colloidal aggregation. *J. Colloid Interface Sci.* 2000, *225*, 460−465.

(34) Lehermayr, C.; Mahler, H. C.; Mader, K.; Fischer, S. Assessment of Net Charge and Protein−Protein Interactions of Different Monoclonal Antibodies. *J. Pharm. Sci.* 2011, *100*, 2551−2562.

(35) Liu, W.; Cellmer, T.; Keerl, D.; Prausnitz, J. M.; Blanch, H. W. Interactions of lysozyme in guanidinium chloride solutions from static and dynamic light-scattering measurements. *Biotechnol. Bioeng.* 2005, *90*, 482−490.

(36) Chari, R.; Jerath, K.; Badkar, A. V.; Kalonia, D. S. Long- and Short-Range Electrostatic Interactions Affect the Rheology of Highly Concentrated Antibody Solutions. *Pharm. Res.* 2009, *26*, 2607−2618.

(37) Connolly, B. D.; Petry, C.; Yadav, S.; Demeule, B.; Ciaccio, N.; Moore, J. M.; Shire, S. J.; Gokarn, Y. R. Weak Interactions Govern the Viscosity of Concentrated Antibody Solutions: High-Throughput Analysis Using the Diffusion Interaction Parameter. *Biophys. J.* 2012, *103*, 69−78.

(38) Yadav, S.; Shire, S. J.; Kalonia, D. S. Viscosity Behavior of High-Concentration Monoclonal Antibody Solutions: Correlation with Interaction Parameter and Electroviscous Effects. *J. Pharm. Sci.* 2012, *101*, 998−1011.

(39) Mirarefi, A. Y.; Zukoski, C. F. Gradient diffusion and protein solubility: Use of dynamic light scattering to localize crystallization conditions. *J. Cryst. Growth* 2004, *265*, 274−283.

(40) James, S.; McManus, J. J. Thermal and Solution Stability of Lysozyme in the Presence of Sucrose, Glucose, and Trehalose. *J. Phys. Chem. B* 2012, *116*, 10182−10188.

(41) Hristodorov, D.; Fischer, R.; Linden, L. With or Without Sugar? (A)glycosylation of Therapeutic Antibodies. *Mol. Biotechnol.* 2012, DOI: 10.1007/s12033-012-9612-x.

(42) Gillespie, R.; Nguyen, T.; Macneil, S.; Jones, L.; Crampton, S.; Vunnum, S. Cation Exchange Surface-Mediated Denaturation of an Aglycosylated Immunoglobulin (IgG1). *J. Chromatogr., A* 2012, *1251*, 101−110.

(43) Kayser, V.; Chennamsetty, N.; Voynov, V.; Forrer, K.; Helk, B.; Trout, B. L. Glycosylation Influences on the Aggregation Propensity of Therapeutic Monoclonal Antibodies. *Biotechnol. J.* 2011, *6*, 38−44.

(44) Sola, R. J.; Griebenow, K. Effects of Glycosylation on the Stability of Protein Pharmaceuticals. *J. Pharm. Sci.* 2009, *98*, 1223−1245.

(45) Hristodorov, D.; Fischer, R.; Joerissen, H.; Muller-Tiemann, B.; Apeler, H.; Linden, L. Generation and Comparative Characterization of Glycosylated and Aglycosylated Human IgG1 Antibodies. *Mol. Biotechnol.* 2012, DOI: 10.1007/s12033-012-9531-x.

(46) Thirumangalathu, R.; Krishnan, S.; Ricci, M. S.; Brems, D. N.; Randolph, T. W.; Carpenter, J. F. Silicone Oil- and Agitation-Induced Aggregation of a Monoclonal Antibody in Aqueous Solution. *J. Pharm. Sci.* 2009, *98*, 3167−3181.

(47) Ionescu, R. M.; Vlasak, J.; Price, C.; Kirchmeier, M. Contribution of Variable Domains to the Stability of Humanized IgG1Monoclonal Antibodies. *J. Pharm. Sci.* 2008, *97*, 1414−1426.

(48) Collins, K. D. Ions from the Hofmeister Series and Osmolytes: Effects on Proteins in Solution and in the Crystallization Process. *Methods* 2004, *34*, 300−311.

(49) Politi, R.; Harries, D. Enthalpically Driven Peptide Stabilization by Protective Osmolytes. *Chem. Commun.* 2010, *46*, 6449−6451.

(50) Hall, M.; Rubin, J.; Behrens, S. H.; Bommarius, A. S. The Cellulose-Binding Domain of Cellobiohydrolase Cel7A from Trichoderma Reesei Is Also a Thermostabilizing Domain. *J. Biotechnol.* 2011, *155*, 370−376.

(51) Hud, N. V.; Smith, F. W.; Anet, F. A. L.; Feigon, J. The Selectivity for K$^+$ Versus Na$^+$ in DNA Quadruplexes Is Dominated by Relative Free Energies of Hydration: A Thermodynamic Analysis by ^{1}H NMR. *Biochemistry* 1996, *35*, 15383−15390.

(52) Lannan, F. M.; Mamajanov, I.; Hud, N. V. Human Telomere Sequence DNA in Water-Free and High-Viscosity Solvents: G-Quadruplex Folding Governed by Kramers Rate Theory. *J. Am. Chem. Soc.* 2012, *134*, 15324−15330.

(53) Broering, J. M.; Bommarius, A. S. Evaluation of Hofmeister Effects on the Kinetic Stability of Proteins. *J. Phys. Chem. B* 2005, *109*, 20612−20619.

Salt-Induced Aggregation of a Monoclonal Human Immunoglobulin G1

JONATHAN RUBIN,[1,2] LARS LINDEN,[3] WAYNE M. COCO,[4] ANDREAS S. BOMMARIUS,[1,2,5] SVEN H. BEHRENS[1]

[1]School of Chemical and Biomolecular Engineering, Georgia Institute of Technology, Atlanta, Georgia 30332-0100

[2]Parker H. Petit Institute of Bioengineering and Bioscience, Georgia Institute of Technology, Atlanta, Georgia 30332-0363

[3]Bayer Healthcare AG, Global Biologics, Wuppertal 42096, Germany

[4]Bayer Healthcare AG, Global Biologics, Cologne 50829, Germany

[5]School of Chemistry and Biochemistry, Georgia Institute of Technology, Atlanta, Georgia 30332-0400

Received 19 June 2012; revised 13 October 2012; accepted 18 October 2012

Published online 12 November 2012 in Wiley Online Library (wileyonlinelibrary.com). DOI 10.1002/jps.23363

ABSTRACT: Physical stability is critical for any therapeutic protein's efficacy and economic viability. No reliable theory exists to predict stability *de novo,* and modeling aggregation is challenging as this phenomenon can involve orientation effects, unfolding, and the rearrangement of noncovalent bonds inter- and intramolecularly in a complex sequence of poorly understood events. Despite this complexity, the simple observation of protein concentration-dependent diffusivity in stable, low ionic-strength solutions can provide valuable information about a protein's propensity to aggregate at higher salt concentrations and over longer times. We recently verified this notion using two model proteins, and others have shown that this strategy may be applicable to antibodies as well. Here, we expand our previous study to a monoclonal human immunoglobulin G1 antibody and discuss both merits and limitations of stability assessments based on the diffusional virial coefficient k_D. We find this parameter to be a good predictor of relative protein stability in solutions of different chaotropic salts, and a telling heuristic for the effect of kosmotropes. Both temperature and glycosylation are seen to have a strong influence on k_D, and we examine how these factors affect stability assessments. Protein unfolding is monitored with a fluorescence assay to assist in interpreting the observed aggregation rates. © 2012 Wiley Periodicals, Inc. and the American Pharmacists Association J Pharm Sci 102:377–386, 2013

Keywords: protein aggregation; protein folding/refolding; light scattering (dynamic); Hofmeister; interaction parameter; ANS fluorescence; protein formulation; monoclonal antibody; stability; kinetics

INTRODUCTION

Antibodies represent the fastest growing class of human therapeutics.[1,2] They treat a wide range of conditions, including transplant rejection, non-Hodgkin's lymphoma, multiple sclerosis, and a variety of cancers.[1] As of March 2012, 34 monoclonal antibodies (mAbs) were approved for sale in the United States and European Union, 28 of which are actively marketed and nine of the 28 have achieved blockbuster status.[3,4]

Irreversible protein aggregation is a common and undesirable occurrence in many stages of biopharmaceutical manufacturing including fermentation, purification, formulation, and storage. Aggregates are detrimental because they reduce the efficacy of the treatment,[5] and may elicit an immune response.[6] Because of these concerns, the International Conference on Harmonisation has regulated that a biological pharmaceutical must have a shelf-life greater than 6 months (>12 months is recommended) under its prescribed storage conditions to be salable [Q5C ICH § 4.3 (1995)].

Abbreviations used: mAb, monoclonal antibody; hIgG1, human immunoglobulin G1; ANS, 8-anilino-1-naphthalenesulfonic acid; DLS, dynamic light scattering.

Additional Supporting Information may be found in the online version of this article. Supporting Information

Correspondence to: Sven H. Behrens (Telephone: +404-894-3166; Fax: +404-894-2866; E-mail: sbehrens@gatech.edu)

Journal of Pharmaceutical Sciences, Vol. 102, 377–386 (2013)

© 2012 Wiley Periodicals, Inc. and the American Pharmacists Association

pharmaceutically relevant monoclonal human immunoglobulin G1 (hIgG1) antibody and its aglycosylated counterpart. Although the relative stability of these antibodies in different chaotropic solutions is accurately reflected in measured values of k_D, the influence of different kosmotropic media on protein stability cannot be resolved in the same way. We further show that caution is warranted when interpreting variations in the interaction parameter caused by (de)glycosylation or temperature changes. Lastly, we study the antibodies' folding state during salt-induced aggregation using the hydrophobic residue binding dye 8-anilino-1-naphthalenesulfonic acid (ANS) and relate the findings to the observed aggregate growth.

MATERIALS

Antibodies

A pair of hIgG1 mAbs (molecular weight = 145 kDa) was used as the basis for this study. The two proteins were a glycosylated and an aglycosylated version of a protein with the same amino acid sequence and a pI of 8.23. The aglycosylated version was generated by introducing the mutation N297A into the heavy chain as described previously.[26] The purified proteins were provided by Bayer Pharma AG (Berlin, Germany) in 25 mM acetate buffer (pH 5.5) and 150 mM sodium chloride. The formulation was purified via buffer exchange cross-flow and size-exclusion chromatography, then sterile filtered and frozen in liquid nitrogen. The glycosylated IgG1 was present at 362 μM (52.3 mg/mL) and the aglycosylated antibody was provided at 80 μM (11.49 mg/mL). The concentration of the antibodies was determined before experimentation using a molar extinction coefficient of 235,480 $(\mathrm{M\ cm})^{-1}$.

Salt Buffer Preparation

All salts used were of >99% purity, American Chemical Society reagent grade. Salt solutions were prepared in the isotonic acetate buffer described above. Solutions contained one of the following: sodium citrate (J.T. Baker, Phillipsburg, New Jersey)/citric acid (Sigma–Aldrich, St. Louis, Missouri), sodium sulfate anhydrous (Sigma–Aldrich), sodium acetate (Sigma–Aldrich)/acetic acid (purity 96%, Honeywell Riedel-de Haen, Seelze, Germany), sodium formate (Aldrich), sodium fluoride (BDH Merck Ltd, Poole Dorset, United Kingdom), sodium chloride (BDH), sodium bromide (Sigma–Aldrich), sodium nitrate (Sigma–Aldrich), sodium iodide (EMD Merck KGaA, Darmstadt, Germany), and sodium thiocyanate (Sigma–Aldrich). After dissolving salt in the buffer described above, the pH was readjusted, if necessary, to 5.5 ± 0.05 using either sodium hydroxide or the appropriate acid (i.e., sulfuric acid for a sulfate solution). The salt solution was then filtered through a hydrophilic polyethersulfone membrane with 0.2 μm pores (Pall Acrodisc® syringe filter with Supor® membrane, Pall Corporation, Port Washington, New York).

METHODS

Interaction Parameter Determination

Diffusivity measurements were carried out at 25°C, 35°C, and 45°C, pH 5.5, and ionic strength 0.225 M (175 mM arising from the ubiquitous background buffer described above and 50 mM from the salt being tested). In these conditions, the protein remains stable in its native conformation (T_m is shown in Table 2 and Fig. S8, Supplementary Information).[27]

Prepared salt solutions and protein solutions were mixed in a Corning black-walled 96-well plate with final protein concentrations between 12 and 180 μM (1.4 and 26 mg/mL). The samples were stirred very gently to provide adequate mixing while avoiding shear-induced aggregation. They were then capped by a layer of silicon oil to prevent solvent evaporation and investigated by DLS using a Wyatt DynaPro plate reader, which operates in a backscattering geometry (158°). Data obtained using paraffin oil to cap wells are presented in Supplementary Information. The silicon oil had no effect on the readings as it is insoluble in water.[28] Every well was read 10 consecutive times for 20 s each. Diffusivity readings obtained from DLS measurements at the same protein concentration were averaged and normalized by the diffusivity found in the most dilute solutions. Then, the interaction parameter k_D was determined from the slope of the normalized diffusivity as a function of protein concentration. An illustrative example of calculating k_D is provided in the Supplementary Information.

Aggregation Rate Experiments

Aggregation rate experiments were performed at 35°C and 45°C. Samples were prepared in 96-well plates similarly to the diffusivity experiments; however, in these experiments, a wide range of salt molarities was investigated. The hydrodynamic radius of each sample was tracked over a minimum of 12 h. The change in particle hydrodynamic radius over time was monitored and used to calculate the initial aggregation rate k_{11}.[19]

ANS Binding

A solution of ANS(Sigma-Aldrich) was prepared daily in the acetate buffer described above. Samples were prepared in duplicates in a black-walled 96-well plate. All experiments were conducted at 35°C, the protein concentration was 3.5 μM (0.4 mg/mL, for both proteins), and 60 μM ANS was present in each well in addition to the salt in question. For every salt, a pair of wells without protein, but containing the same

DOI 10.1002/jps

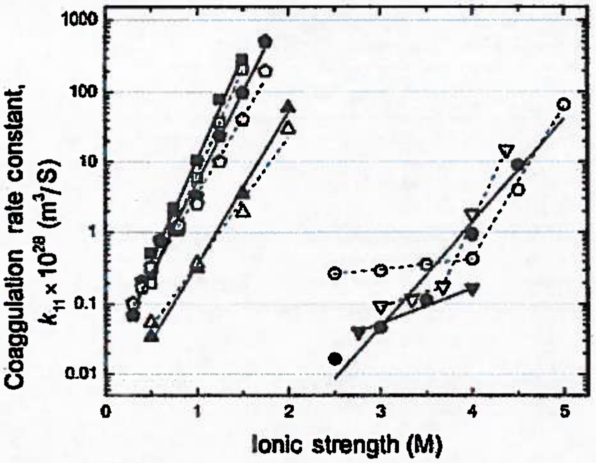

Figure 2. Coagulation rate constants as function of ionic strength at 35°C for thiocyanate (■), iodide (▲), perchlorate (pentagon), bromide (●), and chloride (▼). Closed icons are for the glycosylated antibody and open icons are for aglycosylated. Fitting error bars (not shown) generated by Excel Linest were comparable in size to the data point markers or smaller.

in Figure 2. Accelerating aggregation by means of increasing temperature is a common method for fast assessments of long-term stability.[7,31] Aggregation experiments at 45°C were also conducted and are available in the Supplementary Information.

In the 25 mM acetate background buffer at 35°C, the glycosylated protein did not aggregate over 12 h; however, the aglycosylated antibody aggregated over 12 h at a rate of $k_{11} = 8.1 \times 10^{-30}$ m³/s. At 45°C, the rate constants of aggregation for the glycosylated and aglycosylated mAbs were $k_{11} = 2 \times 10^{-29}$ and 5.5×10^{-29} m³/s, respectively.

Figure 2 shows the aggregation rate constant k_{11} of both antibodies in solutions of different chaotropes. As with the interaction parameter, we see a Hofmeister trend where k_{11} at constant ionic strength generally increased with increasing chaotropicity. Thiocyanate caused aggregation at the lowest ionic strength (~1 M), and weaker chaotropes, such as bromide and chloride, required much higher salt concentrations (~4 M) to destabilize the protein. Surprisingly, glycosylation did not systematically affect the aggregation rates (Fig. 2): in the presence of very strong chaotropes (thiocyanate, iodide, and perchlorate), no significant differences between the aggregation rates of glycosylated and aglycosylated antibodies are observed at all, whereas for the weak chaotrope, bromide glycosylation does appear to provide some stabilization. This effect, however, is significant only at ionic strengths (below 4 M NaBr) where aggregation is already slow ($<10^{-28}$ m³/s).

Aggregation experiments with kosmotropes are summarized in Figure 3. Unlike experiments with chaotropes, they did not show a simple increase in k_{11} with increasing kosmotropicity. Instead, three regimes were apparent: (1) no observable aggregation, (2) slow aggregation, and (3) rapid aggregation with almost instantaneous precipitation. Coagulation rate constants in regime (2) (not shown) were all below 10^{-28} m³/s and showed no systematic trend. Regime (3) aggregated too fast to measure. Interestingly, for acetate and formate, moderate salt concentrations did not induce any aggregation [regime (1)]. With acetate, precipitation or gelation of either antibody [i.e., regime (3)] could not be achieved in the entire ionic strength range (up to 3.75 M).

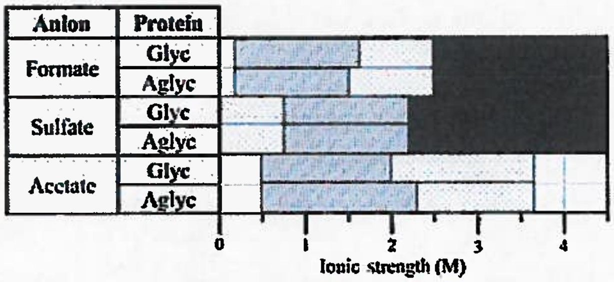

Figure 3. Molarities of a given kosmotropes to induce no aggregation (dotted), slow aggregation (shaded grey, $k_{11} < 1 \times 10^{-28}$ m³/s) or instantaneous aggregation (black) for glycosylated ("Glyc") and aglycosylated ("Aglyc") antibodies.

To aid stability comparisons in the chaotropic solutions, we adopt as a metric for the stability against salt-induced aggregation the ionic strength I_s required to trigger aggregation at an initial rate of $k_{11} = 10^{-28}$ m³/s. This same reference value of k_{11} was previously used in our study of lysozyme and BSA.[32] The results for I_s, along with the values of the interaction parameter k_D, are reported in Table 2.

Correlating k_D and I_s

Figure 4 presents the correlation between the ionic strength I_s inducing aggregation at a rate of $k_{11} = 10^{-28}$ m³/s and the protein–protein interaction parameter k_D. Only data for the chaotropic counterions are plotted, for reasons discussed earlier.

A strong correlation is found for the glycosylated protein ($R^2 = 0.99$) and a fair correlation for the aglycosylated protein ($R^2 = 0.82$). The lower R^2 for the aglycosylated protein is likely derived from the greater uncertainty in k_D (see Table 2).

Unfolding and Aggregation

In chaotropic solutions, increasing salt concentrations always led to faster aggregation (Fig. 2); in kosmotropic solutions (Fig. 3), however, the same was not always true. In acetate and formate, both antibodies aggregated slowly at low salt concentrations, but at moderate concentrations no aggregation was observed. We suspected that the antibodies' folding state had a strong bearing on this behavior and

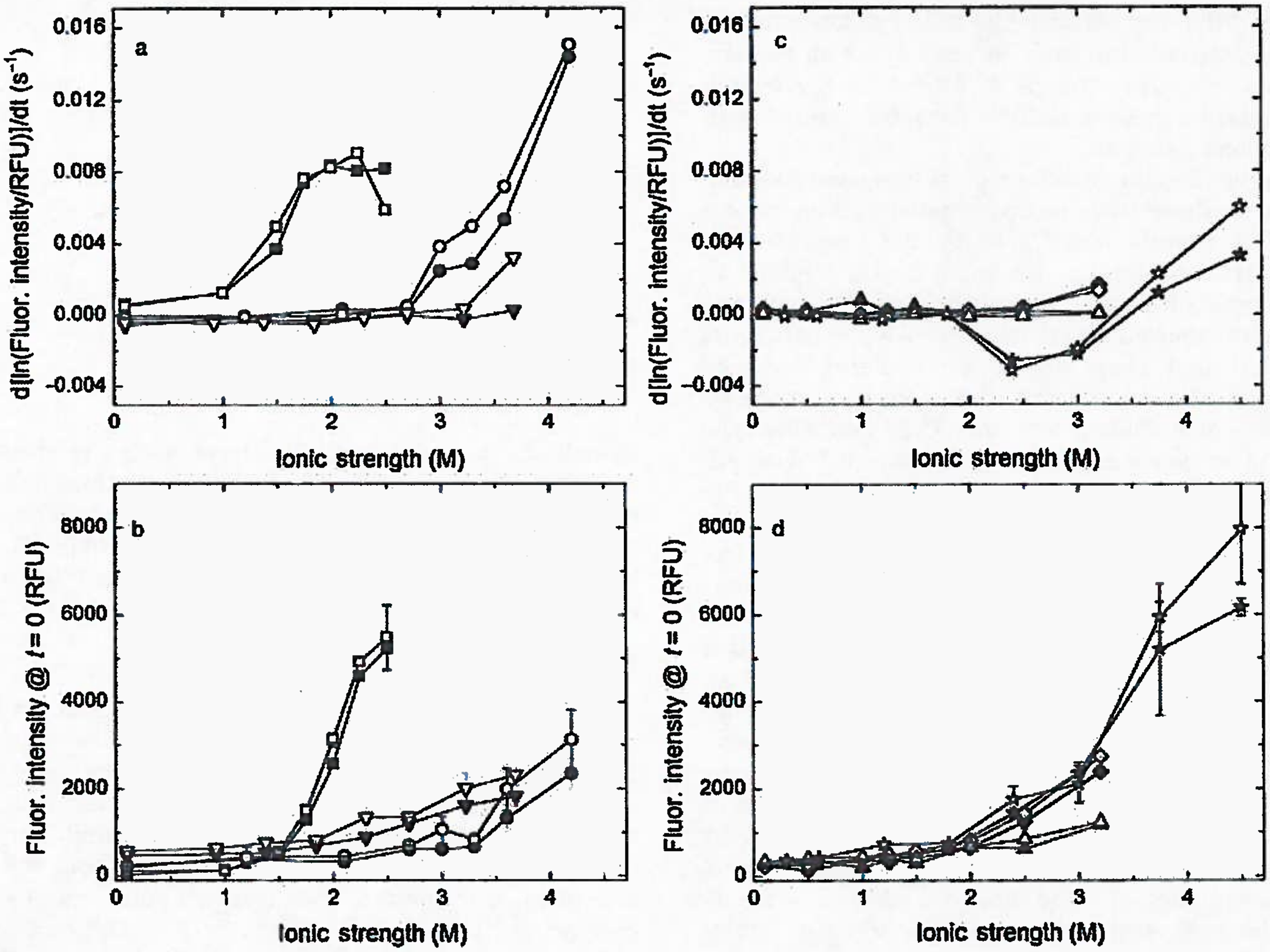

Figure 5. ANS binding rates for chaotropes (a) and kosmotropes (c); fitting error bars generated by Excel Linest were on the order of the data markers or smaller. Initial ANS binding is displayed for chaotropes (b) and kosmotropes (d); the error shown corresponds to one standard deviation. Chaotropes (a and b) include thiocyanate (■), bromide (●), and chloride (▼). Kosmotropes (c and d) include formate (◆), acetate (▲), and sulfate (hexagon). Closed icons are for the glycosylated and open icons are for aglycosylated antibody.

sulfate solutions. Acetate and formate solutions were generally stable, therefore, no significant difference in stability was observed due to glycosylation.

From these experiments, we find that substantial aggregation and substantial unfolding always go hand in hand. In the case of formate and acetate, however, slow aggregation is found without significant unfolding (below 1.5 M) and slight unfolding without aggregation (at 2.0–2.5 M formate or above 2.5 M acetate).

DISCUSSION

Manifestation of Hofmeister Effects

In all three sets of experiments (interaction parameter, salt-induced aggregation, and unfolding state experiments), a common trend along the lines of the Hofmeister series was observed. Chaotropes introduced instability, the extent of which depended on the chaotropicity of the anion. Kosmotropes stabilized the antibodies; however, the effect of different kosmotropes did not vary greatly. This Hofmeister trend, where chaotropes vary significantly, but kosmotropes do not, has been observed previously in the case of lysozyme's propensity to aggregate[19] and the kinetic destabilization of horse liver alcohol dehydrogenase, α-chymotrypsin, and monomeric Red Fluorescent Protein activity.[34]

This phenomenon can be rationalized by chaotropes' natural tendency to accumulate at the protein surface, whereas kosmotropes act around the protein. Weakly hydrated chaotropes adsorb onto hydrophobic surfaces or interfaces (such as air–water interfaces or hydrocarbons on proteins).[35,36] The more chaotropic the ion, the stronger this effect and the more tightly the ion will bind to a protein,[37] and in turn the greater the observed effect. The

CONCLUSIONS

Previously, the "protein interaction parameter" k_D accessible by DLS was shown to be a fast and reliable predictor for the ion-specific destabilization of globular model proteins by different sodium salts.[19] This work extends the study to the ion-induced destabilization of a monoclonal hIgG1 antibody, with regard to both the aggregation and folding state of the antibody, and additionally examines the influence of temperature and glycosylation. In agreement with our previous work, this work shows that a significantly lower k_D for one electrolyte composition over another at the same ionic strength is suggestive of lower relative stability. The interaction parameter k_D was best determined at room temperature (25°C) as higher temperatures obscured Hofmeister effects. This interaction parameter was found to be a good predictor of ion-specific aggregation trends in the chaotropic regime and a telling heuristic in kosmotropic solutions. We found k_D to be very sensitive to glycosylation. Despite the strong influence of both temperature and glycosylation on k_D, these effects do not correlate with stability.

Accelerated tests of protein stability are a critical part of bringing a drug to market quickly. We have shown that, when interpreted with caution, the interaction parameter for stable protein solutions can offer valuable clues about the relative stability in much more saline, aggregating conditions. The required diffusivity data are accessible fast and without sample degradation by a noninvasive, high-throughput technique, making the analysis of interaction parameters a highly promising tool for faster and more directed screening of therapeutic proteins.

ACKNOWLEDGMENTS

Funding for this project was provided by the National Science Foundation IUCRC Center for Pharmaceutical Development (CPD) (grant 0969003) and the GAANN fellowship through the US Department of Education. We thank Grant Hendrickson and Dr. Andrew Lyon of Georgia Tech for use of their plate reader DLS and Dr. Irena Mamajanov and Dr. Nicolas Hud of Georgia Tech for help with use of the CD instrument. We are grateful to all members of Cell and Protein Sciences, Bayer Pharma AG, who contributed to this manuscript. J.R. would also like to thank J.T. Park, R.M. Clairmont, and D.R. Noga for fruitful discussion and advice.

REFERENCES

1. Carter PJ. 2006. Potent antibody therapeutics by design. Nat Rev Immunol 6(5):343–357.
2. Daugherty AL, Mrsny RJ. 2006. Formulation and delivery issues for monoclonal antibody therapeutics. Adv Drug Deliver Rev 58(5–6):686–706.
3. Elvin JG, Couston RG, van der Walle CF. 2011. Therapeutic antibodies: Market considerations, disease targets and bioprocessing. Int J Pharm. DOI:10.1016/j.ijpharm.2011.12.039 [Epub ahead of print.]
4. Reichert JM. 2012. Marketed therapeutic antibodies compendium. MA 4(3):413–415.
5. Schellekens H. 2002. Immunogenicity of therapeutic proteins: Clinical implications and future prospects. Clin Ther 24(11):1720–1740.
6. Rosenberg AS. 2006. Effects of protein aggregates: An immunologic perspective. AAPS J 8(3):E501–E507.
7. Allen LV, Popovich NG, Ansel HC. 2010. Ansel's pharmaceutical dosage forms and drug delivery systems. 9th ed. Philadelphia, Pennsylvania: Lippincott Williams & Wilkins.
8. Chi EY, Krishnan S, Randolph TW, Carpenter JF. 2003. Physical stability of proteins in aqueous solution: Mechanism and driving forces in nonnative protein aggregation. Pharm Res 20(9):1325–1336.
9. Baldwin RL. 1996. How Hofmeister ion interactions affect protein stability. Biophys J 71(4):2056–2063.
10. Lauer TM, Agrawal NJ, Chennamsetty N, Egodage K, Helk B, Trout BL. 2012. Developability index: A rapid in silico tool for the screening of antibody aggregation propensity. J Pharm Sci 101(1):102–115.
11. Liu W, Cellmer T, Keerl D, Prausnitz JM, Blanch HW. 2005. Interactions of lysozyme in guanidinium chloride solutions from static and dynamic light-scattering measurements. Biotechnol Bioeng 90(4):482–490.
12. Chi EY, Krishnan S, Kendrick BS, Chang BS, Carpenter JF, Randolph TW. 2003. Roles of conformational stability and colloidal stability in the aggregation of recombinant human granulocyte colony-stimulating factor. Protein Sci 12(5):903–913.
13. Alford JR, Kendrick BS, Carpenter JF, Randolph TW. 2008. Measurement of the second osmotic virial coefficient for protein solutions exhibiting monomer–dimer equilibrium. Anal Biochem 377(2):128–133.
14. Attri AK, Minton AP. 2005. New methods for measuring macromolecular interactions in solution via static light scattering: basic methodolog, and application to nonassociating and self-associating proteins. Anal Biochem 337(1):103–110.
15. Tessier PM, Lenhoff AM, Sandler SI. 2002. Rapid measurement of protein osmotic second virial coefficients by self-interaction chromatography. Biophys J 82(3):1620–1631.
16. Saluja A, Fesinmeyer RM, Hogan S, Brems DN, Gokarn YR. 2010. Diffusion and sedimentation interaction parameters for measuring the second virial coefficient and their utility as predictors of protein aggregation. Biophys J 99(8):2657–2665.
17. Lehermayr C, Mahler HC, Mader K, Fischer S. 2011. Assessment of net charge and protein–protein interactions of different monoclonal antibodies. J Pharm Sci 100(7):2551–2562.
18. Bommarius AS, Broering JM, Chaparro-Riggers JF, Polizzi KM. 2006. High-throughput screening for enhanced protein stability. Curr Opin Biotech 17(6):606–610.
19. Rubin J, San Miguel A, Bommarius AS, Behrens SH. 2010. Correlating aggregation kinetics and stationary diffusion in protein-sodium salt systems observed with dynamic light scattering. J Phys Chem B 114(12):4383–4387.
20. Saito S, Hasegawa J, Kobayashi N, Kishi N, Uchiyama S, Fukui K. 2012. Behavior of monoclonal antibodies: Relation between the second virial coefficient (B(2)) at low concentrations and aggregation propensity and viscosity at high concentrations. Pharmaceut Res 29(2):397–410.
21. Behrens SH, Borkovec M. 2000. Influence of the secondary interaction energy minimum on the early stages of colloidal aggregation. J Colloid Interface Sci 225(2):460–465.
22. Connolly BD, Petry C, Yadav S, Demeule B, Ciaccio N, Moore JMR, Shire SJ, Gokarn YR. 2012. Weak interactions govern the viscosity of concentrated antibody solutions:

BIOCHEMISTRY
including biophysical chemistry & molecular biology

Article

pubs.acs.org/biochemistry

Novel Protease Inhibitors via Computational Redesign of Subtilisin BPN′ Propeptide

Ashley B. Daugherty, Pravin Muthu, and Stefan Lutz*

Department of Chemistry, Emory University, 1515 Dickey Drive, Atlanta, Georgia 30322, United States

Supporting Information

ABSTRACT: The propeptide domain of subtilisin BPN′ functions as a molecular chaperone for its cognate protease yet quickly assumes a predominantly unfolded structure following cleavage by the mature protease. In contrast, structural stabilization of the propeptide domain has been proposed to competitively inhibit protease self-cleavage, suggesting the possibility for the generation of novel proteinaceous subtilisin inhibitors. Using a Rosetta fixed backbone design, we have redesigned the subtilisin BPN′ propeptide structure to generate synthetic peptide sequences with increased and tunable structural stability. Molecular dynamics simulations provide supporting evidence that the artificial sequences retain structure without its protease cognate unlike the inherently disordered wild-type propeptide. Experimental evaluation of two designer domains by spectroscopic methods verified their structural integrity. Furthermore, the novel propeptide domains were shown to possess significantly enhanced thermostability. Nevertheless, their modest functional performance as protease inhibitors raises doubt that propeptide stability alone is sufficient for effective inhibitor design.

Subtilisins belong to the class of nonspecific serine proteases in the subtilase family. Originally isolated from various *Bacillus* species in soil, these enzymes are highly efficient and promiscuous hydrolases with significance in a variety of commercial applications and organic synthetic chemistry.[1−4] To prevent autoproteolysis of the enzyme, the addition of reversible protease inhibitors such as borates and boronic acid derivatives has been a standard procedure.[5−7] Nevertheless, these small-molecule inhibitors present a significant environmental problem. Attractive and sustainable alternatives to the existing inhibitors are proteinaceous subtilisin inhibitors derived from the protease's own N-terminal propeptide sequence.[4,8] Normally, these propeptide sequences play a critical role as a chaperone in the maturation process of native proteases, assisting the latter in folding efficiently into its correct tertiary structure.[9−11] Upon the successful completion of folding, the propeptide C-terminal region is positioned in the substrate-binding cleft of the mature enzyme and is consequently hydrolyzed. Self-cleavage triggers unfolding and release of the pro-segment, followed by further degradation by its cognate protease.[12−14]

Beyond the function of the propeptide as an intramolecular chaperone in protease maturation, previous studies have indicated that the bound pro-sequence can also temporarily inhibit proteolytic activity.[15,16] A key component to sustaining inhibitory function is retention of the propeptide tertiary structure. It has been reasoned that these naturally effective but short-lived inhibitors can work for extended periods of time if the structural integrity of the propeptide is preserved through enhanced protein stability, which reduces the level of pro-sequence unfolding and susceptibility to proteolysis.[12,17,18] Such an argument is independently supported by structure analysis of natural protease inhibitors such as proteinase A inhibitor 1 (POIA1) from *Pleurotus ostreatus* [Protein Data Bank (PDB) entries 1V5I and 1ITP] and yeast proteinase B inhibitor 2 that have been found to exhibit high degrees of structural similarity with the folded propeptide.[15,19−21]

The hypothesis has also been explored experimentally by a series of protein engineering studies involving subtilisin BPN′ from *Bacillus amyloliquefaciens* and its pro-sequence. Rational protein design and directed evolution strategies led to the introduction of a disulfide bond into the propeptide sequence by Bryan and co-workers and translated into a dramatic stabilization of the propeptide.[22−25] Separately, Kojima et al. reported a number of propeptide BPN′ mutants with improved packing of their hydrophobic core that exhibited increased stability and improved inhibitory function.[17,18,26] However, the former design was not tested for inhibitory function, while the data for the latter variants proved to be difficult to reproduce.

In recent years, advances in computational algorithms for in silico protein design have offered a promising new approach for improving protein stability.[27,28] In silico methods have an advantage over directed evolution strategies with regard to speed and ability for more comprehensively sampling the vastness of sequence space. An extended study of nine globular proteins by Baker and co-workers demonstrated that their Rosetta design algorithm is an effective tool for identifying

Received: June 20, 2012
Revised: September 20, 2012
Published: September 25, 2012

ACS Publications © 2012 American Chemical Society

dx.doi.org/10.1021/bi300832v | *Biochemistry* 2012, 51, 8247−8255

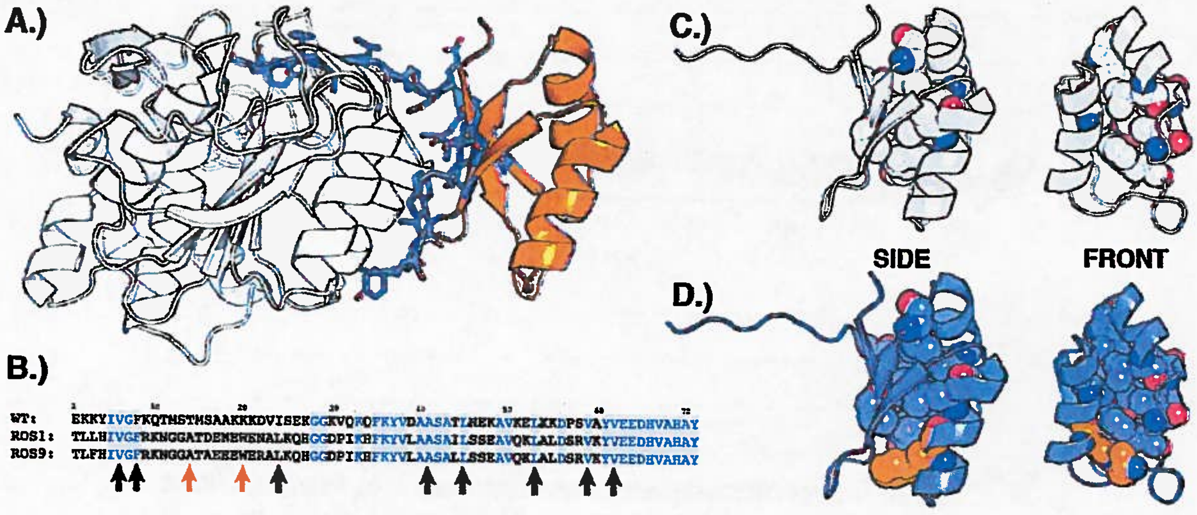
A.)
B.)
C.)
SIDE
FRONT
D.)
10
20
30
40
50
60
72
WT: EKKYIVGFKQTMSTMSAAKKKDVISEKGGKVQKQFKYVDAASATLNEKAVKELKKDPSVAYVEEDHVAHAY
ROS1: TLLHIVGFRKNGGATDENEWENALKQHGGDPIKHFKYVLAASAILSSEAVQKLALDSRVKYVEEDHVAHAY
ROS3: TLFHIVGFRKNGGATAEEEWERALKQHGGDPIKHFKYVLAASALLSSEAVQKLALDSRVKYVEEDHVAHAY

Figure 1. Protease propeptide redesign. (A) Structure of wild-type subtilisin BPN′ with bound propeptide (PDB entry 1SPB).[9] The propeptide is colored orange with residues at the propeptide–protease interface shown as purple sticks. (B) Sequence alignment of the native propeptide (WT) with Rosetta designs ROS1 and ROS3. Conserved residues are highlighted in gray, while residues of the hydrophobic core structure are marked with arrows. Positions 14 and 20 (orange arrows) represent the residues involved in the predicted core expansion. (C) Side and front views of the native propeptide with hydrophobic core residues shown in space-filling mode. (D) Computational model of ROS1 with the hydrophobic core expanded by T14A and K20W mutations (orange).

and loaded onto a HiTrap SP FF column, preequilibrated with buffer B [50 mM HEPES (pH 8) and 50 mM NaCl for WT and 50 mM sodium phosphate (pH 6) and 50 mM NaCl for ROS1, ROS3, and REF]. The column was washed with 7 column volumes (CV) of the corresponding buffer B. A linear gradient from 0 to 50% buffer C (buffer B with 1 M NaCl) over 25 CV was applied. Product fractions were combined and concentrated to ~1 mL using a Millipore filter unit (molecular mass cutoff of 3 kDa). In a final polishing step, propeptides were purified by size exclusion chromatography {Superdex 200, 10/300 GL column, equilibrated with buffer D [50 mM Tris-HCl (pH 8) and 300 mM NaCl]; flow rate of 0.5 mL/min}. Elution of the propeptide was monitored by UV detection at 280 nm, and product fractions were combined and analyzed by sodium dodecyl sulfate–polyacrylamide gel electrophoresis (SDS–PAGE). Propeptide samples were flash-frozen in liquid nitrogen and stored at −80 °C.

Circular Dichroism Spectroscopy. The experiments were performed using a Jasco J-810 spectropolarimeter equipped with a Peltier unit for temperature control. The path length of the cuvette used was 1 mm, with the protein concentration ranging from 25 to 40 μM as determined by the absorbance at 280 nm. All samples were prepared in 50 mM potassium phosphate buffer (pH 7–8 depending on the pI). Spectra were collected in the far-UV wavelength range at 25 °C using a scan rate of 20 nm/min, a response time of 2 s, and a bandwidth of 2 nm. The spectrum reported represents an average of three accumulation scans. For thermal denaturation experiments, the change in ellipticity at 222 nm was monitored from 4 to 80 °C with a temperature gradient of 1.0 °C/min.

Intrinsic Tryptophan Fluorescence. All measurements were taken on a FluoroMax-3 spectrophotometer (Horbia Jobin Yvon, Edison, NJ), equipped with a thermostated cell holder and a NESLAB RTE7 water bath (Thermo Electron Corp., Waltham, MA). Purified protein samples of ROS1 and ROS3 (70–140 μM) were prepared in 50 mM potassium phosphate buffer (pH 8). As a control, tryptophan (50 μM) was used in the same buffer. Samples were excited at 295 ± 0.5 nm, and their emission spectra were measured with 1 nm bandwidth resolution at wavelengths between 300 and 400 nm. Sample scans were taken in 5 °C increments from 20 to 75 °C with a 3 min sample equilibration time. All spectral data were analyzed in Origin7 to determine the maximal peak intensity and emission wavelength.

Protease Inhibition. Protease inhibition was monitored via hydrolysis of AAFP (*N*-succinyl-L-Ala-L-Ala-L-Pro-L-Phe *p*-nitroanilide) by selected proteases in the presence of various amounts of propeptide.[37] Assays were conducted with protease concentrations remaining consistent for each data set (1.8 nM for Savinase, 0.38 nM for BLAP, and 0.56 nM for Carlsberg) and 1–50-fold molar ratios of propeptide at 25 °C. Briefly, the propeptide was mixed with protease and preincubated for 0 or 20 min, followed by addition to 0.111 mM AAFP in reaction buffer [0.1 M Tris-HCl (pH 8.6) and 0.1% Brij35] and a total reaction volume of 1 mL. Upon addition of enzyme mix, substrate conversion was monitored spectrophotometrically via a change in absorbance at 410 nm over time. Substrate hydrolysis for each propeptide:protease ratio was measured in triplicate.

■ RESULTS AND DISCUSSION

Computational Propeptide Redesign. The Rosetta Molecular Modeling program (version 3.1) was used for redesigning the propeptide domain of subtilisin BPN′.[31] An initial search of SCOP [Structural Classification of Proteins (http://scop.mrc-lmb.cam.ac.uk/scop/)] found four crystal structures for propeptides in the subtilase family [PDB entries 1SPB (subtilisin BPN′ from *B. amyloliquefaciens*),[9] 1SCJ (subtilisin E from *Bacillus subtilis*),[12] 2Z30 (subtilisin from *Thermococcus kodakarensis*),[38] and 1T1E (pro-kumamolisin activation domain from *Bacillus* sp. MN-32)][39] and two structures of the native protease inhibitor POIA1 from *P. ostreatus* (PDB entries 1V5I and 1ITP).[19,21] On the basis of the extensive amount of prior work with propeptide from subtilisin BPN′ that sets a benchmark for our own experiments, its crystallographic coordinates when it was complexed with the expansion of the hydrophobic core is clearly distinct from that of the previously reported covalently linked disulfide variant, offering in principle the opportunity for tunability of protein stability through modifications of noncovalent interactions in proteins, including hydrophobic core and/or surface residues.

Separately, we validated our Rosetta propeptide designs by assessing the structural integrity of propeptide variants via molecular dynamics (MD) simulation using a CHARMM22 force field. Rather than performing such simulations on all designs, we selected representative sequences on the basis of a phylogenetic analysis of third-round sequences using ClustalW2.[40] The analysis reveals a grouping of the propeptide sequences into eight clusters (Figure S1 of the Supporting Information). The differences in sequence among the eight clusters are relatively small and limited to various combinations of amino acid changes at 10 positions. In addition to wild-type BPN′ propeptide (WT) and the disulfide-linked variant of Bryan and co-workers[22] (REF), a representative from each cluster was picked [ROS1−8 (Figure S2 of the Supporting Information)] and used for the MD simulations. The predicted difference in protein stability of the propeptide variants translates into distinct, time-dependent trajectories for their rmsd after an arbitrary burn-in period of 200 ps to reach the equilibrated structure (Figure 2 and Figure S3 of the Supporting Information). As shown in Figure 2, the WT sequence does not appear to be stable, atrophying to the disordered structure. In contrast, the REF sequence seems to be very stable, as deviant conformers quickly recover to the equilibrated state. The artificial disulfide bond, covalently stitching critical secondary structures, may confer this increased stability. The MD data for the eight Rosetta designs fall between these two extremes, showing mostly favorable, rebounding trajectories. These results are consistent with the anticipated improvement in the structural stability of variants compared to WT propeptide yet reflect greater conformational variance than those for REF (Figure 2 and Figure S3 of the Supporting Information). The only exception is ROS4, for which simulation suggests a similar progression toward a disorderly state as seen for WT. On the basis of the computational predictions, we chose two Rosetta designs, the top-scoring ROS1 and the "second-tier candidate" ROS3, for in-depth experimental evaluation.

Expression and Purification of Designer Propeptides. The gene sequences corresponding to the predicted top-scoring propeptide designs ROS1 and ROS3 as well as WT propeptide were prepared by whole-gene DNA synthesis. All nucleotide sequences were codon-optimized for protein expression in *E. coli*. Separately, we generated the disulfide-linked propeptide variant that served as a positive control in our study. The four required mutations (A23C, K27E, V37L, and Q40C) were introduced into the WT sequence, yielding the reference propeptide (REF). Soluble expression of all four peptide sequences was readily accomplished in *E. coli* ArcticExpress (DE3) (for ROS1 and ROS3) or *E. coli* BL21(DE3) pLysS (for WT and REF), yielding protein at a concentration of ~5 mg/L of culture for ROS1 and ROS3 and 15−20 mg/L of culture for WT and REF. The difference in soluble protein expression levels for the Rosetta designs compared to the WT and REF sequences is significant and interesting in light of the notably improved thermostability of the former (see below). A possible explanation for the phenomenon could be Rosetta's focus on the final, folded propeptide structure without consideration of the actual folding pathway. Nevertheless, soluble protein could be purified by a combination of ion-exchange and gel filtration chromatography, yielding the individual propeptides at >95% purity based on SDS−PAGE analysis. The gel filtration experiments also confirmed previous reports of a propeptide monomer−dimer equilibrium, indicating a 70:30 ratio in favor of monomeric ROS1, ROS3, and REF.

Intrigued by the idea of stabilizing the propeptide through the expansion of the hydrophobic core region, we were also curious about whether extensive mutagenesis at more than 50% of the variable positions as suggested by Rosetta was indeed necessary for enhanced protein stability. Alternatively, substantive improvements might be possible through fewer, more specific substitutions in the extended loop region. We thus decided to build a WT variant with only the two site-specific amino acid substitutions at positions 14 (T14A) and 20 (K20W). In the absence of obvious steric problems to accommodate these changes, the two substitutions were introduced by site-directed mutagenesis of the WT gene sequence. Expression of the corresponding propeptide in *E. coli* ArcticExpress (DE3) was attempted at various temperatures and under various induction conditions yet failed to produce any detectable amounts of soluble propeptide. Our results demonstrate that the simple double mutant WT propeptide with the core expansion substitutions alone is insufficient to accomplish the anticipated propeptide stabilization and emphasizes the benefits of additional, compensatory substitutions necessary for expression of soluble protein.

Structural Characterization of Propeptides. The secondary structure content of the WT propeptide as well as ROS1, ROS3, and REF was initially investigated by far-UV circular dichroism (CD) spectroscopy (Figure 3). Spectral scans were recorded from 190 to 260 nm at ambient temperature. In line with previous findings, the WT protein spectrum was consistent with random coil and is assumed to exist in a largely disordered state. In contrast, the spectra for ROS1, ROS3, and REF were consistent with mixed α-helix/β-sheet structures as predicted on the basis of the secondary

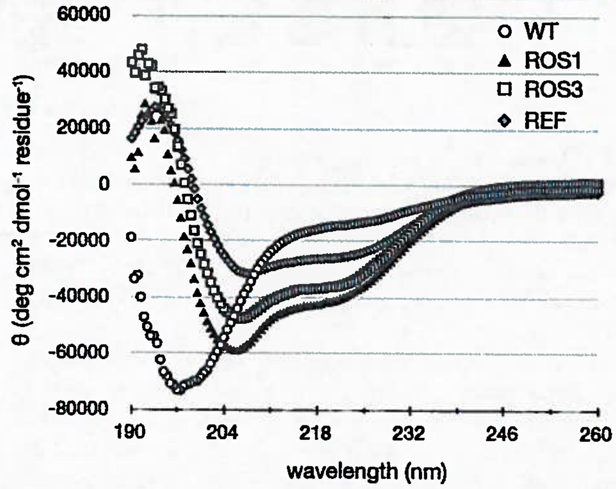

Figure 3. Far-UV circular dichroism spectra (190−260 nm) of wild-type BPN′ (WT), Rosetta design ROS1 and ROS3, and the disulfide-linked variant (REF). While the WT sample resembles a random coil, the spectra of ROS1, ROS3, and REF exhibit clear signatures of mixed α-helix/β-sheet secondary structures. Spectra were recorded on protein samples (25−40 μM) in potassium phosphate buffer (pH 7−8) at ambient temperature.

we evaluated the inhibitory activity of ROS1 and ROS3, as well as WT and REF against three serine proteases, subtilisin Carlsberg, Savinase, and BLAP. Crystal structures among protease complexes have <0.4 Å interface rmsd, and sequence similarity in this region maintains complementary patches of buried hydrophobic and charged interactions, suggesting similar driving forces among subtilisin family members. Subtilisin BPN′ was not included in our study, even though it served as a template for our redesign, as the protease is no longer commercially available. The performance of the propeptide variants was tested in a standard spectrophotometric AAPF activity assay, monitoring the proteolytic activity of individual hydrolases in the presence of different propeptide inhibitor molar ratios.[37]

As shown in Figure 5, all three proteases were inhibited by WT, ROS1, ROS3 and REF albeit to various degrees. The one exception was WT propeptide which did not affect Savinase activity. Against subtilisin Carlsberg, the WT propeptide proved an effective inhibitor with less than 15% proteolytic activity at 20:1 inhibitor:protease ratio. The result was only matched by REF at the highest ratio (50:1) tested in our assay. In contrast, ROS1 and ROS3 show only slight inhibitor activity (60–80% residual proteolytic activity at 50:1). For BLAP, the pattern of inhibitor performance changes significantly. The presence of REF lowers protease activity to <20% at a 10:1 ratio while ROS1 reduces AAPF hydrolysis to ~50% at 10:1 and ~40% at 50:1 inhibitor:protease. ROS3 and WT are less effective, only reaching 30–40% inhibition at a 50:1 ratio. In the case of Savinase, the two Rosetta designs and REF perform similarly, suppressing protease activity to ~70% at the 50:1 ratio. Despite of their moderate inhibitory performance, the results for the three propeptide variants are relevant in light of no detectable inhibitory activity with WT.

Overall, the functional study demonstrates that all four propeptide variants can inhibit selected proteases. Nevertheless, there is no clear correlation between improved thermostability of the propeptides and their effectiveness as inhibitors in our data set. Beyond measuring the inhibitory function of the propeptide variants immediately after they had been mixed with protease, we also explored the time-dependent change in inhibitor activity. Preincubation of individual propeptide variants with proteases for 20 min prior to substrate addition might reveal a stronger correlation between propeptide stability and inhibitor function as the increased structural integrity of the propeptide can slow its degradation by the protease, in turn prolonging inhibitor activity. Subsequent AAPF hydrolysis measurements of the preincubated protein mixtures did detect a reduction in inhibitor activity among all tested propeptide, yet changes were generally within the margin of error (data not shown). Additional experiments exploring longer preincubation times for each protease–inhibitor pair might be necessary for detecting significant differences in inhibitor function in correlation to propeptide stability.

■ CONCLUSIONS

Our study has demonstrated the successful application of computational protein design in combination with MD simulations in generating thermostable variants of the subtilisin BPN′ propeptide domain. The experimental evaluation of the structural properties of ROS1 and ROS3 is consistent with relative rankings based on the arbitrary energy scores in RosettaDesign. Although the data set will benefit from the experimental characterization of additional propeptide designs, our results are consistent with the idea that in silico predictions correlate with propeptide stability. Despite substantial improvements in the structural integrity as reflected by the increased thermostability, the protease inhibition studies nevertheless highlight the current discrepancies between structure and function. More specifically, the original hypothesis in the literature that stabilization of the propeptide will translate into more potent protease inhibitors is clearly not supported by our results. Even for WT and REF, which share high degrees of sequence and structural identity, the inhibitory activity for different proteases varies significantly with no recognizable correlation to the elevated stability of REF. Comparison of the crystal structures for a disulfide-linked propeptide domain closely related to REF (PDB entry 3CNQ)[41] and the WT structure (PDB entry 1SPB)[9] shows an rmsd of 0.94 Å over the entire length of the 71-residue propeptide, yet despite these striking structural similarities, the inhibitory effects of these two propeptides on the proteases in our experiments are notably different. We attribute these uncertainties to discrepancies related to the origin of the propeptide model (subtilisin BPN′) and the tested proteases, as well as small differences in structure and dynamics not accurately captured in the crystallographic information and the computational model. Improved future designs might be possible with the help of advanced Rosetta models considering the flexible backbone and incorporation of interactions at the protease–propeptide interface. Separately, high-resolution nuclear magnetic resonance (NMR) studies will be insightful for validating the accuracy of the Rosetta designs and investigating possible conformational differences between the native propeptide domain and the redesigned structures. Preliminary NMR experiments with the two designer propeptides do indicate a defined secondary structure similar to that of REF (data not shown). Finally, we postulate that the C-terminal portion of the propeptide that was left unchanged for all variants in our study might play an important role in the context of the inhibitory function of these proteins. The region's compatibility with and affinity for the substrate recognition cleft flanking the active site of individual proteases as well as conformational differences between these propeptides and native protease inhibitors such as POIA1 will be the subject of future studies.

■ ASSOCIATED CONTENT

Ⓢ Supporting Information

Details on the computation design and analysis of propeptide variants. This material is available free of charge via the Internet at http://pubs.acs.org.

■ AUTHOR INFORMATION

Corresponding Author

*E-mail: sal2@emory.edu. Telephone: (404) 712-2170.

Funding

This work was in part supported by funds from the National Science Foundation Center for Pharmaceutical Manufacturing and Formulation (I/UCRC 0832469) and through a collaboration with Henkel AG & Co. KGaA (Duesseldorf, Germany).

Notes

The authors declare no competing financial interest.

(37) DelMar, E. G., Largman, C., Brodrick, J. W., and Geokas, M. C. (1979) A sensitive new substrate for chymotrypsin. *Anal. Biochem.* *99*, 316–320.

(38) Tanaka, S., Matsumura, H., Koga, Y., Takano, K., and Kanaya, S. (2007) Four new crystal structures of Tk-subtilisin in unautoprocessed, autoprocessed and mature forms: Insight into structural changes during maturation. *J. Mol. Biol.* *372*, 1055–1069.

(39) Comellas-Bigler, M., Maskos, K., Huber, R., Oyama, H., Oda, K., and Bode, W. (2004) 1.2 Å crystal structure of the serine carboxyl proteinase pro-kumamolisin; structure of an intact pro-subtilase. *Structure* *12*, 1313–1323.

(40) Larkin, M. A., Blackshields, G., Brown, N. P., Chenna, R., McGettigan, P. A., McWilliam, H., Valentin, F., Wallace, I. M., Wilm, A., Lopez, R., Thompson, J. D., Gibson, T. J., and Higgins, D. G. (2007) Clustal W and Clustal X version 2.0. *Bioinformatics* *23*, 2947–2948.

(41) Ruan, B., London, V., Fisher, K. E., Gallagher, D. T., and Bryan, P. N. (2008) Engineering substrate preference in subtilisin: Structural and kinetic analysis of a specificity mutant. *Biochemistry* *47*, 6628–6636.

DOI: 10.1002/anie.201107813

Development of an Amine Dehydrogenase for Synthesis of Chiral Amines**

*Michael J. Abrahamson, Eduardo Vázquez-Figueroa, Nicholas B. Woodall, Jeffrey C. Moore, and Andreas S. Bommarius**

Biocatalysts are increasingly prevalent in the large-scale synthesis of enantiomerically pure compounds (EPCs), which are mainly used as active pharmaceutical ingredients (APIs). Enantiomerically pure forms can lead to lower dosages, improved efficacy, and even allow for extension of patents.[1] In 2000, 35% of APIs were chiral compounds, and this number was expected to increase to 70% by 2010.[2] However, many sought-after reactions lack a suitable enzymatic production route. A recent assessment by the ACS Green Chemistry Institute, Pharmaceutical Roundtable noted that the asymmetric synthesis of amines from prochiral ketones and free ammonia was one of the top aspirational reactions challenging the pharmaceutical industry.[3]

Our novel enzyme achieves exactly that aim: it creates amines with high selectivity. Previously characterized amine dehydrogenases were incapable of effecting the reductive amination of ketones and lacked stereospecificity.[4]

While chiral amines can be produced both chemically and enzymatically, the large-scale production of chiral amines is still challenging and heavily reliant on traditional methods of chemical synthesis.[1,5,6] Common methods include resolution though fractional crystallization[7] and the hydrogenation of C=N bonds, particularly in enamines.[8] Nonetheless, some chemoenzymatic routes, particularly with transaminases,[9] have shown promise in the dynamic kinetic resolution of racemic amines[10] and the direct asymmetric synthesis of amines with ω-transaminases (ω-TA), as used in the synthesis of sitagliptin.[11,12] This novel process has eliminated the use and removal of a less-selective rhodium catalyst, yet requires the use of a sacrificial amine source. The undesired ketone byproduct must also be removed to shift the reaction equilibrium beyond about 50% conversion.

Asymmetric synthesis by amine dehydrogenases (AmDHs) would be the ideal route to produce chiral amines. When paired with a cofactor recycling system, such as glucose/glucose dehydrogenase (GDH) or formate/formate dehydrogenase (FDH), amine dehydrogenases allow for the direct production of chiral amines, with the consumption of only an inexpensive reducing agent, such as glucose or formate, and free ammonia (Scheme 1).[5b,13]

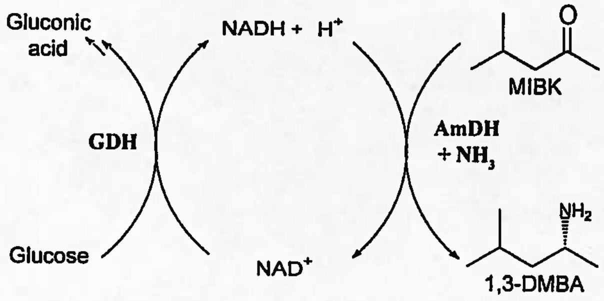

Scheme 1. Asymmetric synthesis reaction scheme with an amine dehydrogenase paired with a glucose dehydrogenase cofactor recycling system.

By using an existing amino acid dehydrogenase scaffold, we have successfully altered the substrate specificity through several rounds of protein engineering to create an amine dehydrogenase. Instead of the wild-type α-keto acid, the amine dehydrogenase now accepts the analogous ketone, methyl isobutyl ketone (MIBK), which corresponds to removal of the carboxyl moiety (Scheme 2). The wild-type leucine dehydrogenase exhibited no measurable activity toward the reductive amination of MIBK.

Leucine dehydrogenase from *Bacillus stereothermophilus* served as the initial protein scaffold. The only crystal structure currently available for leucine dehydrogenase (LeuDH) is an apo crystal structure from *Bacillus sphaericus* (PDB:

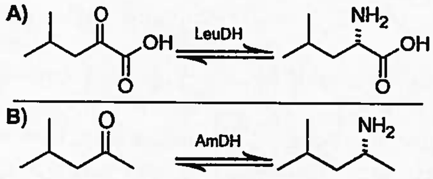

Scheme 2. A) Wild-type leucine dehydrogenase reaction. B) Novel amine dehydrogenase reaction.

---

[*] M. J. Abrahamson, Dr. E. Vázquez-Figueroa, N. B. Woodall, Prof. Dr. A. S. Bommarius
School of Chemical and Biomolecular Engineering, Georgia Institute of Technology, Petit Institute of Bioengineering and Bioscience
311 Ferst Drive N.W., Atlanta, GA 30332 (USA)
E-mail: andreas.bommarius@chbe.gatech.edu
Homepage: http://www.chbe.gatech.edu/bommarius
Dr. J. C. Moore
Department of Process Research, Merck Research Laboratories, Merck and Company, Inc., Rahway, NJ 07065 (USA)

[**] We thank Merck & Co. for initial support. M.J.A. gratefully acknowledges support from a GAANN fellowship by the US Dept. of Education and from NSF I/UCRC grant 0969003 to the Center for Pharmaceutical Development. E.V.-F. gratefully acknowledges support by a NSF Graduate Fellowship and a Goizueta fellowship. Support for the Genetix Colony picker by the NSF-MRI program 0320786 is gratefully acknowledged.

Supporting information for this article is available on the WWW under http://dx.doi.org/10.1002/anie.201107813.

© 2012 Wiley-VCH Verlag GmbH & Co. KGaA, Weinheim

absorbance at 340 nm was correlated to the reduction of the NAD^+ cofactor, and can be related stoichiometrically to substrate conversion. The absorbance at 600 nm accounted for differences in the biomass loading and was used, accordingly, to normalize the absorption at 340 nm. Successful variants were identified on the basis of their normalized 340 nm absorbance, relative to the control plate that lacks any substrate.[19] This ratiometric procedure eliminated false positives arising from the aggregation of cell debris and decreased experimental error.

The resulting hits were purified and analyzed spectrophotometrically for amination and deamination activity. The best variant was then used as the basis for subsequent rounds of mutation.

Early rounds of mutation (libraries 1–9) identified either the wild-type sequence or single variants which improved simultaneously the activity in both the amination and deamination directions, thus allowing for the straightforward selection of the top variant. Library 10 identified distinct mutations for the most-active amination and deamination variants. The most active amination and deamination mutations were with position Asn261 exchanged by Cys and Val. Library 11 further improved the amination activity by identifying synergistic mutations at positions 68 and 261, with these positions mutated from those in libraries 1 and 10. The final amine dehydrogenase contained four mutations, which are summarized in Table 2.

The most-active variants showed amination and deamination activity toward a number of ketones and amines, respectively (Table 3). The final variant (K68S/E114V/N261L/V291C) showed enhanced amination activity over the previous library 10 mutant toward all the ketones investigated, except methyl acetoacetate.

Table 3: Substrate profiles of top amination and deamination variants.

Substrate[a]	K68M/E114V/N261V/ V291C[b]		K68S/E114V/N261L/ V291C[b]	
(*R*)-MBA	476.5	±1.4	586.3	±4.1
(*S*)-MBA	5.0	±0.0	1.6	±0.0
(*R*/*S*)-MBA[c]	484.0	±3.5	784.6	±13.4
cyclohexylamine	–		56.0	±0.0
cyclohexanone	18.8	±0.0	123.4	±3.5
ethyl pyruvate	19.8	±7.0	13.2	±5.8
methyl acetoacetate	4.5	±0.7	4.5	±0.6
ethyl-3-oxohexanoate	6.4	±4.9	14.0	±1.2
acetophenone	3.5	±0.7	58.8	±1.7

[a] Activity measured with 20 mM substrate. [b] Specific activity in $mU\,mg^{-1}$ protein, with the error representing one standard deviation. [c] Activity measured with 40 mM racemic MBA, 20 mM of each enantiomer.

The enantioselectivity was initially estimated by measuring the deamination activity toward individual enantiomers of methylbenzylamine (MBA). MBA was used in place of 1,3-DMBA for selectivity experiments since it had a reasonable level of activity and individual enantiomers of MBA were commercially available. A preference towards (*R*)-MBA over the corresponding *S* enantiomer was evident from the deamination activities of $0.586\,U\,mg^{-1}$ and $0.002\,U\,mg^{-1}$, respectively. These preliminary results were corroborated through direct measurement of the enantioselectivity of the MIBK amination in producing chiral 1,3-DMBA. Enzymatic conversion was allowed to continue for a total of 48 h with a GDH-cofactor recycling system, and gave a ketone substrate conversion of (92.5±2.6)%. The resulting amine product was extracted from the aqueous reaction phase using toluene, subsequently derivatized using trifluoroacetic anhydride (TFAA), and analyzed by gas chromatography. The derivatization of 1,3-DMBA allowed adequate baseline separation of the peaks, with elution times of 47.5 and 48.9 min for the *S* and *R* enantiomers, respectively. The enantiomer peaks were identified through polarimetry since pure enantiomer standards were not available.[19] The resulting data gave an *ee* value of 99.8% toward (*R*)-1,3-DMBA, which corresponds to the wild-type *S* selectivity (change of Cahn–Ingold–Prelog preference upon replacement of the carboxy group by a methyl group). The amine product was extracted from an 175 mL-scale reaction using methyl *tert*-butyl ether and concentrated through rotovap distillation. 29.5 mg of (*R*)-1,3-DMBA at 84.7% conversion resulted, as confirmed by the ^1H NMR spectrum and chiral gas chromatography.[19]

In conclusion, we have successfully developed an amine dehydrogenase, by starting with an existing amino acid dehydrogenase as a template and subsequent active-site-targeted protein engineering. Eleven rounds of protein engineering completely inverted the enzyme's specificity and created amination activity of $0.69\,U\,mg^{-1}$ with a corresponding k_{cat} value of $0.46\,s^{-1}$. In doing so, the native activity toward L-Leu was reduced to immeasurably low levels. The enantioselectivity of the wild-type enzyme was maintained,

Table 2: Accumulated mutations and resulting improvements to the specific activity and K_M value of leucine dehydrogenase.[a]

Library	Mutations	Reductive amination specific activity[b]		K_M[c]		Oxidative deamination specific activity[b]		K_M[c]	
wild-type	–	n.m.[d]		n.m.		n.m.		n.m.	
1	K68M	0.0002		n.m.		0.0034		n.m.	
3	K68M, E114V	0.015		n.m.		0.65		48	
6	K68M, E114V, V291C	0.016	±0.004	70.2	±35	1.02	±0.41	77.1	±66
10[e]	**K68M, E114V, N261V, V291C**	0.089	±0.007	10.3	±3.6	**2.81**	±0.44	30.9	±13
	K68M, E114V, N261C, V291C	0.236	±0.04	21.6	±12	1.76	±0.20	14.8	±6.0
11	**K68S, E114V, N261I, V291C**	**0.690**	±0.07	**15.1**	±5.1	2.64	±0.28	57.5	±12.5

[a] Error values represent 95% confidence intervals of nonlinear fit parameters. [b] Maximum specific activity (units/mg protein). [c] MIBK or 1,3-DMBA substrate (mM). [d] n.m. = not measurable ($<0.1\,mU\,mg^{-1}$). [e] Separate variants gave maximum amination and deamination activity.

© 2012 Wiley-VCH Verlag GmbH & Co. KGaA, Weinheim

DOI: 10.1002/adsc.201201030

The Evolution of an Amine Dehydrogenase Biocatalyst for the Asymmetric Production of Chiral Amines

Michael J. Abrahamson,[a] John W. Wong,[b] and Andreas S. Bommarius[a,c,*]

[a] School of Chemical and Biomolecular Engineering, Georgia Institute of Technology, Parker H. Petit Institute of Bioengineering and Bioscience, Atlanta, GA 30332-0400, USA
Fax: (+1)-404-894-2295; phone: (+1)-404-385-1334; e-mail: andreas.bommarius@chbe.gatech.edu
[b] Chemical Research & Development, Pfizer Worldwide Research & Development, Groton, CT 06340, USA
[c] School of Chemistry and Biochemistry, Georgia Institute of Technology, 901 Atlantic Drive, Atlanta, GA 30332-0400, USA

Received: November 20, 2012; Published online: March 20, 2013

Supporting information for this article is available on the WWW under http://dx.doi.org/10.1002/adsc.201201030.

Abstract: The reductive amination of ketones to produce chiral amines is an important transformation in the production of pharmaceutical intermediates. Therefore, industrially applicable enzymatic methods that enable the selective synthesis of chiral amines could be very useful. Using a phenylalanine dehydrogenase scaffold devoid of amine dehydrogenase activity, a robust amine dehydrogenase has been evolved with a single two-site library allowing for the direct production of (*R*)-1-(4-fluorophenyl)-propyl-2-amine from *para*-fluorophenylacetone with a k_{cat} value of 6.85 s^{-1} and a K_M value of 7.75 mM for the ketone substrate. This is the first example of a highly active amine dehydrogenase capable of accepting aliphatic and benzylic ketone substrates. The stereoselectivity of the evolved amine dehydrogenase was very high (>99.8% *ee*) showing that high selectivity of the wild-type phenylalanine dehydrogenase was conserved in the evolution process. When paired with glucose/glucose dehydrogenase, NADH cofactor can be effficiently regenerated and the reaction driven to over 93% conversion. The broad specificity, high selectivity, and near complete conversion render this amine dehydrogenase an attractive target for further evolution toward pharmaceutical compounds and subsequent application.

Keywords: amine dehydrogenase; asymmetric catalysis; biocatalysis; chiral amines; directed evolution

Introduction

One of the shortcomings of biocatalysis is the limited number of reactions which have identified enzymatic routes. As the field of protein engineering grows, the characterization of novel biocatalysts expands the repertoire of accessible reactions.[1–4] A prominent example of this novel application is the recent evolution of an ω-transaminase to produce sitagliptin.[5,6] Biocatalysis is emerging as an essential tool in the asymmetric synthesis of chiral intermediates, which play a particularly important role as building blocks for the pharmaceutical industry. Therapeutic compounds often act as structurally optimized inhibitors of biological processes, and since the human body functions using chiral chemistry, these compounds almost always contain chiral centers. Enantiomerically pure forms of active pharmaceutical ingredients (APIs) can lead to lower dosages, increased efficacy, and elimination of detrimental side-effects.[7] In 2006, 80% of small-molecule drugs approved by the FDA were chiral and 75% were single enantiomers.[8] The production of chiral amines is of particular importance due to their highly active and diverse influence on biological functions.[3–5,7,9] Amine-based pharmaceuticals are used in a wide range of functions including; stimulants[10], decongestants[11], vasoconstrictors[12], and antidepressants.[13]

The production of chiral amines remains difficult through traditional chemical catalysis,[3,14] and the direct amination of ketones with free ammonia to produce chiral amines has been identified as one of the most aspirational reactions challenging the pharmaceutical industry by the American Chemical Society's Green Chemistry Institute, Pharmaceutical Roundtable.[15] Recently, we have demonstrated this reaction by an amine dehydrogenase (AmDH) that was obtained through the modification of a leucine dehydrogenase (LeuDH) scaffold to accept ketone substrates[1]. This biocatalytic route of production

WILEY ONLINE LIBRARY

© 2013 Wiley-VCH Verlag GmbH & Co. KGaA, Weinheim

Table 2. Characterization of his-tag-purified PheDH library 1 hits. Kinetic parameters k_{cat} and K_M determined by non-linear fit for the amination of PFPA.

K77 Residue	N276 Residue	Non-Linear Michaelis–Menten			
		$k_{cat,app}$ [s^{-1}][a]		K_M [mM]	
Ser	**Leu**	**2.80**	**±0.54**	**4.4**	**±1.6**
Trp	**Glu**	**2.63**	**±0.16**	**5.3**	**±0.6**
Met	Met	1.82	±0.19	7.9	±1.3
Ser	Ser	1.31	±0.36	14.5	±5.2
Cys	Leu	1.29	±0.25	3.5	±1.4
Met	Leu	1.28	±0.10	4.2	±0.6
Ser	Val	1.06	±0.19	4.4	±1.5
Met	Cys	0.90	±0.08	1.5	±0.4
Met	Leu	0.86	±0.18	4.6	±1.8
Ser	Phe	0.79	±0.18	22.2	±0.4
Met	Ser	0.66	±0.07	4.9	±1.0
Val	Leu	0.56	±0.06	3.3	±0.8
Cys	Ile	0.55	±0.06	7.7	±1.4
Gly	Ile	0.34	±0.07	5.9	±2.0
Ser	Gly	0.28	±0.07	6.8	±2.7
Ser	Met	0.10	±0.04	28.6	±13.8
Gly	Cys	0.029	±0.00	–	
Ser	Glu	0.024	±0.01	9.0	±7.6
Trp	Ile	0.019	±0.01	–	
Trp	Gly	0.017	±0.02	–	
Gly	Val	0.017	±0.01	–	

[a] Apparent k_{cat} values in 225 mM NH_4Cl/NH_4OH pH 9.6, 200 μM NADH.

other variants at these two positions could yield further synergistic improvements. Since previous libraries had identified LeuDH K67M as a beneficial mutation, it was essential that the degenerate codon at that position include methionine to ensure the identification of the best variant. With a two-site library, codon selection must also be efficient by limiting codon redundancy to maintain a manageable screening effort. A two-site NNK library at these residues would encode for all 20 amino acids at each position. This large number of amino acid substitutions and codon redundancy results in a significant screening effort of 3066 colonies to achieve statistical coverage. The more restricted and efficient codon DDK greatly reduces the screening effort to 969 colonies by limiting the redundancy while still including a structurally-diverse selection of 15 amino acids.

The high-throughput screening of this diverse two-site PheDH K77DDK N276DDK library identified 36 highly-active colonies, containing 21 unique variants for subsequent characterization. These variants were purified and individually characterized for kinetic parameters in the amination of PFPA to more accurately determine which combination of mutations performed best (Table 2). All unique variants within the 21 pairs of mutations were active amine dehydrogenases, eight of which provided apparent k_{cat} values greater than 1 s^{-1} in the amination of PFPA. The K77S/N276L variant was selected as the top candidate for further characterization, since it had the highest apparent k_{cat} value and a lower PFPA K_M value than the next best K77W/N276E variant.

Characterization of PheDH-AmDH

The K77S/N276L variant was characterized in detail for a number of properties including; pertinent kinetic parameters, substrate specificity, thermostability, overall conversion, and enantioselectivity.

Kinetic parameters, $k_{cat,app}$ and K_M, were determined for the enzyme and each of the amination and deamination substrates. The original assay conditions of 225 mM NH_4Cl/NH_4OH buffer did not saturate the enzyme with respect to NH_3. The k_{cat} value for this AmDH enzyme with all three substrates saturated in 2M NH_4Cl/NH_4OH buffer at pH 9.6 was 6.85±0.59 s^{-1} at 25 °C. This k_{cat} value was nearly 15-fold greater than the maximum observed k_{cat} of 0.46 s^{-1} for the previously developed LeuDH-AmDH.[1] The increase in buffer concentration did have an effect upon the K_M value of PFPA, which increased to 7.75±1.67 mM under saturated reaction conditions of 2M NH_4Cl/NH_4OH buffer (pH 9.6) with 200 μM NADH. The K_M value for NADH was 23.9±0.6 μM and was similar to the K_M value of native PheDH for NADH.

The significant increase in the K_M for NH_3 ($K_{M,\ NH_3}$=557±107 mM) seen in the amination of PFPA, as compared to the amination of phenyl pyruvate by the wild-type PheDH ($K_{M,\ NH_3}$=37.6±5.2 mM) can be at least partially attributed to decreased activation of the carbonyl moiety of PFPA, with its neighboring methyl group, compared to the carbonyl moiety in phenyl pyruvate, which is activated by the adjacent carboxyl group. The smaller δ+-charge of the α-carbon decreases its electrophilicity, requiring a higher concentration of the ammonia nucleophile.

The deamination of (*R/S*)-FPPAm exhibited slightly lower activity with a k_{cat} value of 1.92±0.10 s^{-1}. The K_M values of the amine substrate and NAD^+ were similar to those for the amination reaction being 3.42±0.42 mM and 61.6±12.1 μM, respectively.

The substrate scope of the K77S/N276L PheDH-AmDH double variant was evaluated by determining the amination and deamination activities toward a number of different ketones and amines. The diversity of these ketones varied in structure from small aliphatic ketones such as 3-methyl-2-butanone, to larger aromatic ketones with additional functionality, such as phenoxy-2-propanone.

The enzyme showed elevated activity toward methyl ketones versus ethyl ketones or cyclic ketones (Table 3). The top five most active ketones; PFPA,

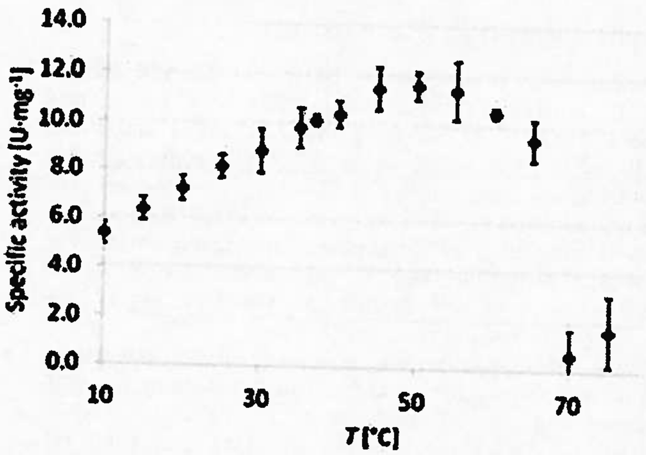

Figure 3. Profile of activity versus temperature for PheDH K77S/N276L double variant (AmDH). Amination activity measured in 2M NH_4Cl/NH_4OH buffer pH 9.6, 200 μM NADH, and 20 mM PFPA for 2 min.

enthalpy of melting. The K77S/N276L variant resulted in a melting point of 59.9 °C, 4.4 °C less than the wild-type. The specific cause for this change is unknown, but could be due to either disruption of the packing of the wild-type enzyme's hydrophobic core or a net decrease in hydrophobicity by the amino acid substitutions resulting in a lower folding entropy.[19]

The thermostability of the double variant K77S/N276L was additionally investigated by an activity *versus* temperature profile (Figure 3). This profile shows the enzyme's near-linear increase in the lower temperature range (10–45 °C), corresponding to a low apparent Arrhenius activation energy of $241\ \mathrm{J\,mol^{-1}}$.[20] At 50 °C, close to the temperature of maximum activity, the maximum specific activity was $11.6\ \mathrm{U\,mg^{-1}}$. Above 50 °C, the enzyme began to rapidly lose activity as a result of denaturation. This data correlated well with the CD data where a dramatic loss of secondary structure was also observed above 50 °C.

Conclusions

Previous knowledge gained in the evolution of an amine dehydrogenase from LeuDH,[1] particularly the influence of binding pocket residues Lys77 and Asn276, allowed for the rapid evolution of an AmDH from PheDH from *Bacillus badius*. With a reasonably active starting variant K77M/N276V, a stringent high-throughput screening of a single two-site library across the sites 77 and 276 identified a variant, K77S/N276L, with high reductive amination activity with a k_{cat} value of $6.85\ \mathrm{s^{-1}}$ at 25 °C. The evolved AmDH demonstrated extremely high enantioselectivity [> 99.8% *ee* in the conversion of PFPA to (*R*)-FPPAm], which is a critical feature for the synthesis of chiral amines. The reaction can be simply and inexpensively driven to high conversions in excess of 90% when paired with a cofactor recycle system. With a temperature of maximum activity of 50 °C, at which the observed specific activity rises to $11.6\ \mathrm{U\,mg^{-1}}$, the K77S/N276K AmDH variant is sufficiently stable for further evolution,[21] despite a 4.4 °C decrease in thermostability in comparison with wild-type PheDH. The novel AmDH exhibits amination activity towards a range of ketone substrates, with preference for methyl ketones, and beta-positioned ketones in the case of aromatic substrates. In summary, K77S/N276K AmDH is a good starting point for further evolution to increase activity toward specific API targets or fine chemicals.

Experimental Section

General

Substrates were obtained from suppliers and used without further purification. NADH was obtained from Amresco (Solon, OH). NAD^+, NH_4OH, PFPA, (*R*)-MBA, (*R/S*)-MBA, MIBK, 1,3-DMBA, phenoxy-2-propanone, 2-hexanone, ethyl pyruvate, 2-methylcyclohexanone, 3-methylcyclohexanone, and 3-methyl-2-butanone were obtained from Sigma (St. Louis, MO). (*S*)-MBA, acetophenone, cyclopentanone, and benzaldehyde were obtained from Fluka (St. Louis, MO). NH_4Cl was obtained from BDH (London, UK). (*R/S*)-FPPAm and 3-pentanone were obtained from Alfa Aesar (Ward Hill, MA). 3-Hexanone was obtained from Riedel-de Haen (Seelze, Germany). Cyclohexanone was obtained from Mallinckrodt (Phillipsburg, NJ). ^1H NMR spectra were obtained in $CDCl_3$ at 400 MHz on a Varian Mercury VX400 spectrometer. Gas chromatography was performed on a Shimadzu GC-2010 gas chromatographer equipped with a Restec Rt-BDEXcst column.

Gene Cloning and Expression

Genomic DNA from *Bacillus badius* Bachelor (ATCC# 14574) was purchased from the American Type Culture Collection. The gene was amplified using a standard PCR protocol[22] with the forward primer, 5′-GGAATTC**CATAT**GAGCTTAGTAGAAAAAACATCCATCA-3′ and reverse primer, 5′-CCGCT**CGAGTA**TTAGTTGCGAATATCCCATTTTG-3′. These primers simultaneously inserted the restriction sites *Nde*I and *Xho*I prior to and following the gene, respectively. The locations of the restriction sites are indicated by bold type with each primer. This made for simple digestion and ligation into either pET17b or pET28a plasmids.

Wild-type PheDH from *Bacillus badius* and variants were expressed in a pET28a, BL21 (DE3) system at 37 °C in MagicMedia™ media for 24 h, and subsequently his-tag purified using standard Ni-NTA affinity chromatography.

Activity Measurements

Activity of purified proteins was measured using a spectrophotometric assay at 340 nm, corresponding to the cofactor

© 2013 Wiley-VCH Verlag GmbH & Co. KGaA, Weinheim

laher, D. Hilvert, M. H. Gelb, B. L. Stoddard, K. N. Houk, F. E. Michael, D. Baker, *Science* **2010**, *329*, 309; l) M. Hall, A. S. Bommarius, *Chem. Rev.* **2011**, *111*, 4088.

[3] M. Breuer, K. Ditrich, T. Habicher, B. Hauer, M. Kebeler, R. Stürmer, T. Zelinski, *Angew. Chem.* **2004**, *116*, 806; *Angew. Chem. Int. Ed.* **2004**, *43*, 788.

[4] M. Höhne, U. T. Bornscheuer, *ChemCatChem* **2009**, *1*, 42.

[5] F. G. Mutti, J. Sattler, K. Tauber, W. Kroutil, *ChemCatChem* **2011**, *3*, 109.

[6] C. K. Savile, J. M. Janey, E. C. Mundorff, J. C. Moore, S. Tam, W. R. Jarvis, J. C. Colbeck, A. Krebber, F. J. Fleitz, J. Brands, P. N. Devine, G. W. Huisman, G. J. Hughes, *Science* **2010**, *329*, 305.

[7] I. Agranat, S. R. Wainschtein, *Drug Discovery Today* **2010**, *15*, 163.

[8] A. M. Thayer, Chem. Eng. News **2007**, *85*, 11.

[9] a) J. S. Carey, D. Laffan, C. Thomson, M. T. Williams, *Org. Biomol. Chem.* **2006**, *4*, 2337; D. J. Pollard, J. M. Woodley, *Trends Biotechnol.* **2007**, *25*, 66; b) J. Tao, J.-H. Xu, *Curr. Opin. Chem. Biol.* **2009**, *13*, 43; N. J. Turner, R. Carr, *Biocatal. Pharm. Biotechnol. Ind.* **2007**, 743.

[10] P. M. Groves, G. V. Rebec, *Annu. Rev. Psychol.* **1976**, 27, 91.

[11] R. P. Roth, E. I. Cantekin, C. D. Bluestone, R. M. Welch, Y. W. Cho, *Ann. Otol., Rhinol. Laryngol.* **1977**, *86*, 235.

[12] R. Y. Moore, F. E. Bloom, *Annu. Rev. Neurosci.* **1979**, *2*, 113.

[13] J. W. Maas, *Trends Neurosci.* **1979**, *2*, 306.

[14] A. Johansson, *Contemp. Org. Synth.* **1995**, *2*, 393; T. C. Nugent, M. El-Shazly, *Adv. Synth. Catal.* **2010**, *352*, 753.

[15] D. J. C. Constable, P. J. Dunn, J. D. Hayler, G. R. Humphrey, J. L. Leazer, R. J. Linderman, K. Lorenz, J. Manley, B. A. Pearlman, A. Wells, A. Zaks, T. Y. Zhang, *Green Chem.* **2007**, *9*, 411.

[16] Y. Asano, A. Nakazawa, K. Endo, Y. Hibino, M. Ohmori, N. Numao, K. Kondo, *Euro. J. Biochem.* **1987**, *168*, 153.

[17] R. Maiti, G. H. Van Domselaar, H. Zhang, D. S. Wishart, *Nucleic Acids Res.* **2004**, *32*, 590.

[18] United States Department of Justice, Drug Enforcement Administration, **2012**.

[19] a) R. Jaenicke, *Eur. J. Biochem.* **1991**, *202*, 715; b) B. W. Matthews, H. Nicholson, W. J. Becktel, *Proc. Natl. Acad. Sci. USA* **1987**, *84*, 6663.

[20] A. Cornish-Bowden, *Fundamentals of Enzyme Kinetics*, Portland Press, **2004**.

[21] J. D. Bloom, F. H. Arnold, *Proc. Natl. Acad. Sci. USA* **2009**, *106*, 9995.

[22] J. Sambrook, D. W. Russell, *Molecular Cloning: A Laboratory Manual*, Cold Spring Harbor Laboratory Press, **2001**.

[23] R. M. C. Dawson, D. C. Elliott, W. H. Elliott, *Data for Biochemical Research*, Clarendon Press, **1989**.

[24] *Stratagene Quikchange® Site-Directed Mutagenesis Kit*, Vol. Revision A, **1998**.

[25] a) L. Munoz, A. M. Rodriguez, G. Rosell, M. P. Bosch, A. Guerrero, *Org. Biomol. Chem.* **2011**, *9*, 8171; b) A. Plenevaux, S. L. Dewey, J. S. Fowler, M. Guillaume, A. P. Wolf, *J. Med. Chem.* **1990**, *33*, 2015.

© 2013 Wiley-VCH Verlag GmbH & Co. KGaA, Weinheim